Investigation of nanomechanical resonators in a micro cavity for optomechanics experiments

Dissertation der Fakultät für Physik der
Ludwig-Maximilians-Universität München

vorgelegt von
Sebastian Stapfner
geboren in Rosenheim

München 2016

Erstgutachter: Prof. Eva M. Weig
Zweitgutachter: Prof. Joachim Rädler
Tag der mündlichen Prüfung: 5. Februar 2016

Für Steffi und unsere Kinder.

Zusammenfassung

Die dynamische Kopplung zwischen Licht und mechanischen Systemen wird seit einigen Jahren intensiv unter dem Überbegriff Optomechanik untersucht. Um diese Wechselwirkung möglichst effektiv zu gestalten, sind drei Parameter entscheidend. Die Abklingzeit der optisch induzierten Kraft sollte größer oder zumindest vergleichbar mit der Periodendauer der mechanischen Oszillation sein und die effektive mechanische Masse sowie die Dämpfung der mechanischen Schwingung sollten möglichst klein sein. Für die Messung dieser lichtinduzierten Effekte bieten sich also sehr kleine mechanische Systeme, sogenannte mikro- und nanoelektromechanische Systeme (M/NEMS), mit hohen mechanischen Güten an.

In dieser Arbeit wurde ein experimenteller Aufbau realisiert, der es ermöglicht MEMS und NEMS im intensiven Lichtfeld einer Miniatur-Fabry-Pérot-Kavität zu untersuchen. Verspiegelte Endflächen von optischen Glasfasern im Abstand von einigen zehn Mikrometern formen diese Kavität mit sehr hoher Finesse. Die Kavität wird im Vakuum betrieben, um die Güte der M/NEMS hoch zu halten. Ein Laser zur Anregung der Kavität kann über die optische Resonanz verstimmt werden. Die Schwingung der M/NEMS moduliert das reflektierte bzw. transmittierte optische Signal im Megahertzbereich und wird mittels Fotodetektoren elektrisch spektral analysiert.
In diesem Aufbau kamen mechanische Resonatoren zum Einsatz, die nach zwei komplementären Gesichtspunkten hergestellt wurden. Einerseits wurden Resonatoren aus Kohlenstoffnanoröhren (carbon nanotubes, CNTs) mit sehr geringer Masse und andererseits aus Siliziumnitrid (SiN) mit sehr hoher mechanischer Güte gefertigt.

NEMS aus CNTs hatten Abmessungen weit unter der Wellenlänge des verwendeten Lichts. In der Miniaturkavität wurde durch Ausnutzung dispersiver Wechselwirkung die thermisch getriebene brownsche Bewegung bei Raumtemperatur mit der Eigenfrequenz des CNTs gemessen.

M/NEMS aus SiN waren herstellungsbedingt größer als CNT-NEMS, wurden jedoch mit sehr hohen mechanischen Güten gefertigt. Abhängig von Form der SiN-Strukturen und ihrer Position in der Kavität wurden sehr hohe optomechanische Kopplungen demonstriert. Bei moderaten Kopplungen ließen sich optisch induzierte Änderungen der mechanischen Resonanzfrequenzen nachweisen. Diese stimmen qualitativ mit einem theoretischen Modell überein, in dem dispersive und dissipative optomechanische Kopplungen berücksichtigt sind. Als weitere Ursache für die Frequenzverschiebungen wurden photothermische Effekte identifiziert.

Contents

Chapter 1

Introduction

Already in the 1960's the dynamics of mechanical systems coupled to radiative fields has been studied [Bra67]. In a pioneer experiment mechanical bistability of a macroscopic mirror subjected to an intense laser field has been demonstrated in the 1980's [Dor83]. Another two decades later radiation pressure was employed to actively damp out the mechanical vibration of a mirror by means of electronic feedback [Coh99]. The field of optomechanics attained increased attention in 2004 when the potential for optomechanical ground state cooling without use of electronic feedback was suggested [Met04]. This implies that an oscillatory mode of a macroscopic object can be prepared in a quantum state which promises fundamental tests of quantum mechanics on a macroscopic scale [Vit07, Har08]. Fueled by this prospect a growing number of teams started their research on this topic and a diversity of optomechanical systems arose. The popular scheme of the 'deformable Fabry-Pérot cavity' where a macroscopic movable cavity mirror forms the mechanical element was copied in several experiments [Met04, Kle06, Gig06, Cor07]. The 'membrane-in-the-middle' scheme operates with a fixed cavity that couples to the motion of a thin dielectric membrane inside it [Tho08]. Integrated photonic elements on the micrometer scale like silica toroids [Sch06] and semi-conducting disks [Din10] support whispering-gallery optical and acoustic modes that exhibit optomechanical behavior analog to the 'deformable Fabry-Pérot cavity'. Photonic-phononic crystals with carefully engineered photonic and phononic bands form a further class of very successful optomechanical nanostructures [Cha11]. Levitated particles in optical traps are not connected to any substrate and the mechanical and vibrational properties are controlled by the light field [Gie12]. Electronic resonant circuits where the capacitive element depends on the position of a mechanical element represent optomechanical systems in the microwave regime [Reg08, Roc10]. All these realizations have in common that the mechanical vibration alters the optical properties of the cavity, which gives rise to a parametric coupling.
Ground state cooling has already been demonstrated by three research groups. By direct cooling a gigahertz resonator mode in a dilution cryostat the energy of the thermal bath was set below the oscillatory energy of the mechanical mode at gigahertz frequency $k_{\mathrm{B}}\,T < \hbar\,\Omega$ [O'C10]. The mechanical ground state was achieved by optomechanical cool-

ing with a microwave electronic [Teu11a] and a nanophotonic optical setup [Cha11]. Technological applications emerging from optomechanical research are in the fields of ultrasensitive transducers [Kra12] and optical information technology [Fio11, And14].

In the theory for the observed optomechanical effects reference [Met04] imposes three requirements on the system of study with low finesse cavities. Firstly, the resonator must be of low mass; secondly, the rate of mechanical energy dissipation has to be small; and finally, the loss rate in the cavity containing the optical field be comparable to the natural frequency of a mechanical mode. The quantitative assertion of these requirements has inspired the optomechanics community to meet these requirements using a system consisting of a nanomechanical resonator in a fixed miniature optical cavity [Fav08].
In the present work, we investigate the direct coupling of light and mechanics by positioning a nanomechanical resonator in an optical cavity. The optical apparatus comprises a miniature high finesse cavity between two nearly abutting optical fibers. This technique originally developed for experiments in atomic optics [Ste06] has found application many fields, including the investigation of optical nanostructures [Bar11] or nitrogen vacancy centers [Alb13]. In literature, the two approaches pursued to realize mechanical resonators that meet the named requirements are *bottom-up* processes and *top-down* fabrication. An example of the former is carbon nanotubes that are fabricated ready to fit into the cavity, realizing the lowest-possible-mass object resonating in the cavity. Exemplifying the latter, doubly clamped resonators are engineered top-down by semiconductor techniques from silicon nitride. These structures, sporting sub-micron cross-sectional dimensions, display outstanding mechanical dissipation characteristics [Unt10].

Consequently this thesis is built-up as follows.
In chapter 2 theoretical background information and salient tools to model the optical and mechanical components of the optomechanical system are presented. Mechanisms of the optomechanical coupling are explained and finally three optomechanical models are outlined. These models, all known from literature, are relevant in this work in order to describe a nanomechanical element inside a fixed microcavity.
The experimental setup is presented in chapter 3. Starting with a detailed explanation of the assembly procedure for miniature cavities and their characterization, the measurement setup is described. This includes lasers and light sources to illuminate the cavity, optical readout, feed-back loops for laser and cavity stabilization, sample positioning and vacuum handling.
Chapter 4 comprises results on the work with CNTs published in *Applied Physics Letters* in 2013 [Sta13]. The preparation of carbon nanotube devices for the use inside the cavity and their characteristics are detailed. Measurements of these nanoscopic samples in the optical cavity exhibit a sensitivity sufficient to clearly resolve the Brownian motion of the nanotube.
The top-down approach with silicon nitride material is presented in chapter 5. The processing of doubly-clamped freely suspended strings to be introduced into the cavity poses its individual challenges, however this method keeps large freedom of design and fabricated structures exhibit remarkable mechanical characteristics. With carefully designed

shape and precise positioning of the strings in the cavity, enormous optomechanical coupling rates are observed. At moderate couplings optically influenced mechanical frequencies fit qualitatively to a model including dispersive and dissipative coupling when extended by a term accounting for a photothermally induced frequency shift.

Chapter 2

Theoretical considerations

A mechanical element inside an optical cavity forms an optomechanical system. Both systems influence each other via the mechanical displacement and forces exerted by the intense light field of the cavity. This way a complex back-action mechanism is formed leading to altered optical and mechanical characteristics [Asp14]. An illustration of the optomechanical system studied in this work is presented in figure 2.1. Here a mechanical element smaller than the typical optical wavelength vibrates with amplitude z at position z_0 inside the optical field of a cavity. In order to understand the complex dynamic behavior of the whole system it is useful to know about the optical and mechanical subsystem and their interaction first. The concepts of optomechanical systems are presented for the deformable Fabry-Pérot cavity first and subsequently translated to a model describing the more specific case of a nanomechanical element inside a micro cavity. This chapter introduces formalisms and models available from published articles and textbooks that are useful for the experimental work.

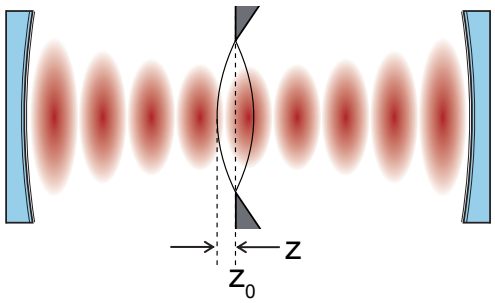

Figure 2.1: Illustration of a sub-wavelength sized mechanical resonator in an optical cavity (adopted from reference [Fav08]).

2.1 Optomechanics principles

Optomechanical systems comprise optical and mechanical subsystems that are coupled through an optically induced dynamical backaction force and geometrical constraints given by the mechanical displacement. It is crucial to know about the characteristics of both subsystems and their interaction mechanisms. In the following, theoretical formalisms to describe the optical and mechanical system individually are presented as well as the coupling between them.

2.1.1 Optical cavity

A Fabry-Pérot cavity formed by a pair of concave mirrors builds the optical element of this work. The geometry and further parameters of the cavity mode are derived from the Gaussian beam formalism and from a transfer matrix formalism for propagation of the electric field through layered media. Standard text books on optics provide the basis for these calculations [Sal91, Sie86, Kle88].

Gaussian beam

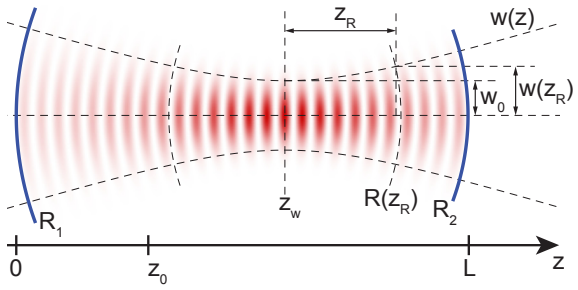

Figure 2.2: Illustration of the absolute electric field (red) distributed inside an optical cavity. Spherical mirrors are sketched blue with radii R_1 and R_2

The optical mode that is supported in an empty cavity with spherical mirrors like the one sketched in figure 2.1 can be derived from the radii of curvature of the mirrors R_1 and R_2 and their distance L. A transfer matrix method is applied that is explained in common optics textbooks like reference [Sal91]. In paraxial approximation, the beam is described by the distance from the optical axis r and its slope or the angle of the beam with the optical axis $r' = \mathrm{d}r/\mathrm{d}z$ in vector form

$$\begin{pmatrix} r \\ r' \end{pmatrix}. \tag{2.1}$$

Matrices transform the vector as the propagation through an optical system transforms the beam. Propagation of the beam through the cavity from z_0 to the right for one round trip transforms the initial beam $(r_\mathrm{i}, r'_\mathrm{i})$ into the final beam $(r_\mathrm{f}, r'_\mathrm{f})$ as

$$\begin{pmatrix} r_\mathrm{f} \\ r'_\mathrm{f} \end{pmatrix} = \begin{pmatrix} 1 & z_0 \\ 0 & 1 \end{pmatrix} \begin{pmatrix} 1 & 0 \\ -\frac{2}{R_1} & 1 \end{pmatrix} \begin{pmatrix} 1 & L \\ 0 & 1 \end{pmatrix} \begin{pmatrix} 1 & 0 \\ -\frac{2}{R_2} & 1 \end{pmatrix} \begin{pmatrix} 1 & L - z_0 \\ 0 & 1 \end{pmatrix} \begin{pmatrix} r_\mathrm{i} \\ r'_\mathrm{i} \end{pmatrix}$$
$$= \begin{pmatrix} A & B \\ C & D \end{pmatrix} \begin{pmatrix} r_\mathrm{i} \\ r'_\mathrm{i} \end{pmatrix} \tag{2.2}$$

where the ABCD matrix summarizes the single transformations of the whole system. According to Gaussian beam formalism the q-parameter

$$\frac{1}{q(z)} = \frac{1}{R(z)} - i \frac{\lambda}{\pi w^2(z)} \tag{2.3}$$

fully characterizes the Gaussian beam with radius of curvature of the wavefront $R(z)$ and beam radius $w(z)$ at position z for wavelength λ (see e.g. reference [Sal91]). The propagation of a Gaussian beam is described by matrices, too. Especially the ABCD matrix applied to the q-parameter with the requirement of a stable cavity mode and stating its reproduction after one round trip yields

$$q(z + \text{"one round trip"}) = \frac{A\,q(z) + B}{C\,q(z) + D} \equiv q(z), \tag{2.4}$$

which gives an equation for the cavity mode

$$\frac{1}{q(z)} = -\frac{A - B}{2\,D} \pm i \frac{1}{B} \sqrt{1 - \frac{(A + D)^2}{4}}. \tag{2.5}$$

Together with equations 2.2 and 2.3

$$R(z) = \frac{z^2(-2\,L + R_1 + R_2) + L\,R_1(R_2 - L) + 2\,L\,z(L - R_2)}{L^2 - L(R_2 + 2\,z) + z(R_1 + R_2)} \tag{2.6}$$

$$w^2(z) = \frac{\lambda\,(z^2(-2\,L + R_1 + R_2) + L\,R_1(R_2 - L) + 2\,L\,z\,(L - R_2))}{\pi \sqrt{-L\,(L - R_1)(L - R_2)(L - R_1 - R_2)}} \tag{2.7}$$

are evaluated and the mode waist

$$w_0 = \sqrt{\frac{\lambda \sqrt{-L\,(L - R_1)(L - R_2)(L - R_1 - R_2)}}{\pi\,(R_1 + R_2 - 2\,L)}} \tag{2.8}$$

is situated at a distance $z_\mathrm{w} = L\,(L - R_2)/(-2\,L + R_1 + R_2)$ from the left mirror.

The intensity distribution I of the cavity mode is derived from the superposition of two counter-propagating Gaussian beams of the same shape

$$E_{\pm}(\mathbf{r},z) = E_0 \frac{w_0}{w(z)} \mathrm{e}^{\frac{-\mathbf{r}^2}{w^2(z)} - i\frac{\pm k\,\mathbf{r}^2}{2\,R(z)} - i\left(\pm k\,z - \arctan\left(\frac{z-z_\mathrm{w}}{z_\mathrm{R}}\right)\right)} \tag{2.9}$$

$$\begin{aligned} I(\mathbf{r},z) &= \frac{1}{2} c_0\,\epsilon_0\,\left|E_+(\mathbf{r},z) + E_-(\mathbf{r},z)\right|^2 \\ &\approx I_0 \frac{w_0^2}{w^2(z)} \mathrm{e}^{\frac{-2\,\mathbf{r}^2}{w^2(z)}} \cos^2\left(k\,(z-z_\mathrm{w}) + \frac{k\,\mathbf{r}^2}{2\,R(z)}\right) \\ &\approx \frac{2\,P}{\pi\,w_0^2} \mathrm{e}^{-\frac{2}{w_0^2}(x^2+y^2)} \cos^2\left(k\,(z-z_\mathrm{w})\right) \\ &\approx P\,\eta^2(x,y,z). \end{aligned} \tag{2.10}$$

The approximation is enabled by the assumptions that the waist is not too large compared to the wavelength, $w_0 \approx 4\,\lambda$ and the cavity is operated well within Rayleigh range $z_\mathrm{R} = \frac{\pi\,w_0^2}{\lambda} > z - z_\mathrm{w}$. Further terms are the radial coordinate $r^2 = x^2 + y^2$, the wave front radius of curvature $R(z) = (z - z_\mathrm{w})\left(1 + \frac{z_\mathrm{R}^2}{(z-z_\mathrm{w})^2}\right)$ and the nominal intensity $I_0 = \epsilon_0\,c_0\,E_0\,E_0^*/2 = \frac{2\,P}{\pi\,w_0^2}$ that is related to the circulating optical power P of a Gaussian beam propagating with vacuum speed of light c_0 and dielectric constant ϵ_0. The optical mode function

$$\eta^2(\mathbf{r}) = \eta^2(x,y,z) = \frac{2}{\pi\,w_0^2} \mathrm{e}^{-\frac{2}{w_0^2}(x^2+y^2)} \cos^2\left(k\,(z-z_\mathrm{w})\right) \tag{2.11}$$

contains a Gaussian distribution in the transversal x-y-plane expressed by

$$\eta^2(x_i) = \sqrt{\frac{2}{\pi\,w_0^2}}\,\mathrm{e}^{\frac{-2(x_i - x_{i,0})^2}{w_0^2}} \tag{2.12}$$

which obeys the normalization

$$\int_{-\infty}^{\infty} \eta^2(x_i)\,\mathrm{d}x_i = 1 \tag{2.13}$$

for each coordinate $x_i = x, y$ separately.

Fabry-Pérot cavity

A formalism well suited to simulate Fabry-Pérot cavities is transfer matrices as they model the propagation of the electric field through layered media.
An electromagnetic wave of wave vector $k = 2\,\pi/\lambda$ propagating a distance l through dielectric material of refractive index n collects an additional phase of $-i\,k\,n\,l$ as sketched in figure 2.3(a). The matrix

$$\mathbf{P}(n,l,k) = \begin{pmatrix} \mathrm{e}^{i\,k\,n\,l} & 0 \\ 0 & \mathrm{e}^{-i\,k\,n\,l} \end{pmatrix} \tag{2.14}$$

connects the fields on the left side $\mathbf{E}_1 = (E_{1\mathrm{R}}, E_{1\mathrm{L}})$ to the fields on the right side $\mathbf{E}_2 = (E_{2\mathrm{R}}, E_{2\mathrm{L}})$ through $\mathbf{E}_1 = \mathbf{P}(n,k,l)\,\mathbf{E}_2$.
At a dielectric boundary the electric field is reflected and transmitted as illustrated in figure 2.3(b). Fields and refractive indexes on the right or left side of the boundary are marked with indexes 1 or 2, respectively. Fields propagating to the right or left carry the additional indexes R or L, respectively. The Fresnel formulas for normal incidence provide the coefficients of transmittance $t_{ab} = i\frac{2\,n_a}{n_a+n_b}$ and reflectance $r_{ab} = \frac{n_a-n_b}{n_a+n_b}$, where a and $b \neq a$ are 1 or 2. The matrix

$$\mathbf{M}(t,r) = \frac{1}{t}\begin{pmatrix} 1 & r \\ r & -1 \end{pmatrix} \tag{2.15}$$

expresses the fields on the left side by the fields on the right side.

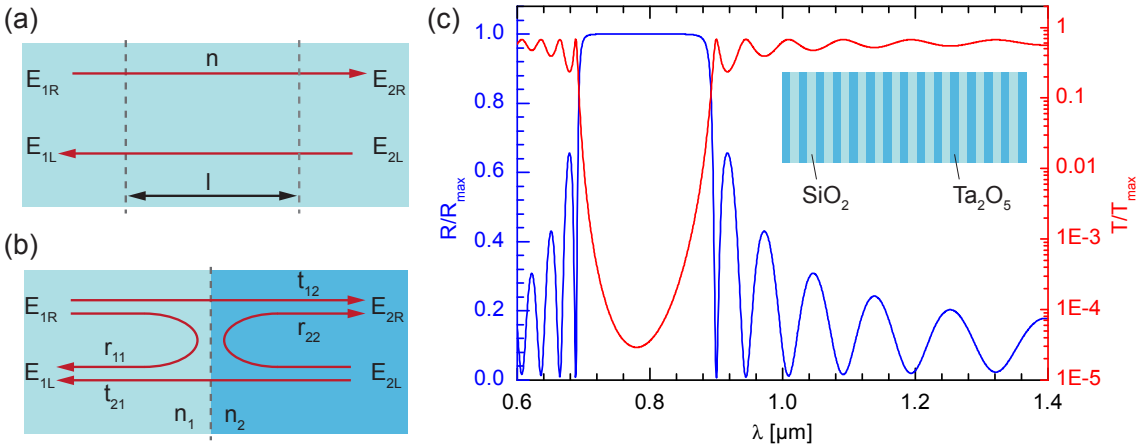

Figure 2.3: Propagation of the electric field (a) through dielectric media and (b) across a dielectric boundary. (c) Simulation of the normalized reflection R/R_{max} (blue) and transmission T/T_{max} (red) of a laser mirror in linear and logarithmic scale, respectively. The mirror, formed by a dielectric layer stack consisting of 29 quarter wave layers of alternating tantalium pentoxide (Ta_2O_5) and silicon dioxide (SiO_2) as sketched in the inset, is simulated by repeated multiplication of the matrices illustrated in (a) and (b).

Propagation of light through layered dielectric media can thus be simulated by multiplying matrices $\mathbf{M}$ and $\mathbf{P}$ with respective parameters and in correct order. Thus a cavity mirror consisting of some tens of quarter wave layers with alternating refractive indexes is described as

$$\mathbf{M_1} = \mathbf{M}_{\mathrm{s},1}(\mathbf{P}_1\,\mathbf{M}_{1,2}\,\mathbf{P}_2\,\mathbf{M}_{2,1})^j\,\mathbf{P}_1\,\mathbf{M}_{1,\mathrm{c}} = \begin{pmatrix} m_{11} & m_{12} \\ m_{21} & m_{22} \end{pmatrix}. \tag{2.16}$$

Here the matrix product of first mirror $\mathbf{M}_1$ is written down, where $P_1 = P(n_1, l_1, k)$ and $M_{1,2} = M(t_{12}, r_{11})$. $\mathbf{M}_{\mathrm{s},1}$ and $\mathbf{M}_{1,\mathrm{c}}$ characterize the boundary between a mirror substrate and the first layer and the last layer and the cavity gap. The term in parentheses

is multiplied j-times and describes the propagation through j pairs of layers, where the indices stand for the refractive indexes of the respective layer. The intensity transmission $T = \frac{n_c}{n_s}|\frac{1}{m_{11}}|^2$ and reflection $R = \frac{m_{12}}{m_{11}}$ of such a system are derived from equation 2.15 and 2.16. Reflection R and transmission T profiles are calculated for an exemplary mirror consisting of 29 quarter wave layers (at $780\,\mathrm{nm}$) of alternating tantalium pentoxide ($n_{\mathrm{TaO}} = 2.105$) and silicon dioxide ($n_{\mathrm{SiO}} = 1.455$). In figure 2.3(c) R and T are plotted versus wavelength in linear and logarithmic scale, respectively. The spectra exhibit a broad reflection band from $700\,\mathrm{nm}$ to $880\,\mathrm{nm}$ with minimum of transmission around $780\,\mathrm{nm}$.
The matrix of an empty Fabry-Pérot cavity with a beam propagating freely from left to right cavity mirror can be written as

$$\mathbf{C} = \mathbf{M_1}\mathbf{P}_{\mathrm{c}}\mathbf{M_2}. \tag{2.17}$$

The expression for the transmission of the cavity derived from C is well known from optics text books [Sal91]

$$T(\omega) = \frac{T_{\max}}{1 + (\frac{2\mathcal{F}}{\pi})^2 \sin^2(\frac{\pi\omega}{\omega_{\mathrm{FSR}}})} \tag{2.18}$$

with optical frequency $\omega/2\pi$, free spectral range $\omega_{\mathrm{FSR}}/2\pi = \frac{c}{2L}$ and finesse $\mathcal{F} = \frac{\pi r}{1-r^2}$.

Cavity loss

The finesse relates to optical losses of the cavity mode, which can also be expressed by a damping rate κ describing the decay of the optical energy. The full width at half maximum of the resonance in angular frequency equals κ and

$$\kappa = \omega_{\mathrm{FWHM}} = \frac{\omega_{\mathrm{FSR}}}{\mathcal{F}}. \tag{2.19}$$

The dissipation of the empty cavity is noted as κ_0 throughout this work. Mechanisms that contribute to the cavity linewidth $\kappa/2\pi$ can be found e.g. in reference [Hun10] or in text books like reference [Sie86] and some of them are mentioned here. A dissipation mechanism arising already with the Fabry-Pérot formalism is coupling through mirrors with finite transmission. Thus some of the high intensity cavity light leaks out as it comes in. Absorption in the mirrors or in the material inside the cavity also dissipates energy of the cavity mode. At mirrors with finite radial extension some portion of the Gaussian cavity mode is clipped and limits the cavity finesse. Scattering at imperfect mirrors with certain surface roughness and scattering of light out of the cavity mode by objects inside the cavity obviously extracts optical energy.

Mode Volume

The cavity mode volume V_m is the volume taken by the electromagnetic mode weighted by normalized intensity [Sri06]

$$V_\mathrm{m} = \frac{\int \epsilon_\mathrm{r}(\mathbf{r})|\mathbf{E}(\mathbf{r})|^2 \mathrm{d}^3\mathbf{r}}{\max(\epsilon_\mathrm{r}(\mathbf{r})|\mathbf{E}(\mathbf{r})|^2)} \approx \pi/4 w_0^2 L. \tag{2.20}$$

The approximation holds for Fabry-Pérot cavities that are shorter than the Rayleigh range z_R and for optical TEM_{00} modes, where the intensity has radial Gaussian distribution and modulates axially like $\cos^2(k\,z)$ analog to equation 2.10 [Hun10].

Cavity with dielectric sheet

Putting a dielectric sheet of thickness d with transfer matrix

$$\mathbf{D} = \mathbf{M}_\mathrm{c,d}\mathbf{P}_\mathrm{d}\mathbf{M}_\mathrm{d,c} \tag{2.21}$$

in between the mirrors at position z_0, the cavity matrix now looks like

$$\mathbf{C} = \mathbf{M}_\mathrm{c,2}\mathbf{P}_\mathrm{c2}\mathbf{D}\mathbf{P}_\mathrm{c1}\mathbf{M}_\mathrm{c,1}. \tag{2.22}$$

Upon moving the sheet along the cavity axis z, the cavity resonance frequency and the transmission vary periodically. Figure 2.4 shows plots of these values resulting from calculations for a cavity with a $50\,\mathrm{nm}$ thick sheet of silicon nitride ($n_\mathrm{SiN} = 2.2$) inserted at z_0. The cavity resonance frequency ω_c changes by a few megahertz upon a position shift of only $2\,\mathrm{pm}$ which can be seen in the plot of figure 2.4(a). These resonance curves are calculated close to the minimum of $\omega_\mathrm{c}(\Delta z_0)/2\pi$ at $\Delta z_0 = -70\,\mathrm{nm}$. The transmission (red) and resonance frequency (blue) of the cavity exhibit quarter and half wavelength periodical dependence, respectively, upon the position of the sheet as shown in figure 2.4(b).

2.1.2 Mechanics

Doubly clamped flexural beams with circular and rectangular cross-section potentially subjected to tensile stress are relevant structures for this work. In order to model their vibrational properties Euler Bernoulli beam theory is applied and results in formulas for mode shape, stiffness and resonance frequency. The description of the flexural motion of an extended beam is simplified by using the construct of the effective mass as point mass in the model of the harmonic oscillator. Dissipation is easily included in the harmonic oscillator, and thus spectral distributions of the vibration of real mechanical resonators can be derived with few parameters. Calculations in this section follow calculations detailed in reference [Wea90, Cle03, Kar08, Ane10a, Pin99] and is partially presented in reference [Sta13] and supplementary information.

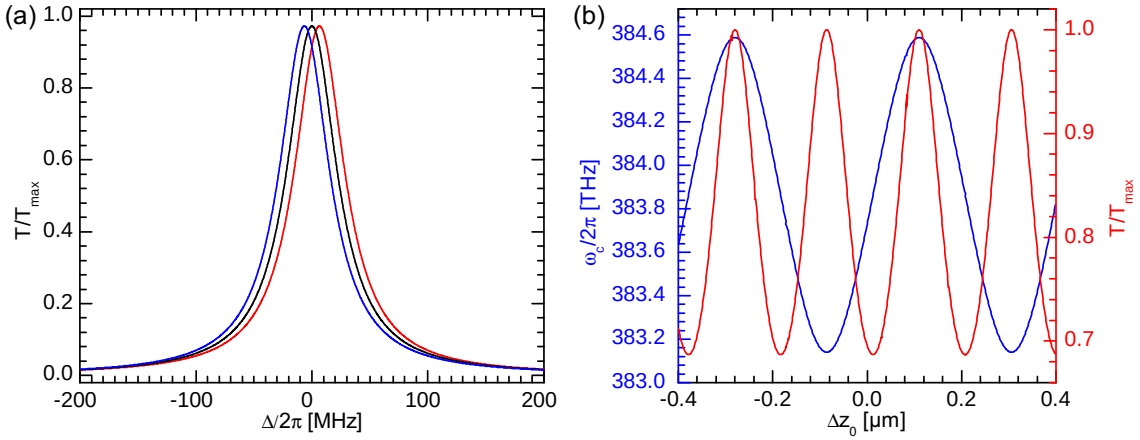

Figure 2.4: Simulation of a cavity containing a $50\,\mathrm{nm}$ thick dielectric layer of silicon nitride (Si_3N_4) with refractive index $n_{SiN} = 2.2$ at position z_0. (a) Normalized transmission versus laser cavity detuning $\Delta = \omega_l - \omega_c$ for three positions separated by steps of $2\,\mathrm{pm}$ (around $\Delta z_0 = -70\,\mathrm{nm}$ in (b)). (b) Resonance frequency $\omega_c/2\pi$ (blue) and normalized transmission T/T_{max} (red) as function of the differential position of the dielectric layer Δz_0.

Beam theory

Continuous elastic theory provides a formalism to calculate deflection properties and frequency response of extended mechanical objects subjected to different static and dynamic loads. Geometry, material parameters and respective boundary conditions are included and play a significant role.

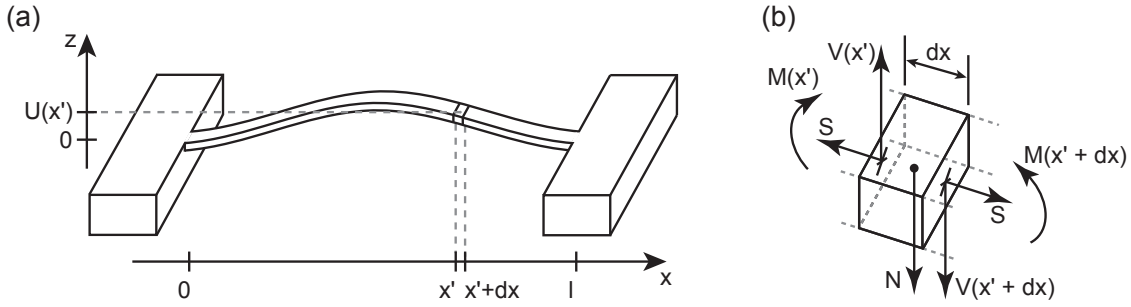

Figure 2.5: (a) Sketch of a deflected elastic beam. (b) Free-body diagram of a segment of the beam with acting forces and moments.

The dynamic displacement $U(x)$ in z-direction of a homogeneous flexural beam of length l is calculated by balancing moments and forces acting on an infinitesimal segment of length $\mathrm{d}x$ as illustrated in figure 2.5(a) and (b). Therefore the bending moment $M = E\,I\,\frac{\partial^2 U}{\partial x^2}$, shear force $V (= \frac{\partial M}{\partial x})$, inertial force $N = \rho\,A\,dx\,\frac{\partial^2 U}{\partial t^2}$ and tensile stress $S = \sigma\,A$ are considered. This yields the Euler-Bernoulli equation of an elastic flexural beam under tensile stress, which is driven by a time and position dependent reduced force $f(x,t)$

$$\frac{\partial^2}{\partial x^2} E\,I \frac{\partial^2 U(x,t)}{\partial x^2} - \sigma\,A \frac{\partial^2 U(x,t)}{\partial x^2} + \rho\,A \frac{\partial^2 U(x,t)}{\partial t^2} = f(x,t). \tag{2.23}$$

The first and second terms account for restoring forces caused by the elastic deformation of the beam and the tensile stress, respectively, where the third term stems from the inertial force of the segment. Further parameters in equation 2.23 are the Young's module of elasticity E, axial tensile stress σ, the mass density ρ, the cross-section area A and the area moment of inertia I. I becomes $I_{\text{circ}} = \frac{\pi}{4} r^4$ for circular cross-section of radius r and $I_{\text{rect}} = \frac{1}{12} d^3\,w$ for rectangular cross-section with dimensions parallel d and perpendicular w to the motional deflection. The time and position dependent deflection reads

$$U(x,t) = \sum_m q_m(t)\,\phi_m(x). \tag{2.24}$$

$U(x,t)$ superimposes the product of the time dependent amplitude $q_m(t)$ and the position dependent mode shape function $\phi_m(x)$ for all modes m. Two important properties of the mode shape functions are orthogonality

$$\int_0^l \phi_m(x)\,\phi_n(x)\,\mathrm{d}x = 0 \quad \text{for} \quad m \neq n \tag{2.25}$$

as well as the identity relation

$$\int_0^l \phi_n(x) \frac{\partial^4 \phi_n(x)}{\partial x^4}\,\mathrm{d}x = \int_0^l \left(\frac{\partial^2 \phi_n(x)}{\partial x^2} \right)^2 \mathrm{d}x. \tag{2.26}$$

To solve equation 2.23 it is sufficient to derive the solution of the homogeneous differential equation where $f(x,t) = 0$ for one mode n first. The harmonic ansatz $q_n(t) = \mathrm{e}^{-i\,\Omega_n\,t}$ cancels time dependence and for the real valued mode shape function the ansatz

$$\phi_n(x) = a_n \cos(\beta_n x) + b_n \sin(\beta_n x) + c_n \cosh(\beta_n x) + d_n \sinh(\beta_n x) \tag{2.27}$$

is chosen with coefficients $a_n, \ldots d_n$ and spatial frequency β_n.
Boundary conditions determine the coefficients and lead to equations assigning β_n. Two cases of boundary conditions for doubly-clamped structures are considered.

First, for an elastic beam where stress is irrelevant ($\sigma \approx 0$) with fixed, rigid clamping points (no deflection and no slope for ϕ at $x = 0$ and $x = l$) boundary conditions are

$$\phi_n(0) = \phi_n(l) = \left.\frac{\mathrm{d}\phi_n(x)}{\mathrm{d}x}\right|_{x=0} = \left.\frac{\mathrm{d}\phi_n(x)}{\mathrm{d}x}\right|_{x=l} = 0. \tag{2.28}$$

Equations 2.27 and 2.28 lead to mode shape roots $\beta_n\,l$ and coefficient ratios a_n/b_n ($c_n = -a_n$, $d_n = -b_n$). Values are given in table 2.1 for the first five modes and $a_n = 1$ is chosen for all n [Wea90].

The resonance frequencies $\Omega_n/2\pi$ of the modes are obtained by putting ϕ into the homogeneous version of equation 2.23,

$$\Omega_n = \frac{(\beta_n l)^2}{l^2}\sqrt{\frac{E I}{\rho A} + \frac{\sigma l^2}{\pi^2 n^2 \rho}}. \tag{2.29}$$

For the purely elastic beam ($\sigma = 0$), equation 2.29 yields

$$\Omega_n = \frac{(\beta_n l)^2}{l^2}\sqrt{\frac{E I}{\rho A}}, \tag{2.30}$$

and values for $\beta_n l$ are listed in table 2.1.

Second, for a string like, doubly-clamped beam which is exposed to large tensile stress rigid clamps are treated to be simply supported (no deflection and no curvature at the clamps)

$$\phi_n(0) = \phi_n(l) = \left.\frac{\mathrm{d}^2\phi_n(x)}{\mathrm{d}x^2}\right|_{x=0} = \left.\frac{\mathrm{d}^2\phi_n(x)}{\mathrm{d}x^2}\right|_{x=l} = 0. \tag{2.31}$$

Thus $\beta_n l = \pi n$, $b_n = 1$ and all other coefficients $a_n = c_n = d_n = 0$ for the stressed beam and the resonance frequencies are again obtained form the homogeneous form of equation 2.23

$$\Omega_n = \frac{\pi n}{l}\sqrt{\frac{\sigma}{\rho}}. \tag{2.32}$$

For the case of stress dominated restoring force $\beta_n l = \pi n$ and equation 2.32 is an approximation of equation 2.29 where $E I/A \ll \sigma(l/(\pi n))^2$ in this regime.

Table 2.1: Numerical values of $\beta_n l$ and a_n/b_n for the first five modes n of the rigidly doubly clamped elastic beam.

mode index	n	1	2	3	4	5
mode shape roots	$\beta_n l$	4.7300	7.8532	10.9956	14.1372	17.2788
coefficient ratio	a_n/b_n	-1.0178	-0.9992	-1.0000	-1.0000	-1.0000

Effective mass

The mathematical construct of the effective mass aims at reducing the full differential equation of an elastic beam (see equation 2.23) to the simple equation of motion of a harmonic oscillator. While elastic beam theory describes the time-dependent deflection

of each point along the beam, the harmonic oscillator simplifies the calculation to the case of a point-mass oscillating at a specific location on the beam. The effective mass thus describes the fraction of the beam's total mass corresponding to the amplitude of the harmonic oscillator which is equivalent to the deflection of the beam. This solution is more practical to work with, but requires some preliminary work. As will be made clear, the effective mass depends on the reference position along the beam, the geometry of the deflection measurement device and the distribution of the driving force. Thus the effective mass depends on the selected driving and detection schemes. Calculations in this section follow calculations detailed in reference [Wea90, Cle03, Kar08, Ane10a, Pin99].

Multiplying equation 2.23 (now with $\sigma = 0$) by the shape function $\phi_n(x)$ for mode n, integrating over the beam length l and exploiting equations 2.24 to 2.26 yields

$$E\,I\,q_n(t)\int_0^l\left[\frac{\partial^2\phi_n(x)}{\partial x^2}\right]^2\mathrm{d}x+\rho\,A\,\ddot{q}_n(t)\int_0^l\phi_n^2(x)\,\mathrm{d}x=\int_0^l f(x,t)\,\phi_n(x)\,\mathrm{d}x. \quad (2.33)$$

This looks like a harmonic oscillator

$$m_n'\,\ddot{q}_n(t)+k_n'\,q_n(t)=\int_0^l f(x,t)\,\phi_n(x)\,\mathrm{d}x \quad (2.34)$$

with mass and spring constant

$$m_n'=\rho\,A\int_0^l\phi_n^2(x)\,\mathrm{d}x=m\int_0^1\phi_n^2(\xi)\,\mathrm{d}\xi, \quad (2.35a)$$

$$k_n'=E\,I\int_0^l\left[\frac{\partial^2\phi_n(x)}{\partial x^2}\right]^2\mathrm{d}x=\frac{E\,I}{l^3}\int_0^1\left[\frac{\partial^2\phi_n(\xi)}{\partial\xi^2}\right]^2\mathrm{d}\xi, \quad (2.35b)$$

introducing normal coordinates $\xi = x/l$. For each mode n the mode function $\phi_n(\xi)$ is normalized to 1 such that $|\phi_n(\xi)| \leq 1$ on the interval $\xi \in [0;1]$.

In most physical deflection measurement devices the detection is not carried out at a single point but rather distributed over a certain region along the beam. To account for that the mode shape function $\phi_n(\xi)$ is convoluted with a distribution, e.g. $\eta^2(\xi)$ from equation 2.12 where $\eta^2(\xi)$ obeys the normalization

$$\int_{-\infty}^{\infty}\eta^2(\xi)\,\mathrm{d}\xi=1. \quad (2.36)$$

Thus the measured deflection $u_n(t)$ reads

$$u_n(t)=q_n(t)\int_0^1\phi_n(\xi)\eta^2(\xi)\,\mathrm{d}\xi. \quad (2.37)$$

Multiplying equation 2.34 with the integral on the right hand side of equation 2.37 gives

$$m_n' \ddot{u}_n(t) + k_n' u_n(t) = \int_0^l f(x,t)\,\phi_n(x)\,\mathrm{d}x \int_0^1 \phi_n(\xi)\eta^2(\xi)\,\mathrm{d}\xi. \tag{2.38}$$

As detailed in reference [Pin99], for the case of thermal forces driving the flexural motion, $f(x,t)$ is expressed in normal coordinate ξ yielding $f(\xi,t) = F(t)\eta^2(\xi)$, and the effective harmonic oscillator becomes

$$m_{\mathrm{eff},n}\,\ddot{u}_n(t) + k_{\mathrm{eff},n}\,u_n(t) = F(t). \tag{2.39}$$

The effective mass[1] $m_{\mathrm{eff},n}$ and the effective spring constant $k_{\mathrm{eff},n}$,

$$m_{\mathrm{eff},n} = m\frac{\int_0^1 \phi_n^2(\xi)\,\mathrm{d}\xi}{\left[\int_0^1 \phi_n(\xi)\eta^2(\xi)\,\mathrm{d}\xi\right]^2} \quad \text{and} \tag{2.40a}$$

$$k_{\mathrm{eff},n} = \frac{E\,I}{l^3}\frac{\int_0^1 \left[\frac{\partial^2\phi_n(\xi)}{\partial\xi^2}\right]^2 \mathrm{d}\xi}{\left[\int_0^1 \phi_n(\xi)\eta^2(\xi)\,\mathrm{d}\xi\right]^2}, \tag{2.40b}$$

comprise the inertial and elastic properties of the whole beam oscillating in mode n. This allows modeling the dynamics of the beam with a simple harmonic oscillator. A valid calibration of the measured amplitude is possible with the knowledge of the measurement distribution.

Harmonic oscillator

Here, since the deflection profile is no longer interesting $u(t)$ is replaced by $z(t)$. In order to apply the effective mass to a more realistic model for a single mode of an oscillator, a viscous damping term $\gamma_n\,\dot{z}(t)$ is added to equation 2.39

$$\ddot{z}(t) + \gamma\,\dot{z}(t) + \Omega_n^2\,z(t) = F(t) \tag{2.41}$$

where $\Omega_n^2 = k_{\mathrm{eff},n}/m_{\mathrm{eff},n}$. Fourier transformation with $\hat{z}(\Omega) = \mathrm{FT}(z(t)) = (2\pi)^{-1/2}\int_{-\infty}^{\infty} z(t)\mathrm{e}^{-i\Omega t}\,\mathrm{d}t$ and $\hat{F}(\Omega) = \mathrm{FT}(F(t))$ applied to equation 2.41 gives

$$\hat{z}(\Omega) = \chi(\Omega)\,\hat{f}(\Omega) = \frac{\hat{f}(\Omega)}{m(\Omega_n^2 - \Omega^2 + i\,\Omega\,\gamma_n)}. \tag{2.42}$$

The displacement spectrum of the oscillator

[1] For the case of a point-like probe $\eta^2(\xi) = \delta(\xi_0)$ at the maximum deflection ξ_0 the well-established form $m_{\mathrm{eff}} = m\frac{\int_0^1 \phi_n^2(\xi)\,\mathrm{d}\xi}{\phi_n^2(\xi_0)}$ is recovered [Wea90].

$$S_{zz}(\Omega) = \frac{1}{\sqrt{2\,\pi}} \int_{-\infty}^{\infty} R_{zz}(t)\, \mathrm{e}^{-i\,\Omega\,t}\, \mathrm{d}t = |\chi(\Omega)|^2 S_{FF}(\Omega) \tag{2.43}$$

that is the Fourier transform of the autocorrelation function of the displacement $R_{zz}(t) = \int_{-\infty}^{\infty} z(t)\, z(t-t')\, \mathrm{d}t'$ is also expressed through the susceptibility $\chi(\Omega)$ (defined in equation 2.42) and the spectral density of the driving force $S_{FF}(\Omega)$ [Cle10]. The mean squared amplitude

$$\left\langle z^2 \right\rangle = \int_0^{\infty} S_{zz}(\Omega) \mathrm{d}\Omega \tag{2.44}$$

is derived form the oscillator spectrum.

Dissipation

The viscous damping term in equation 2.41 accounts for dissipation of oscillatory energy into the environment. The initial amplitude z_0 of an excited, non-driven ($F(t) = 0$) oscillator decays with time like

$$z(t) = \mathrm{FT}^{-1}(\hat{z}(\Omega)) \approx z_0\, \mathrm{e}^{-\frac{\gamma_n}{2} t} \mathrm{e}^{-i\,\Omega_n\,t} \tag{2.45}$$

which is an approximation for low dissipation, e.g. $\gamma_n \ll \Omega_n$, and valid for positive t. Thus in natural logarithmic scale the oscillatory energy which is proportional to $z^2(t)$ decays in time linearly with slope $-\gamma_n$. The quality factor, that relates the energy stored by the oscillation to the energy dissipated per cycle, can be expressed as

$$Q_n \approx \frac{\Omega_n}{\gamma_n}. \tag{2.46}$$

Dissipation in mechanical nanostructures stems e.g. from thermoelastic effects [Lif00] built-in two-level-systems [Fau14], surface coating [Yu12], the surrounding gaseous environment [Ver08b], losses at the clamping regions [Rie14] and because of polarization in dielectric fields [Rie12]. Further dissipation mechanisms relevant for nanomechanical resonators are mentioned in reviews like reference [Eki05] and reference [Imb14].

2.1.3 Brownian Motion

The equipartition theorem states that in thermal equilibrium all degrees of freedom of a system have the same mean energy. Especially for a non-driven mechanical oscillator that means all modes vibrate with thermal energy

$$\frac{1}{2} k_{\mathrm{B}}\, T = \frac{1}{2} k_{\mathrm{eff},n} \left\langle z^2 \right\rangle, \tag{2.47}$$

with Boltzmann constant k_B, temperature T, mean squared amplitude $\langle z^2 \rangle$ (see equation 2.44), effective spring constant $k_{\text{eff},n} = \Omega_n^2 \, m_{\text{eff},n}$ and effective mass $m_{\text{eff},n}$ (see equations 2.40). Thus the equipartition theorem provides a common means to calibrate measured data of mechanical resonances to motional amplitudes [Met04].

2.1.4 Heating the sample by absorption

In the experimental configuration where the sample is exposed to an intense laser field heating of the sample by photoabsorption has to be considered. This is illustrated in figure 2.6(a) for a doubly clamped, suspended beam (gray) in the optical cavity mode (red). For simplicity the beam center coincides with the center of the optical mode at $x = 0$. The beam is exposed to the light field of the cavity and absorbs energy proportional to the intensity distribution of the overlapping optical mode. The heat generated in the beam flows to the clamping points (at $x = \pm l/2$) that are in equilibrium with the environment at temperature T_0.

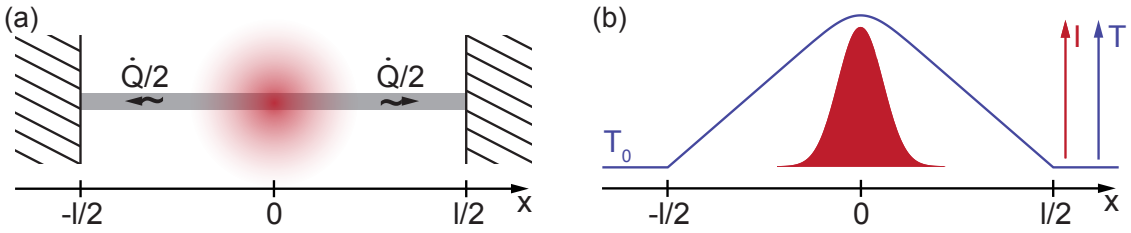

Figure 2.6: Illustration of heating a doubly clamped, suspended beam (gray) in the optical cavity. (a) The beam is exposed to the light field of the cavity and absorbs energy locally proportional to the intensity distribution of the optical mode (red). The heat generated in the beam flows to the clamping points (at $x = \pm l/2$) that are in equilibrium with the environment at temperature T_0. (b) The intensity distribution of the cavity mode (red) is plotted qualitatively together with the resulting temperature profile (blue) along the beam.

Starting from an ordinary heat transfer model $\dot{Q} = \kappa_T \, A \, \Delta T / \Delta l$ for the heat flow $\dot{Q}$ through a homogeneous sample section of length Δl, cross-section A and with thermal conductivity κ_T the temperature difference ΔT across the section reads

$$\Delta T = \frac{\Delta l \, \dot{Q}}{A \, \kappa_T}. \tag{2.48}$$

In thermal steady-state equilibrium $\dot{Q}$ at beam position x' is equal to the absorbed optical power between x' and the cavity mode center at $x' = 0$. For positive x' the heat flow follows an error-functional shape

$$\dot{Q} = \left(\frac{\kappa}{\kappa_0} - 1\right) \frac{P_t}{2} \operatorname{erf}\left(\sqrt{2} \frac{x'}{w_0}\right) \tag{2.49}$$

that is the integral of the transverse cavity mode profile $\eta^2(x')$ from equation 2.12. The optical power lost under the influence of the sample is given by the expression $(\kappa/\kappa_0 -$

$1)P_\mathrm{t}$ where κ_0 and κ denote the intrinsic linewidth of the empty cavity and the linewidth of the cavity with extra damping caused by the presence of the sample. Substituting equation 2.49 into equation 2.48 with differentials ($\Delta T \mapsto \mathrm{d}T$, $\Delta l \mapsto \mathrm{d}x'$) and integrating from x to the clamping point at $l/2$ yields the temperature profile $T(x)$ along the beam

$$T(x) = \frac{1}{A\,\kappa_\mathrm{T}}\left(\frac{\kappa}{\kappa_0} - 1\right)P_\mathrm{t}\int_x^{l/2} \mathrm{erf}\left(\sqrt{2}\frac{x'}{w_0}\right)\mathrm{d}x'. \tag{2.50}$$

The temperature profile along the beam and the intensity distribution of the cavity mode are qualitatively sketched in figure 2.6(b) in blue and red, respectively. The temperature decays linearly towards the clamps as soon as the heating influence of the optical mode becomes negligible.

2.1.5 Couplings

A mechanical element that interacts with the light field of a cavity is parametrically coupled to the cavity. This optomechanical coupling is distinguished by its either dispersive or dissipative nature meaning a shift in position of the mechanical element causes a shift in frequency or linewidth of the cavity, respectively. Relating this coupling to the zero point motion of the mechanical element defines the vacuum optomechanical coupling.

Dispersive optomechanical Coupling

The optomechanical coupling $g_\omega/2\pi$ for only dispersive interaction of the mechanical element with the optical mode of a cavity is defined as the cavity resonance frequency shift per mechanical deflection [Vit07, Tho08, Wei10, Asp14, Cha10]

$$g_\omega = \frac{\partial\omega_\mathrm{c}}{\partial z}. \tag{2.51}$$

The shift of the cavity frequency $\delta\omega_c/2\pi$ upon a small change of a dielectric volume inside the cavity is expressed in cavity perturbation theory by comparing the energies of the polarization field in the dielectric volume, say the perturbation of the cavity, with the field of the unperturbed cavity [Cha10]. Thus

$$\frac{\delta\omega_\mathrm{c}}{\omega_0} = -\frac{1}{2}\frac{\int \delta\mathbf{P}(\mathbf{r})\,\mathbf{E}^*(\mathbf{r})\,\mathrm{d}^3\mathbf{r}}{\int \epsilon_0\,|\mathbf{E}(\mathbf{r})|^2\,\mathrm{d}^3\mathbf{r}}, \tag{2.52}$$

where $\omega_0/2\pi$ is the frequency of the unperturbed cavity, electric field amplitude $\mathbf{E}(\mathbf{r})$, polarization $\delta\mathbf{P}(\mathbf{r}) = \epsilon_0(\epsilon_\mathrm{r}(\mathbf{r}) - 1)\mathbf{E}(\mathbf{r})$, dielectric constant ϵ_0 and spacial dependent permittivity $\epsilon_\mathrm{r}(\mathbf{r})$. A detailed derivation of equation 2.52 is e.g. given in reference [Wal60]. It is assumed that $\epsilon_\mathrm{r}(\mathbf{r}) = \epsilon_\mathrm{r}$ is constant in the volume of the dielectric perturbation V_diel

and only here $(\epsilon_\mathrm{r}(\mathbf{r}) - 1)$ is non-zero. Thus the integral in the numerator of equation 2.52 integrates only over V_diel. In the limit of infinitesimal changes $\delta\omega_\mathrm{c} \mapsto \partial\omega_\mathrm{c}$ and

$$g_\omega = -\frac{\omega_0}{2}\frac{\partial}{\partial z}\frac{\int_{V_\mathrm{diel}} \epsilon_0\,(\epsilon_\mathrm{r}-1)\,|\mathbf{E}(\mathbf{r})|^2\,d^3\mathbf{r}}{\int \epsilon_0\,|\mathbf{E}(\mathbf{r})|^2\,\mathrm{d}^3\mathbf{r}}. \tag{2.53}$$

The denominator is the product of $2\,I_0/c_0$ with the optical mode volume V_m of the undisturbed cavity and constant (c.f. equation 2.20). The electric field $\mathbf{E}(\mathbf{r})$ is composed of the polarization vector $\mathbf{E_0}$ and spatial field distribution $\eta(\mathbf{r})$ (time dependence is neglected here). The intensity is $I(\mathbf{r})$ with maximal value $I_0 \propto E_0^2$. For small coupling ω_0 can be approximated by ω_c.

$$\mathbf{E}(\mathbf{r}) = \mathbf{E_0}\,\eta(\mathbf{r}) \tag{2.54}$$

$$|\mathbf{E}|^2(\mathbf{r}) = \frac{2}{c_0\,\epsilon_0}\,I(\mathbf{r}) = \frac{2\,P}{c_0\,\epsilon_0}\,\eta^2(\mathbf{r}) \tag{2.55}$$

$$g_\omega = -\frac{\pi\,\omega_\mathrm{c}\,(\epsilon_\mathrm{r}-1)\,w_0^2}{2\,V_\mathrm{m}}\,\frac{\partial}{\partial z}\int_{V_\mathrm{diel}} \eta^2(\mathbf{r})\,\mathrm{d}^3\mathbf{r} \tag{2.56}$$

For a simplified case that is assumed here, the optical mode profile is Gaussian and the interaction takes place at the mode waist w_0 on a range far smaller than the Rayleigh range. For this reason the wavefront curvature can be neglected and it is fairly save to approximate the intensity distribution along the cavity axis z by a cosine as it is also done in equation 2.10. In the x-y-plane the intensity follows a Gaussian distribution and a periodic modulation in z direction (see equation 2.12)

$$\eta^2(\mathbf{r}) = \eta^2(x,y,z) \approx \frac{1}{\pi\,w_0^2}\,\mathrm{e}^{-\frac{2}{w_0^2}(x^2+y^2)}\,(1-\sin(2\,k\,(z_0+z)), \tag{2.57}$$

where k is the wave number and z_0 is the position of the perturbing element. The integral over V_diel in Eq. 2.56 is the overlap integral between the optical mode and the (perturbing) mechanical element. Thus

$$g_\omega = -\frac{\omega_\mathrm{c}\,(\epsilon_\mathrm{r}-1)}{2\,V_\mathrm{m}}\,\frac{\partial}{\partial z}\int_{V_\mathrm{diel}} \mathrm{e}^{-2\,\frac{x^2+y^2}{w_0^2}}\,(1-\sin(2\,k\,(z_0+z)))\,\mathrm{d}^3\mathbf{r} \tag{2.58}$$

$$= -\frac{\omega_\mathrm{c}\,(\epsilon_\mathrm{r}-1)}{2\,V_\mathrm{m}}\int_{V_\mathrm{diel}} \mathrm{e}^{-2\,\frac{x^2+y^2}{w_0^2}}\,\frac{\partial}{\partial z}(1-\sin(2\,k\,(z_0+z)))\,\mathrm{d}^3\mathbf{r} \tag{2.59}$$

and the integral in equation 2.56 can be separated by coordinates. With the assumptions that the extension of the mechanical element in y-z-plane (i.e. its cross-section A) is much smaller than the z-periodicity of the optical mode the field across the element can be considered constant.

In the static case the deflection of the mechanical element is considered constant everywhere and when the length l of the mechanical element is larger than the extension of the optical mode ($l \gg 2\,w_0$) the distribution can be approximated by extending the integration boundaries $\int_0^l \exp(-2\,(x-l/2)^2/w_0^2)\,\mathrm{d}x \approx \int_{-\infty}^{\infty} \exp(-2\,x^2/w_0^2)\,\mathrm{d}x = \sqrt{\pi/2}\,w_0$ such that

$$g_{\omega,\text{static}} = \frac{\omega_\text{c}\,k\,(\epsilon_\text{r}-1)\,A}{2\,V_\text{m}}\,\mathrm{e}^{-2\,\frac{y_0^2}{w_0^2}}\cos(2\,k\,z_0)\int_0^l \mathrm{e}^{-2\,\frac{(x-l/2)^2}{w_0^2}}\,\mathrm{d}x \tag{2.60}$$

$$\approx \frac{\sqrt{\pi}\,\omega_\text{c}\,k\,(\epsilon_\text{r}-1)\,w_0\,A}{2\sqrt{2}\,V_\text{m}}\,\mathrm{e}^{-2\,\frac{y_0^2}{w_0^2}}\cos(2\,k\,z_0). \tag{2.61}$$

Considering the dynamics of the system where the mechanical element oscillates in a mode n around a mean position z_0 the spatially dependent deflection is explained by $\phi_n(\mathbf{r})$ (as introduced in section 2.1.2). Hence the contribution of this deflection to g_ω varies with position, too. It is maximal when the the optical mode is centered on an anti-node and zero for centering on a node of the mechanical mode. To account for that the mode shape function $\phi(\mathbf{r})$ has to be considered when the derivative $\partial/\partial z$ is formed and convoluted with the optical mode function. For deflections much smaller than the wavelength, $\phi_n(\mathbf{r})$ can simply be multiplied to the optical mode distribution in the integral of equation 2.56 and for the case of a one dimensional, string like resonator $\phi_n(\mathbf{r}) \mapsto \phi_n(x)$

$$\begin{aligned} g_{\omega,\text{dynamic}} &= -\frac{\omega_\text{c}\,(\epsilon_\text{r}-1)}{2\,V_\text{m}}\int_{V_\text{diel}} \phi_n(\mathbf{r})\mathrm{e}^{-2\,\frac{x^2+y^2}{w_0^2}}\,\frac{\partial}{\partial z_0}(1-\sin(2\,k\,z_0)\,\mathrm{d}^3\mathbf{r} \\ &= \frac{\omega_\text{c}\,k\,(\epsilon_\text{r}-1)}{V_\text{m}}\cos(2\,k\,z_0)\int_{V_\text{diel}} \phi_n(\mathbf{r})\mathrm{e}^{-2\,\frac{x^2+y^2}{w_0^2}}\,\mathrm{d}^3\mathbf{r} \\ &\approx \frac{\omega_\text{c}\,k\,(\epsilon_\text{r}-1)\,A}{V_\text{m}}\,\mathrm{e}^{-2\,\frac{y_0^2}{w_0^2}}\cos(2\,k\,z_0)\int_0^l \phi_n(x)\,\mathrm{e}^{-2\,\frac{(x-l/2)^2}{w_0^2}}\,\mathrm{d}x. \end{aligned} \tag{2.62}$$

The last approximation is valid for a long and thin mechanical element whose extensions in z and y can be neglected compared to the wavelength.
The dynamic optomechanical coupling $g_{\omega,\text{dynamic}}$ reduces to g_ω of the static case if a constant deflection of $\phi_n(\mathbf{r}) = 1$ is used. The overlap integral of the mechanical and optical modes contained in $g_{\omega,\text{dynamic}}$ appears squared in the denominator of the effective mass (see equation 2.40a), too, which will be exploited on the following pages.

Dissipative optomechanical coupling

A mechanical element in the cavity does not only interact dispersively with the optical mode but it also contributes to loss affecting the cavity dissipation rate κ. Usually κ depends on the position of the mechanical element. The change in cavity dissipation per mechanical deflection z is defined as dissipative optomechanical coupling $g_\kappa/2\pi$ as [Li09, Els09, Xue11, Bia11]

$$g_\kappa = \frac{\partial \kappa}{\partial z}. \tag{2.63}$$

Again it has to be distinguished between static and dynamic coupling. For the dynamic case, of course the mechanical mode shape has to be considered as this is described above for g_ω in equation 2.62. The static coupling approximates the dynamic case rather well as long as the spatial wavelength of the mechanical oscillation is much larger than the optical mode diameter and the optical mode is centered on an anti-node of the mechanical mode. Since this condition is satisfied for the measurements presented later in this work, the dissipation rate and g_κ are determined experimentally by recording the decay rate of the optical mode or the cavity linewidth as function of the position z. This procedure is used throughout this work.

Vacuum optomechanical coupling and effective mass

Vacuum optomechanical coupling g_0 is defined as the product of the optomechanical coupling g_ω and the zero point amplitude $z_{\mathrm{zpf},n}$ of the mechanical oscillator vibrating in the n-th mode.

$$g_0 = g_\omega \, z_{\mathrm{zpf},n} \qquad \text{with} \tag{2.64}$$

$$z_{\mathrm{zpf},n} = \sqrt{\frac{\hbar}{2\, m_{\mathrm{eff},n}\, \Omega_n}}, \tag{2.65}$$

effective vibrational mass $m_{\mathrm{eff},n}$ and mechanical resonance frequency Ω_n [Gor10].
Equation 2.47 is used to calibrate the amplitude in the measured power spectrum $S_{PP}(\omega)\, BW$ of the signal to the Brownian motion amplitude of the oscillator. Starting from the displacement z the measured spectrum is composed as follows: z causes the cavity resonance ω_c to shift by the optomechanical coupling $g_\omega = \partial\omega_\mathrm{c}/\partial z$. With the laser locked on the slope of the cavity resonance (e.g. as described in chapter 3.2.2) the optical power transmitted (or reflected) by the cavity fluctuates by $P_\mathrm{opt} = P_\mathrm{in}\ \partial T(\omega)/\partial\omega|_{\omega_\mathrm{l}}\ g_\omega\, z$. The optical power is converted into a photo voltage $V = g_\mathrm{ti}\, g_\mathrm{sens}\, P_\mathrm{opt}$ by the detector and measured by the spectrum analyzer as electrical power V^2/R with a bandwidth BW. Further terms denote the cavity response $T(\omega)$ (see equation 2.18), laser frequency $\omega_\mathrm{l}/2\pi$, injected laser power P_in, transimpedance gain g_ti, spectral sensitivity g_sens and the electrical impedance $R = 50\Omega$.

$$V = g_\mathrm{ti}\, g_\mathrm{sens}\, P_\mathrm{in}\ \left.\frac{\partial T(\omega)}{\partial\omega}\right|_{\omega_\mathrm{l}}\ g_\omega\, z \tag{2.66}$$

$$P = \chi_\mathrm{zP}^2\, g_\omega^2\, z^2 \qquad \text{with} \tag{2.67}$$

$$\chi_\mathrm{zP} = \frac{g_\mathrm{ti}\, g_\mathrm{sens}}{\sqrt{R}}\, P_\mathrm{in}\ \left.\frac{\partial T(\omega)}{\partial\omega}\right|_{\omega_\mathrm{l}} \tag{2.68}$$

Signal power spectal density $S_{PP}(\omega) = 1/R\, S_{VV}(\omega)$ together with Eq. 2.43 to 2.68 yields a signal spectrum

$$S_{PP}(\Omega)\, BW = \frac{BW}{R} S_{VV}(\Omega) = BW\, \chi_{\text{zP}}^2\, g_\omega^2\, S_{zz}(\Omega) \qquad \text{and} \tag{2.69}$$

$$S_{zz}(\Omega) = \frac{1}{BW\, \chi_{\text{zP}}^2\, g_\omega^2}\, S_{PP}(\Omega)\, BW. \tag{2.70}$$

Putting this in Eq. 2.47 leads to a calibration factor β_{calib} for the measured signal amplitude

$$\int_0^\infty S_{PP}(\Omega)\, BW\, \mathrm{d}\Omega = \frac{k_\text{B}\, T}{m_{\text{eff},n}\, \Omega_n^2}\, BW\, \chi_{\text{zP}}^2\, g_\omega^2 \equiv \beta_{\text{calib}}. \tag{2.71}$$

$$\tag{2.72}$$

The optomechanical coupling g_ω deduced from this calibration reads

$$g_\omega = \sqrt{\frac{\beta_{\text{calib}}}{BW\, \chi_{\text{zP}}^2}\, \frac{\Omega_n^2\, m_{\text{eff},n}}{k_\text{B}\, T}}. \tag{2.73}$$

Equations 2.64, 2.65 and 2.73 show that g_0 is independent of a scaling of $m_{\text{eff},n} \mapsto \alpha\, m_{\text{eff},n}$. If $m_{\text{eff},n}$ is scaled by α, e.g. by different ways of calculating the overlap between the optical and mechanical mode functions, this scaling factor α will cancel out in g_0. In fact $m_{\text{eff},n}$ completely cancels out in g_0 since $g_\omega \propto \sqrt{m_{\text{eff},n}}$ and $z_{\text{zpf},n} \propto 1/\sqrt{m_{\text{eff},n}}$. Equations 2.64, 2.65 and 2.73 make clear that g_0 can be calculated directly from the integrated measured power spectrum (equation 2.71) under knowledge of the experimental settings contained in χ_{zP} (see equation 2.68)

$$g_0 = g_\omega\, z_{\text{zpf},n} \tag{2.74}$$

$$= \left(\frac{\beta_{\text{calib}}}{BW\, \chi_{\text{zP}}^2}\, \frac{\Omega_n^2\, m_{\text{eff},n}}{k_\text{B}\, T}\, \frac{\hbar}{2\, m_{\text{eff},n}\, \Omega_n} \right)^{\frac{1}{2}} = \left(\frac{\hbar\, \Omega_n}{2\, k_\text{B}\, T}\, \frac{\beta_{\text{calib}}}{BW\, \chi_{\text{zP}}^2} \right)^{\frac{1}{2}} \tag{2.75}$$

$$= \left(\frac{\hbar\, \Omega_n}{2\, k_\text{B}\, T\, BW\, \chi_{\text{zP}}^2} \int_0^\infty S_{PP}(\Omega)\, BW\, d\Omega \right)^{\frac{1}{2}}. \tag{2.76}$$

2.2 Optomechanical models

Dispersive and dissipative optomechanical couplings lead to energy transfer between optical and mechanical subsystems. The dynamical behavior of optomechanical systems is well understood and briefly described by the macroscopic model of the deformable

Fabry-Pérot cavity first, following the calculations of reference [Met08] for the limit of low finesse cavities. A consequent translation of this model to smaller mechanical objects leads to the proposal of reference [Fav08] where sub-wavelength sized objects are placed inside a miniature cavity. A model close to the experimental situation of the present work considering dispersive and dissipative optomechanical couplings is presented in reference [Bia11].

2.2.1 A common optomechanical model

The deformable Fabry-Pérot cavity represents a famous scheme of an optomechanical system. Here one mirror is fixed and the other one is attached to a spring of rigidity k as illustrated in figure 2.7. For a detailed description refer to reference [Met08].

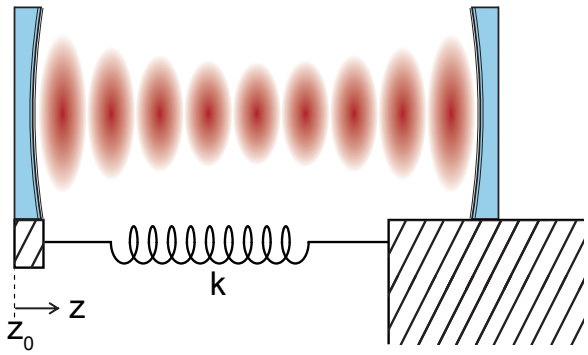

Figure 2.7: Deformable Fabry-Pérot cavity with one mirror fixed and the other attached to a spring.

The equation of motion for the moveable mirror is given by

$$m\,\ddot{z}(t) + m\,\gamma\,\dot{z}(t) + k\,z(t) = F_{th}(t) + F_{ph}(z(t)) \tag{2.77}$$

with the mirror mass m, mirror position z, viscous friction γ and driving forces of thermal F_{th} and optical F_{ph} origin. The term $|F_{th}|^2 = 4\,m\,\gamma\,k_B\,T\,\mathrm{d}\Omega/2\pi$ describes a statistical Langevin force that acts on the mirror as it is in contact to a thermal bath with temperature T. The light induced force is proportional to the intra cavity power and thus it depends on the mirror position $z(t)$. Further because of the decay rate of the cavity mode F_{ph} reacts retarded on fluctuations in $z(t)$. With the exponential retardation $h(t) = 1 - e^{-\frac{t}{\tau}}$ the light induced force can be expressed as $F_{\mathrm{ph}}(z(t)) = F(z_0) + \int_0^t \frac{\mathrm{d}F(z(t'))}{\mathrm{d}t'}\,h(t-t')\,\mathrm{d}t'$ where $\frac{\mathrm{d}F(z(t'))}{\mathrm{d}t'} = \nabla F\,\frac{\partial z(t')}{\partial t'}$ includes the force gradient $\nabla F = \frac{\partial F(z(t'))}{\partial z}$ which is assumed to be constant in linearized optomechanics since the deflections are small enough. Using Laplace transformation with $\hat{z}(\Omega) = \mathrm{LT}(z(t)) = \int_0^\infty z(t)\mathrm{e}^{-i\,\Omega\,t}\,\mathrm{d}t$ and $\hat{F}(\Omega) = \mathrm{LT}(F(t))$, equation 2.77 can be written

$$-\,m\,\Omega^2\,z(\Omega) + i\,\Omega\,m\,\gamma_{\mathrm{eff,ph}}\,z(\Omega) + k_{\mathrm{eff,ph}}\,z(\Omega) = F_{\mathrm{th}}(\Omega) \tag{2.78}$$

with effective damping, spring constant

$$\gamma_{\text{eff,ph}} \equiv \gamma \left(1 + Q \, \frac{\Omega_0 \, \tau}{1 + \Omega^2 \, \tau^2} \, \frac{\nabla F}{k} \right), \tag{2.79}$$

$$k_{\text{eff,ph}} \equiv k \left(1 - \frac{1}{1 + \Omega^2 \, \tau^2} \, \frac{\nabla F}{k} \right), \tag{2.80}$$

and resonance frequency $\Omega^2_{0,\text{eff,ph}} = k_{\text{eff,ph}}/m$. The mirror susceptibility now reads

$$\chi(\Omega) = \frac{1}{m} \, \frac{1}{\Omega^2_{0,\text{eff,ph}} - \Omega^2 + i \, \Omega \, \gamma_{\text{eff,ph}}}. \tag{2.81}$$

The maximum optomechanical effect e.g. in damping rate is reached for $\Omega_0 \, \tau \approx 1$ and $k_{\text{eff,ph}}(\Omega = 0) = 0$ and thus

$$\gamma_{\text{eff,ph,max}} = \gamma(1 + \frac{Q}{2}). \tag{2.82}$$

By inspection of equation 2.79 the following parameters are crucial to reach and boost this limit:

- a high finesse cavity with high τ provides high ∇F,
- a small mass m and small rigidity k enabled by small dimensioned mechanical resonator with high quality factor Q
- mechanical and optical time constants have to be chosen such that $\Omega_0 \, \tau \approx 1$.

With decreasing dimensions the mechanical resonator will reach the Abbe limit at some point and thus it can no longer form the mirror of a high finesse cavity. In the consecutive section a proposal is addressed where this instance is circumvented by separation of the optical and mechanical element.

2.2.2 Nano objects inside an optical cavity

A nano-optomechanical system as proposed in reference [Fav08] promises to overcome the limits of a deformable cavity. In the following this proposal with mechanical resonators smaller than the diffraction limits is briefly presented.
A pair of mirrors forms the cavity into which a mechanical resonator is introduced as depicted in figure 2.1. This way a high finesse cavity is combinable with a high quality factor mechanical resonator and the whole system can be scaled down to sizes compatible to optical fibers where the cavity mode diameter measures only some micrometers. The nanomechanical element is considered to interact with the optical field only weakly since its dimensions are much smaller than the wavelength λ. The interaction is expressed in terms of field transmittance $t_{\text{NR}} = \frac{1}{1+\Sigma}$ and reflectance $r_{\text{NR}} = \frac{-\Sigma}{1+\Sigma}$ where

$\Sigma = \Sigma_1 + i\,\Sigma_2 = \sigma/(2\,\epsilon_0\,c)$ relates to a plane of conductivity σ. This way the real part Σ_1 and the imaginary part Σ_2 account for optical dissipation and dispersion of the nanomechanical element. A scattering matrix (like equation 2.15 in chapter 2.1.1) formed from t_{NR} and r_{NR} is integrated in the product of matrices (at the place of $\mathbf{D}$ in equation 2.22) in order to describe the cavity with the nanomechanical element inside. The intensity transmission of the cavity with the nanomechanical element oscillating with amplitude z around an equilibrium position z_0 is deduced form the matrix product and yields

$$T(z_0, z) = \Big(\big(1 + \Sigma_1\,(1 + 2\,g\,\sin^2(k\,z_0)) + 2\,g\,\Sigma_1\,k\,z\,\sin(2\,k\,z_0)\big)^2 \tag{2.83}$$

$$+ \big(2\,g\,\Sigma_2\,k\,z\,\sin(k\,z_0)\big)^2 \Big)^{-1}, \tag{2.84}$$

where the assumption $z \ll \lambda$ is made and $g = \frac{2}{\pi}\,\mathcal{F} \approx \frac{2}{1-r^2}$ depends on the cavity finesse $\mathcal{F}$. The force acting on the resonator is derived from the imbalance of optical power distributed to the left and to the right of the nanomechanical element inside the cavity. For a high finesse cavity ($g = 2 \cdot 10^4$) the resulting cavity transmission, light induced force and respective gradients are plotted qualitatively versus z_0 in figure 2.8. Two cases are chosen to display, one (a) dominated by dispersion with $\Sigma_1 = 10^{-5}$ and $\Sigma_2 = 5 \cdot 10^{-4}$ and the other (b) dominated by dissipation with $\Sigma_1 = 5 \cdot 10^{-4}$ and $\Sigma_2 \approx 0$.

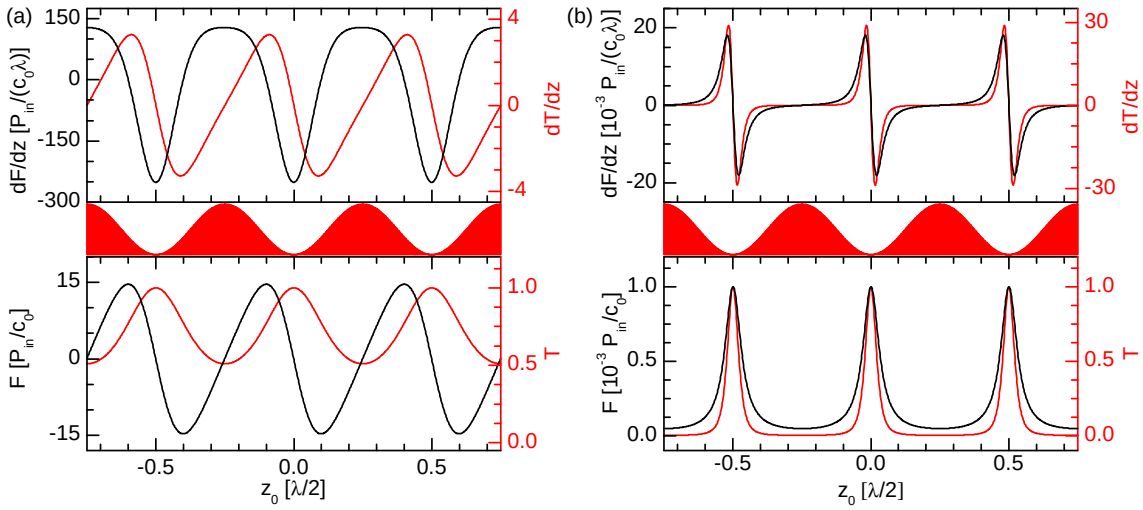

Figure 2.8: Plots of transmission, light-induced force and gradients with respect to the position z_0 of the nanomechanical element for (a) a dispersion dominated case with $\Sigma_1 (= 10^{-5} (< \Sigma_2 (= 5 \cdot 10^{-4})$ and (b) a dissipation dominated case with $\Sigma_1 (= 5 \cdot 10^{-4}) > \Sigma_2 (\approx 0)$. The red centered plot indicates the intensity distribution of the cavity mode. The cavity transmission T (gray) and the force (red) F_{ph} are plotted in the lower diagrams, the gradients $\mathrm{d}\,T/\mathrm{d}z_0$ (gray) and $\mathrm{d}\,F/\mathrm{d}z_0$ (red) are plotted in the upper diagrams (according to reference [Fav08]).

In the dispersion dominated case, where residual dissipation is still present, transmission is slightly modulated and exhibits the periodicity of the cavity mode intensity distribu-

tion. The light-induced force also reflects this periodicity and the extremal values of the force gradient do not coincide with the extremal values of transmission. In the dissipation dominated case the transmission and the light-induced force are peaked when the nanomechanical element coincides with a node of the cavity standing wave pattern. Gradients build-up only in the vicinity of these nodes. Comparing the values of the force gradients makes clear that in the dispersive regime the additional optomechanical damping (c.f. equation 2.79) can be manipulated in a much larger range to positive and negative values.
The force gradient strongly depends on the experimental setting and like Σ it is a value that is not easily accessible. However with decreasing size of the mechanical element only a perturbative character remains with very little dissipation and thus it is expected to approach the favorable dispersive regime.

2.2.3 Membrane with absorption in the middle of a cavity

A rather popular optomechanical system that has attracted the attention of several research groups [Wil09, Har08] is the 'membrane-in-the-middle' setup as it is originally introduced in reference [Tho08]. In this configuration a dielectric membrane is introduced inbetween the mirrors of a fixed Fabry-Pérot cavity. This membrane forms the mechanical part of the optomechanical system. The membrane extends over the full cross-section of the cavity mode and thus it is separated into two sub-cavities. The modes of the subcavities are coupled through the transmission of the membrane and the coupling is mediated by the membrane position. The 'membrane-in-the-middle' is very well illustrated by figure 2.1, too, when the mechanical resonator is thought as a dielectric membrane, which points out the similarity to the system studied in this work.
In the theoretical approach of reference [Bia11] a certain amount of absorption by the membrane is considered. This absorption causes optical loss leading to increased cavity dissipation and membrane heating. A brief sketch of that approach is presented in the following.

The quantum mechanical properties of the optomechanical system are described starting with the Hamiltonian

$$H = \frac{\hbar\,\Omega_n}{2}\,(\hat{p}+\hat{q}) + \hbar\,\omega_{\mathrm{c}}(\hat{q})\,\hat{a}^\dagger\,\hat{a} + i\,\hbar\,E\,(\hat{a}^\dagger\,\mathrm{e}^{i\,\omega_{\mathrm{l}}\,t} - \hat{a}\,\mathrm{e}^{-i\,\omega_{\mathrm{l}}\,t}). \tag{2.85}$$

A single mechanical membrane mode at frequency $\Omega_n/2\pi$ with dimensionless position $\hat{q}$ and momentum $\hat{p}$ operators interacts with a single cavity TEM_{00} mode at frequency $\omega_{\mathrm{c}}/2\pi$ with associated creation $\hat{a}^\dagger$ and annihilation $\hat{a}$ operators via radiation pressure. The empty cavity with frequency $\omega_0/2\pi$ and damping κ_0 experiences a frequency shift $\delta\omega_{\mathrm{c}}(z_0(\hat{q}))$ upon introduction of the membrane. Thus the cavity frequency reads $\omega_{\mathrm{c}}(\hat{q}) = \omega_0 + \delta\omega_{\mathrm{c}}(z_0(\hat{q}))$ and it depends on the membrane center of mass $z_0(\hat{q}) = z_0 + z_{\mathrm{zpf},n}\,\hat{q}$. The membrane position fluctuates around the mean value z_0, where $z_{\mathrm{zpf},n} = \sqrt{\hbar/(2\,m_{\mathrm{eff},n}\,\Omega_n)}$ denotes the zero point fluctuation of the n-th mechanical membrane mode with effective

mass $m_{\mathrm{eff},n}$. The cavity is pumped by a laser at frequency $\omega_\mathrm{l}/2\pi$ with intra cavity power P and $E = \sqrt{2\,P\,\kappa_0/(\hbar\,\omega_\mathrm{l})}$.
Membrane absorption comes into play by considering a non-zero imaginary part in $\delta\omega_\mathrm{c}(z_0(\hat{q}))$ which causes additional position dependent, non-linear cavity dissipation κ. The dynamics of the system are determined by the Hamiltonian in equation 2.85 and by fluctuation-dissipation processes of the optical and mechanical modes. Compared to purely dispersive coupling the additional cavity dissipation acts like an additional optical noise source that leads to modified scattering rates of photons into Stokes and anti-Stokes cavity sidebands. This influences the membrane position spectrum with modified effective angular resonance frequency

$$\Omega_{\mathrm{eff},n} = \Bigg(\Omega_n^2 + C\,\frac{\partial^2\omega_\mathrm{c}}{\partial z^2} - 2\,C\,\frac{\partial\omega_\mathrm{c}}{\partial z}\,\frac{\frac{\partial\omega_\mathrm{c}}{\partial z}\,\Delta\,(\kappa^2/4-\omega^2+\Delta^2)+\frac{\partial\kappa}{\partial z}\,\kappa/4\,(\kappa^2/4+\omega^2+\Delta^2)}{(\kappa^2/4+(\omega-\Delta)^2)(\kappa^2/4+(\omega+\Delta)^2)}\Bigg)^{\frac{1}{2}} \tag{2.86}$$

and damping

$$\gamma_{\mathrm{eff},n} = \gamma_n + C\,\frac{\partial\omega_\mathrm{c}}{\partial z}\,\frac{\frac{\partial\omega_\mathrm{c}}{\partial z}\,\Delta\,\kappa + 2\,\frac{\partial\kappa}{\partial z}\,(\kappa^2/4+\omega^2-\Delta^2)}{(\kappa^2/4+(\omega-\Delta)^2)(\kappa^2/4+(\omega+\Delta)^2)}, \tag{2.87}$$

where

$$C = \frac{4\,\Omega_n\,z_\mathrm{zpf}^2\,\kappa_0\,\mathcal{F}\,P_\mathrm{t,0}}{\pi\,\hbar\,\omega_\mathrm{l}(\kappa^2/4+\Delta^2)}. \tag{2.88}$$

$\Delta = \omega_\mathrm{l} - \omega_\mathrm{c}$ denotes the detuning of the drive laser from the cavity, and the resonant transmission $P_\mathrm{t,0} = \pi\,P/(4\,\mathcal{F})$ relates to P and the cavity finesse $\mathcal{F}$. Dispersive $\frac{1}{2\,\pi}\frac{\partial\omega_\mathrm{c}}{\partial z}$ and dissipative $\frac{1}{2\,\pi}\frac{\partial\kappa}{\partial z}$ optomechanical coupling appear explicitly in Equations 2.86 and 2.87 and thus relate to the optomechanically influenced shift in frequency and dissipation.

2.3 Summary

In summary the ingredients to describe the optomechanical system of a nanomechanical element inside a miniature cavity are formulated. Characteristics of the cavity like mode shape and dissipation are described by a ray transfer and field propagation formalisms. Elastic beam theory leads to expressions for the mode profile of the vibrating mechanical resonator and a formulation of the effective vibrational mass. Thermally driven Brownian motion provides a useful means for calibration of the motional amplitude. Coupling via dispersive and dissipative interaction of the optical mode with the mechanical element leads to the optomechanical system. Models for this system are presented starting from

the very common model of the deformable cavity where optical spring and damping are explained and transfered to a nanomechanical resonator in a rigid cavity which can be described analog to the popular ‘membrane-in-the-middle’ configuration. Calculations and formalisms are kept in a very applied fashion such that the presented collection of equations provide a handy toolbox for the experimental situations investigated in this work.

Chapter 3

Experimental setup

A high-finesse, fiber-based optical miniature cavity as for example used in reference [Ste06] is perfectly suited for the purpose of optomechanical experiments with nano-sized mechanical elements. It is a direct experimental approach to the proposal published in reference [Fav08]. The fabrication and assembly of such a cavity are anything but standard. These topics followed by the description of techniques used to characterize those cavities are addressed here. The optical laser setup to operate the cavity and measure samples and the vacuum setting with methods applied for acoustic vibration suppression are explained briefly.

3.1 Fiber optical micro cavity

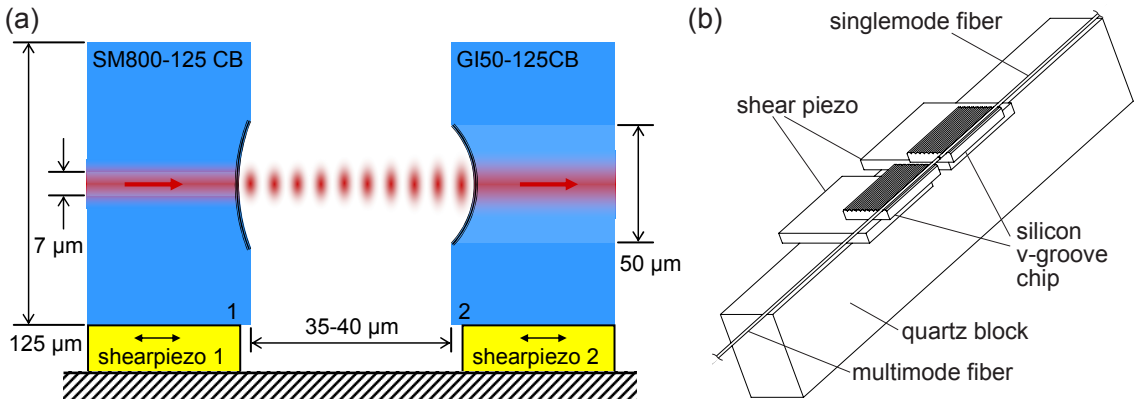

Figure 3.1: (a) Sketch of the cavity. (b) Schematic drawing of the assembled cavity.

The optical micro cavity is formed by two opposing fiber ends [Ste06, Hun10] as depicted schematically in figure 3.1(a). In order to form a high finesse cavity, the cleaved fiber ends are concavely shaped by laser ablation and coated with laser mirrors. The input fiber is a singlemode fiber for light at $800\,\mathrm{nm}$ (SM800-125CB, *Oxford Electronics*).

A multimode fiber with $50\,\mu\mathrm{m}$ core diameter (GI50-125CB, *Oxford Electronics*) is used for the rear mirror providing high collection efficiency in transmission. Fiber ends are permanently glued to shear piezo elements allowing for fine adjustment of the length of the cavity by some hundreds of nanometers. The other degrees of freedom (two translational and two rotational) have to be adjusted very precisely before the glue is cured. The assembly of the cavity as drawn in figure 3.1(b) is explained. Subsequently the cavity is characterized in terms of its finesse and optical mode geometry.

3.1.1 Assembly

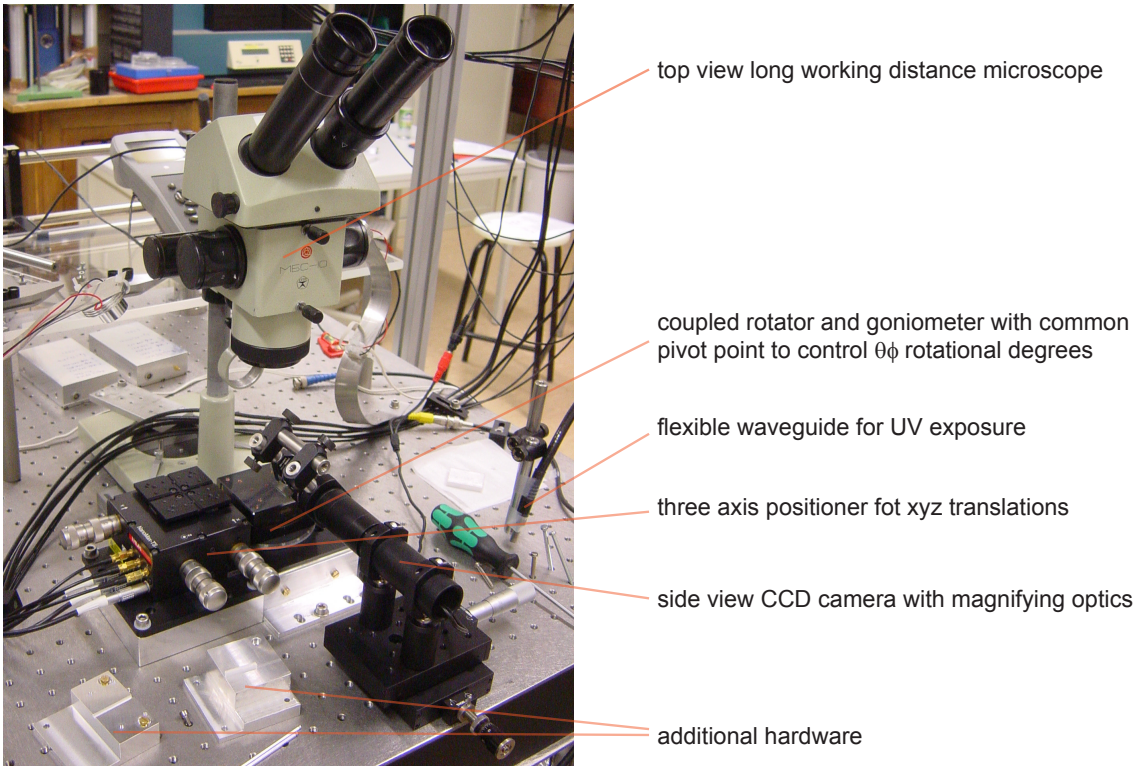

Figure 3.2: Cavity assembly workaround.

Fiber ends are processed with the fiber machining CO_2 laser setup of Jakob Reichel's group at the ENS in Paris [Hun10, Hun12]. Preprocessed fibers are sent to a coating company (*Advanced Thin Films*) to have a highly reflective coating of alternating dielectric layers deposited on the facets. Assembly of the cavities is described below. It is convenient to monitor the assembly from two orthogonal perspectives as depicted in figure 3.2. A long working distance microscope provides the top view and a CCD camera with magnifying optics the side view. A three axis linear positioner (NanoMax, *Thorlabs*), a rotator and a goniometer (*Owis*) enable control of all necessary degrees of freedom. The rotator and the goniometer share a common center of rotation where the alignment and assembly of the cavity takes place and thus the rotational degrees of freedom are decoupled

best from the translational ones. The UV-light (BlueWave 50, *Dymax*) to cure the glue (OP-4-20632, *Dymax*) is directed through a flexible waveguide at the desired location. Throughout this description all temporarily glued connections are cured for 5 s and all permanent ones for 60 s. Attention must be paid at the illumination of the work space. Avoid light sources of short wavelength like white light LEDs as they initiate curing of the used glue. Additional custom hardware adapters (sketched for illustration in appendix A.1) are mounted on the positioning stages at the different steps of assembly.

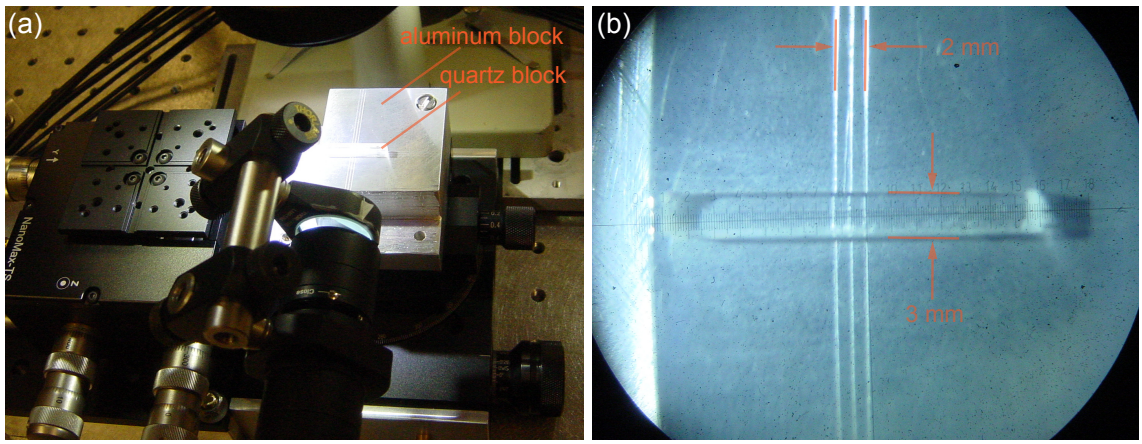

Figure 3.3: Preparation of the quartz block mount. (a) Overview and (b) as seen through the microscope.

A 3 mm × 4 mm × 25 mm quartz block forms a solid basis to mount the cavity on top. In a first step this block is aligned and fixed temporarily with super glue on an aluminum block (see figure 3.3).

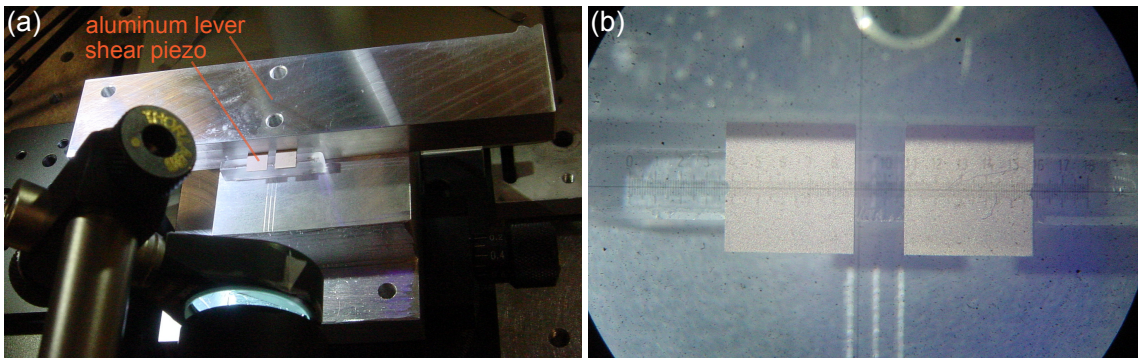

Figure 3.4: Alignment of the shear piezo elements. (a) Overview and (b) as seen through the microscope.

Shear piezo elements (5 mm × 5 mm × 0.5 mm, material PIC 255, *PiezoCeramics*) are aligned on the quartz block (see figure 3.4) and subsequently glued permanently. The aluminum lever serves as edge guide. Be aware of correct placement of the piezos (2 mm gap between them, equal extension on either side, all well centered on the quartz block, and the shear direction as marked by the groove must be parallel to the long extension of the quartz block).

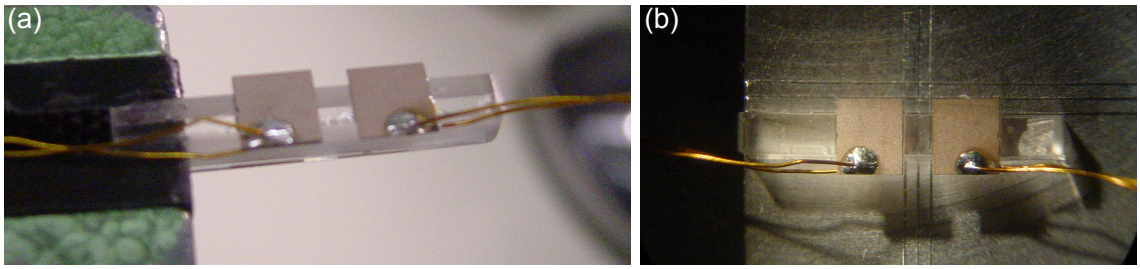

Figure 3.5: Wiring of the shear piezos. (a) Soldering the wires (b) and placing back of the quartz block under the microscope.

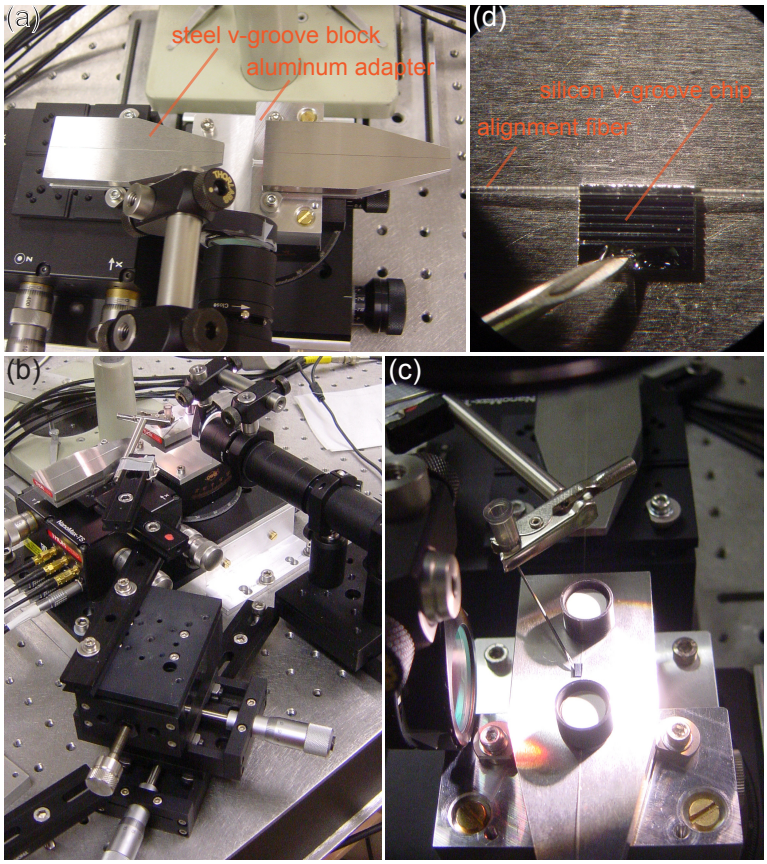

Figure 3.6: (a) Steel blocks with aligned top surfaces and v-grooves. (b) Installed xyz-manipulator with needle clamped at the end of its lever arm. (c) Close-up of the needle in contact with the aligned silicon v-groove chip and (d) stuck together as seen through the microscope.

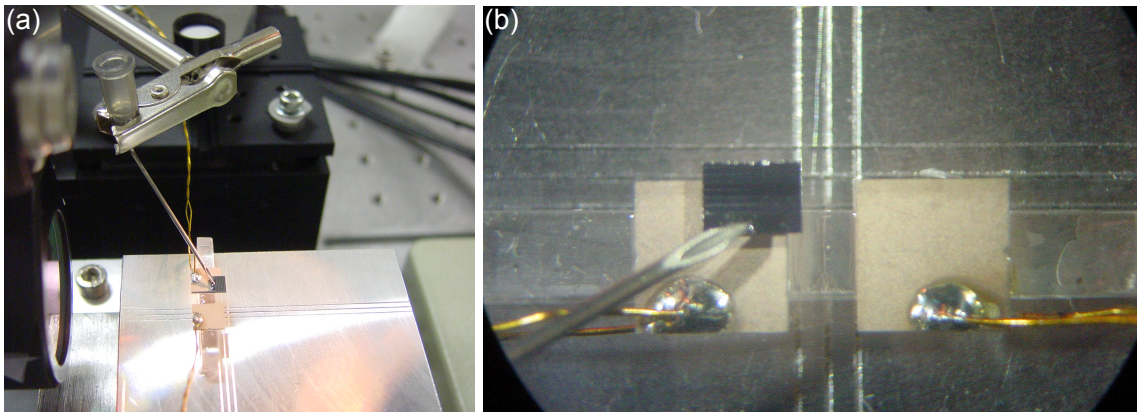

Figure 3.7: Placing and gluing of the first silicon v-groove chip on the shear piezo. (a) Overview and (b) as seen through the microscope.

For soldering wires to the electrodes of the shear piezos (figure 3.5(a)) it is more convenient to remove the quartz block from the aluminum block. Therefore use either a razor blade or dissolve the glue with a droplet of acetone. To decrease electrostatic interaction with the sample it is preferable to have the common ground connected to the top electrodes of both piezos. It is also advantageous to use flexible miniature coaxial cables instead of twisted pair wires. Put the quartz block back on the aluminum block aligned with the guiding groves as shown in figure 3.5(b) and fix it non-permanently with glue.

Remove the aluminum block with the glued quartz block. Mount the aluminum adapter on top of the goniometer and the two steel v-groove blocks as depicted in figure 3.6(a). The top surfaces of the steel v-groove blocks and the grooves themselves are aligned parallel. The angular positioning has to be kept fixed and must not be changed until mentioned. A further xyz-manipulator is installed and screwed on the breadboard (figure 3.6(b)). A needle is clamped to the extending lever arm of the manipulator and pointing at a silicon v-groove chip (figure 3.6(c)) that is placed onto the steel v-groove block right in the focus of the microscope. Grooves of the silicon chip are aligned parallel with the groove of the underlying steel block. Without disturbing this alignment the needle is brought into contact with the silicon chip and fixed temporarily with a small droplet of glue (figure 3.6(d)). The position of the manipulator on the table must not be shifted as long as the silicon chip is attached to the needle.

Replace the aluminum block with the steel v-groove by the aluminum block with the adhered quartz block (figure 3.7(a)). Place the silicon v-groove chip on the left piezo extending its right and upper edges by half a millimeter as shown in figure 3.7(b) and glue it permanently. The glue has to cover the whole contact area and form a slight meniscus at the side faces of the chip. Curing the glue under the chip might be affected by shadowing. In order to avoid this illumination under a small angle is advantageous. Thus UV light enters the glue filled gap between piezo and silicon chip and the curing result is enhanced.

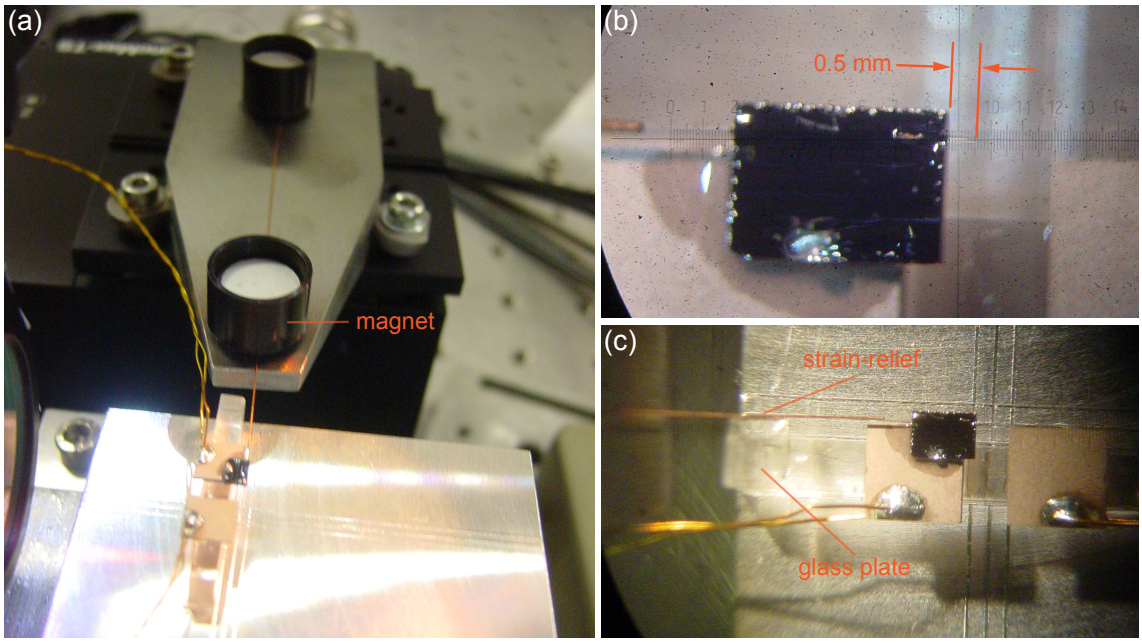

Figure 3.8: Gluing the first fiber. (a) Fiber to v-groove alignment. (b) Fiber end extends v-groove chip by half a millimeter. (c) Fiber glued to v-groove chip and stain-relief.

The first fiber, the singlemode fiber, is magnetically mounted in the groove of the steel block on top of the xyz-positioner and approached to the silicon chip (figure 3.8(a)). The mirror ended fiber has to extend the v-groove of the silicon chip by 0.5 to $0.7\,\mathrm{mm}$ (figure 3.8(b)). Bed the fiber in a droplet of glue and make sure that no air is under the fiber and the fiber is covered with glue. Cure the glue for $60\,s$. Place a small glass plate on the quartz block at its left end such that it gently touches the coated fiber and fix it there permanently. Glue the fiber and the piezo wire to either side of this glass plate securely since this will serve as mechanical strain-relief (figure 3.8(c)).

Carefully remove the aluminum block with quartz block, the first mounted fiber and the steel v-groove block. Mount the aluminum lever arm on the xyz-positioner and the steel v-groove block on top of the goniometer with respective aluminum adapters (figure 3.9(a)). Put the second silicon v-groove chip onto the steel v-groove block with their grooves aligned (figure 3.9(b)). A tenth of a millimeter of material is ground off the bottom side of this very piece of silicon v-groove chip, that will allow more tolerance for alignment of the cavity in its angular and vertical degrees later. Adhere the silicon chip temporarily to the aluminum lever arm with two tiny spots of glue on either bumpy protrusion at the side of the arm. This connection must be weak enough to cleave it after the cavity is fully assembled. Not changing the angles of the rotator and goniometer till now has secured that the alignment of the v-groove chip and its grooves fit to that of the first one already mounted on the piezo.

Pull-back the steel v-groove block by one centimeter to the right and mount the second fiber, the multimode fiber, in a way that it protrudes the left edge by circa one centimeter

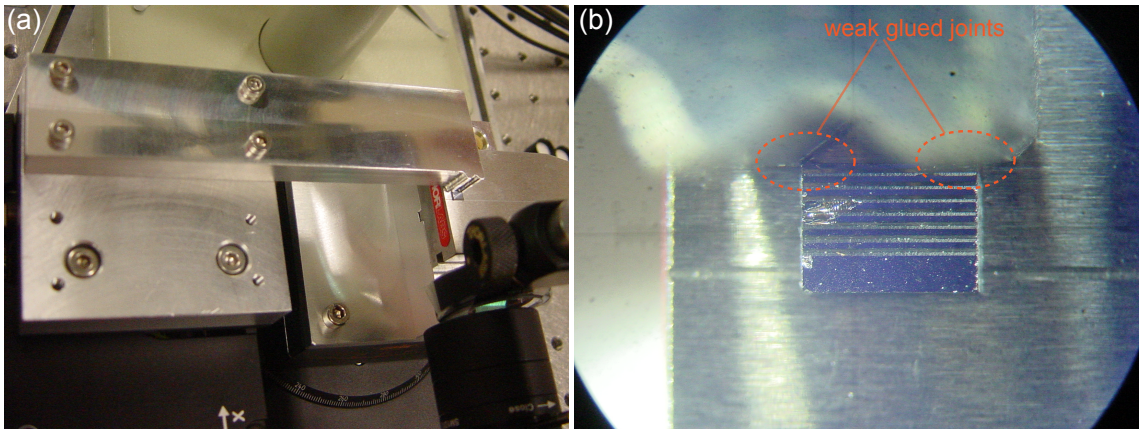

Figure 3.9: Aluminum lever arm with second silicon v-groove chip adhered. (a) Overview and (b) as seen through the microscope.

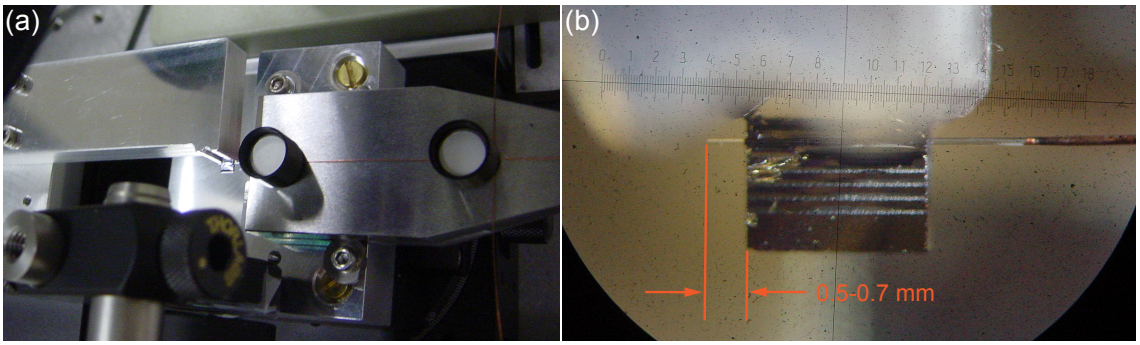

Figure 3.10: Fixing the second fiber. (a) Fiber to v-groove alignment. (b) Fiber end extends v-groove chip by half a millimeter.

(figure 3.10(a)). Align the free end of the fiber with the groove of the silicon chip that is suspended at the aluminum lever arm. Goniometer and rotator might be used now. The mirror ended fiber has to extend the v-groove of the silicon chip by 0.5 to $0.7\,\mathrm{mm}$ to the left (figure 3.10(b)). Bed the fiber in a droplet of glue and make sure that no air is under the fiber and the fiber is covered with glue. Cure the glue for $60\,s$.

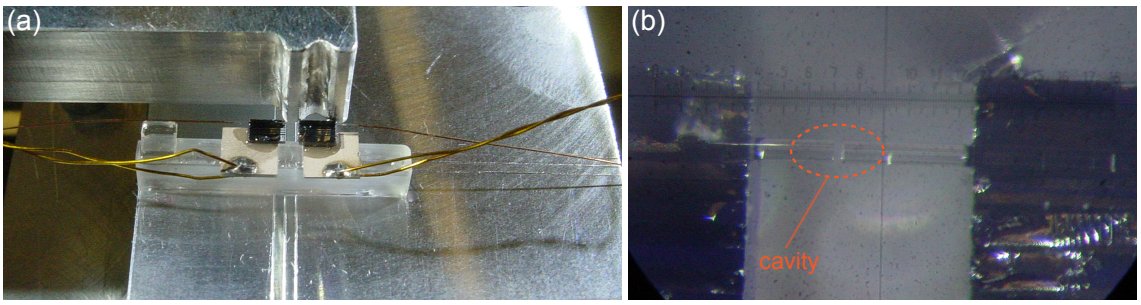

Figure 3.11: Cavity alignment and gluing. (a) Overview and (b) as seen through the microscope.

The aluminum adapter with steel v-groove block on the goniometer is replaced by the aluminum block with the adhered quartz block (figure 3.11(a)). Now the alignment procedure of the cavity starts. The goal is to have a cavity of about $30\,\mu\mathrm{m}$ length with well defined optical modes. Throughout this procedure the cavity is periodically scanned to monitor the cavity reflection and transmission spectra. Therefore connect the fibers and the left piezo to a suitable setup (use e.g. the setup described in section 3.2). It is advantageous to start the alignment with a very short cavity. Adjust one rotational degree first and compensate with the proper transversal axis for translational mismatch. Higher order modes in the cavity spectrum have to be suppressed and resonances in transmission or reflection are maximized. Proceed with the other pair of angular and transversal axes. Increase the cavity length and readjust the rotational and translational degrees. Repeat these adjustment and expansion procedures to iteratively approach the aimed cavity length. Fill the gap between the silicon v-groove chip and the piezo on the right with slow curing glue (301, *EPO-TEK*). While hardening compensate for the shrinking of the glue in order to keep the cavity well aligned.

Final alignment of the cavity is depicted in (figure 3.12(a) and (b)) seen from orthogonal views. The alignment procedure, that optimizes the fundamental mode of the cavity, together with geometrical imperfections of the fiber ends may result in the visual axial mismatch of the fibers. The aluminum lever arm is disconnected from the right silicon chip by cleaving the glue joints. To weaken the link the glue spots are perforated with a needle before the lever arm is moved to brake the connection. Strain-relief for fiber and piezo wire is installed on the right end of the quartz block as before. Transfer the quartz block with the cavity from the aluminum block to the final mount for integration into the experimental setup.

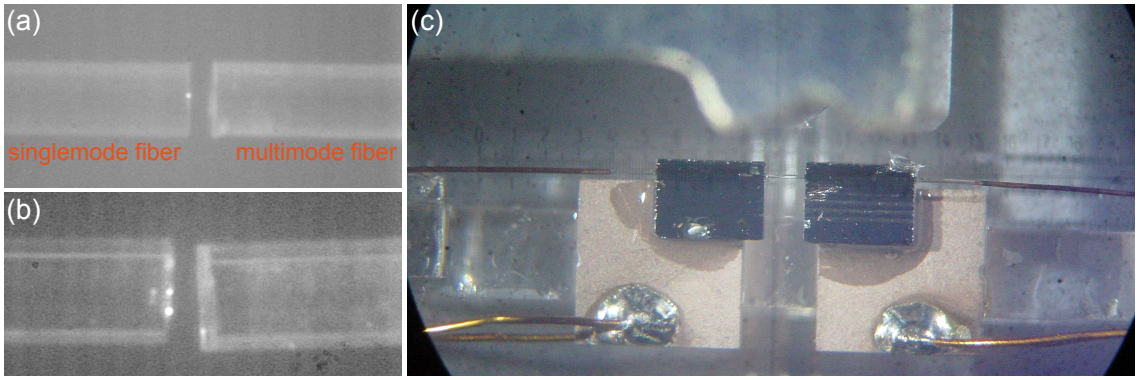

Figure 3.12: Final cavity alignment (a) and (b) seen from orthogonal views. (c) Cavity unfixed from the aluminum lever arm removed

3.1.2 Characterization

For the investigations of the interaction of light with mechanical elements inside the cavity some of its characteristics are important to know. These are the cavity finesse and the geometry of the optical mode. Both are experimentally accessible through measurements of the free spectral range and the cavity linewidth or damping rate. The typical setup to measure these values is illustrated in figure 3.13.

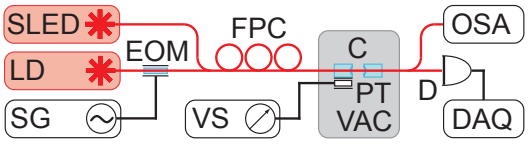

Figure 3.13: Setup to measure the free spectral range and the linewidth of the cavity. Symbols are described in the text.

In order to measure the free spectral range a super luminescent light emitting diode (SLED, EXS7505-8411, *Exalos*) with $750\,\mathrm{nm}$ center wavelength and $20\,\mathrm{nm}$ bandwidth illuminates the cavity (C). The transmitted light is sent to an optical spectrometer (OSA), which consists of a Czerny-Turner-monochromator (HR 320, *Horiba Jobin Yvon*) combined with a liquid nitrogen cooled CCD-camera (LN/CCD1024 E/1, *Princeton Instruments*).
For the measurement of the cavity linewidth laser light from a stabilized diode laser (LD, see below 3.2.1) is injected into the cavity. The cavity length is scanned across a resonance by sweeping the voltage of the variable voltage source (VS) that is applied to the shear piezo element (PT). The transmission signal is acquired with a photo detector (D) and monitored on an oscilloscope (DAQ). For calibration purpose the laser light is modulated by the electro optical phase modulator (EOM, NIR-MPX800-LN-10, *Photline*) fed with an electrical RF-signal ($17\,\mathrm{dBm}$ at $1\,\mathrm{GHz}$) provided by the signal generator (SG). Fiber polarization control (FPC) allows selecting one distinct cavity polarization. The cavity is operated in vacuum (VAC) at $10^{-5}\,\mathrm{mbar}$.

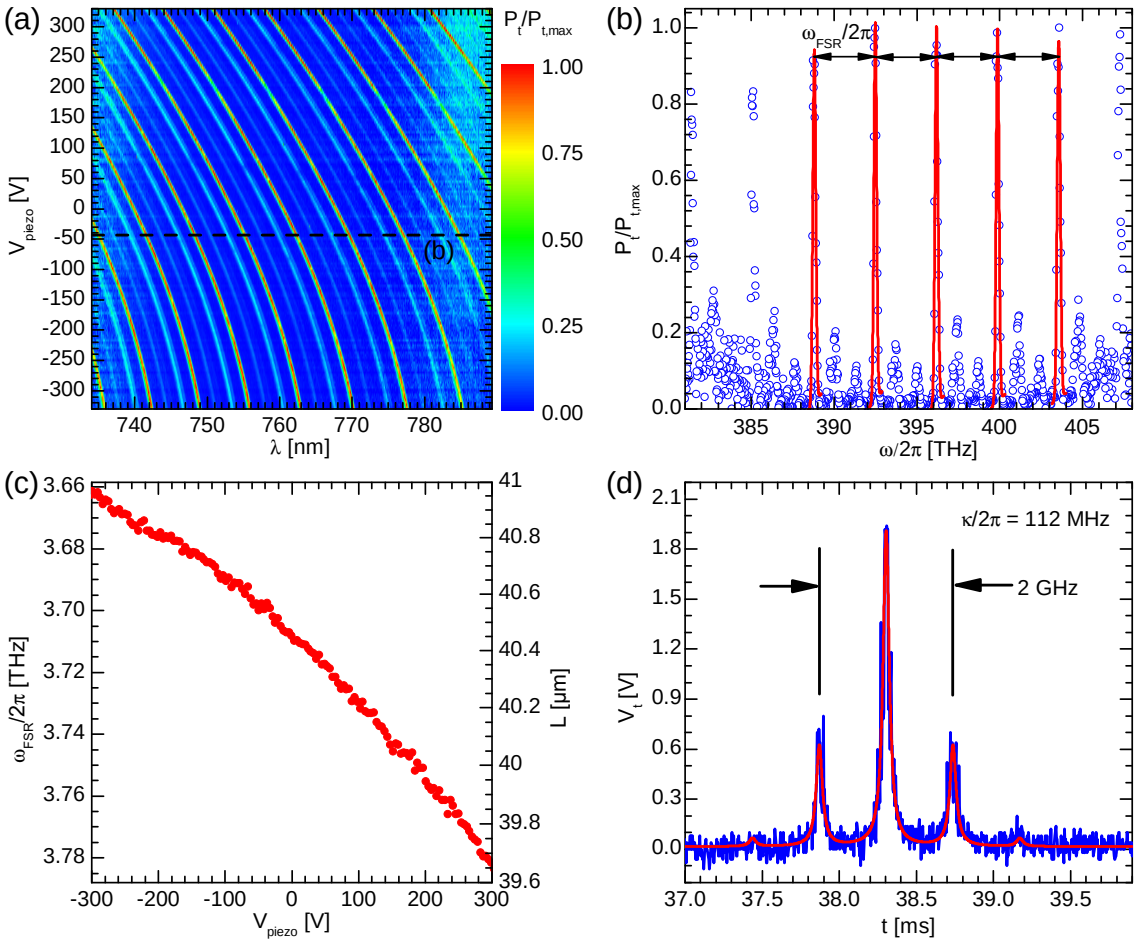

Figure 3.14: (a) Cavity transmission spectra measured with the SLED and varying cavity length set by V_{piezo}. The spectrum marked by the dashed line is plotted in (b) with its wavelength axis transformed into frequency units. Gaussian fits (red curves) to the data points (blue open circles) yield the spacing of the main resonances and thus the FSR of the cavity $\omega_{\text{FSR}}/2\pi$. (c) Values of the FSR and linked effective cavity length L are plotted against the cavity piezo voltage V_{piezo}. (d) Photo detector voltage of the cavity transmission versus scan time measured during a scan across a cavity resonance with modulated laser. Sidebands are visible on either side of the main resonance. The known side band spacing allows for calibration of the horizontal axis in frequency units. A multiple airy fit (red) of equation 3.2 to the data trace (blue) yields the cavity linewidth $\kappa/2\pi$ of 112 MHz.

Cavity transmission spectra measured with the SLED for varying cavity length set by V_{piezo} are shown in the color plot of figure 3.14(a). Up to eight longitudinal cavity modes (red bent lines) are observed in the measured wavelength range. In between of these two higher order resonances occur (light blue bent curves). The spectrum marked by the dashed line is plotted in figure 3.14(b) with its wavelength axis transformed into frequency units. Gaussian fits (red curves) to the data points (blue open circles) yield the positions of the main resonances and their spacing is the free spectral range (FSR) of the cavity $\omega_{\text{FSR}}/2\pi$. The effective cavity length L, that includes the part of the optical mode penetrating the dielectric layer stack of the mirrors, is inversely proportional to $\omega_{\text{FSR}}/2\pi$ by

$$L = \frac{\pi\, c}{\omega_{\text{FSR}}} \tag{3.1}$$

with the vacuum speed of light c. Values of the FSR and linked effective cavity length L are plotted against the cavity piezo voltage V_{piezo} in figure 3.14(c). At $V_{\text{piezo}} = 0\,\text{V}$ the free spectral range is $3.70\,\text{THz} \pm 1\,\%$ and thus the effective cavity length is $40.4\,\mu m$.

A highly resolved scan across a cavity resonance measured with a modulated laser is presented in figure 3.14(d). Sidebands are visible on either side of the main resonance with their spacing given by the modulation frequency $\Omega_{\text{mod}}/2\pi$. A multiple airy fit (red) to the data trace (blue) along with the known side band spacing allows for calibration of the horizontal axis in frequency units and yields the cavity linewidth $\kappa/2\pi = \omega_{\text{FWHM}}/2\pi$ of $112\,\text{MHz}$. The multiple airy fit function reads

$$T(\omega) + a_1\, T(\omega - \Omega_{\text{mod}}) + a_1\, T(\omega + \Omega_{\text{mod}}) + a_2\, T(\omega - 2\,\Omega_{\text{mod}}) + a_2\, T(\omega + 2\,\Omega_{\text{mod}}) \tag{3.2}$$

where a_1 and a_2 are amplitude coefficients and T is the expression of equation 2.18 for the transmission of a single cavity resonance

$$T(\omega) = \frac{T_{\text{max}}}{1 + (\frac{2\mathcal{F}}{\pi})^2\, \sin^2(\frac{\pi\,\omega}{\omega_{\text{FSR}}})} \tag{3.3}$$

with peak transmission T_{max}. The cavity finesse $\mathcal{F}$ is given by the ratio of the free spectral range and the linewidth

$$\mathcal{F} = \frac{\omega_{\text{FSR}}}{\kappa} \tag{3.4}$$

which has a value of $33 \cdot 10^3 \pm 5\,\%$ at $V_{\text{piezo}} = 0\,\text{V}$. The errors originate from the statistics of the respective fits.

A standard formalism applying ray propagation transfer matrices allows to calculate optical mode parameters in cavities or laser resonators from geometric boundary conditions (refer to chapter 2.1.1 or see text books about optics e.g. reference [Sal91]). This is used to estimate the diameter of the optical mode from the cavity length $L = 40.4\,\mu m$

and mirror radii of curvature that are $91\,\mu\mathrm{m}$ for the singlemode fiber and $120 \pm 40\,\mu\mathrm{m}$ for the multimode fiber. Thus the mode waist radius is approximately $3.1 \pm 0.1\,\mu\mathrm{m}$ and the diameter of the mode reaches up to $8.8\,\mu\mathrm{m}$ at the surfaces of the mirrors.

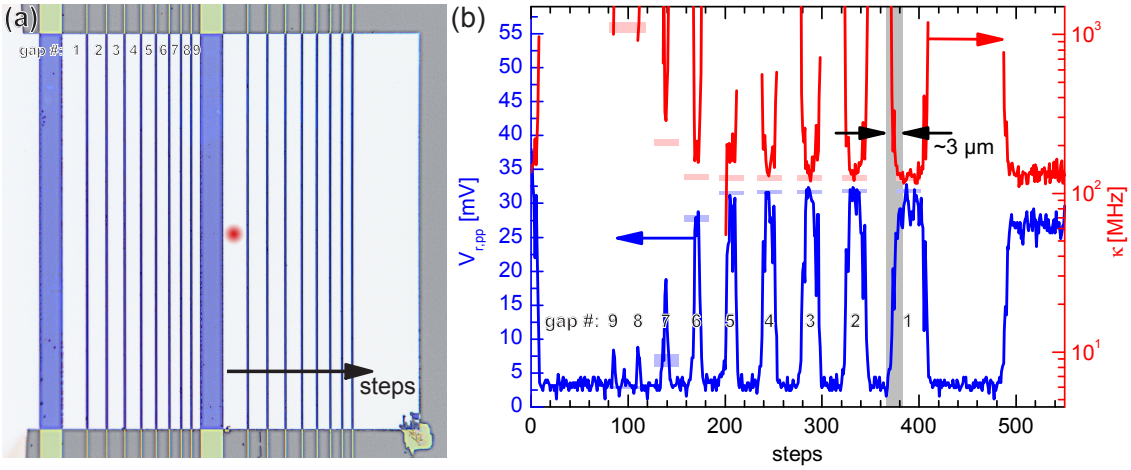

Figure 3.15: Measurement of the cavity mode diameter. (a) A test sample consists of a freely suspended line grid (blue) with gaps (light gray) of varying widths (given in table 3.1). The sample is stepped through the cavity mode (central red spot) effectively moving the spot through the grid defined by gaps #9 to #1 and at each step a cavity resonance scan is recorded. (b) Cavity resonant transmission $V_{\mathrm{r,pp}}$ and linewidth $\kappa/2\pi$ are plotted in blue and red, respectively. Increases in transmission and decreases in cavity damping rate result from traversing gaps. Thus these features in these traces can be assigned to the gaps as labeled.

Table 3.1: Gaps and widths of the test structure shown in figure 3.15a.

gap number		1	2	3	4	5	6	7	8	9
gap width	$[\mu\mathrm{m}]$	28.0	22.4	20.8	18.6	16.6	14.6	12.8	10.7	10.1
linewidth	$[\mathrm{MHz}]$	115	119	119	128	156	156	286	918	1003

The clear aperture describes the smallest diameter of an aperture that can be introduced into the cavity without creating too much extra loss. This value is of course larger than the mode waist diameter of high finesse cavities. However the clear aperture is a crucial design parameter to know when dissipative objects are introduced into the cavity. With a clipping model that adds the extra optical loss induced by the structure (this is the portion of the optical mode overlapping with the structure) to the cavity round trip loss analog to the formalism presented in reference [Sal91] the dependence of transmission and linewidth on geometrical configurations can be derived. The clear width for a slit aperture inside the cavity is thus estimated from the geometry of the mode and intrinsic cavity damping. For $10\,\%$ incease in linewidth the slit can be as narrow as $14\,\mu\mathrm{m}$.

The clear width for a slit aperture is measured by introducing a test sample with gaps of different widths into the cavity. The test structure is formed by a series of parallel, freely suspended beams made of silicon nitride with varying distance from each other.

The beams are $2\,\mu\mathrm{m}$ or $30\,\mu\mathrm{m}$ wide and widths of the gaps are listed in table 3.1 and. The fabrication of such a structure is explained later in chapter 5.1. Figure 3.15(a) displays the test structure, where the supporting silicon frame is gray, the suspended parts of the beams are blue, gaps are light gray and the cavity mode is illustrated by the diffuse red spot.

The starting position (zero steps) of the test sample relative to the cavity mode (red dot) is illustrated in figure 3.15(a). Since there is no overlap between the structure and the cavity mode, the resonant cavity transmission is maximal and the cavity linewidth is minimal (see figure 3.15(b) where photo detector voltage $V_{\mathrm{r,pp}}$ and linewidth $\kappa/2\pi$ are plotted as blue and red traces, respectively). Stepping of the sample to the right, as indicated by the black arrow in figure 3.15(a), drives the thick blue beam into the stationary cavity mode. This causes extra cavity damping, the linewidth increases and the transmission drops until the extra optical loss is too strong to support a cavity mode and practically no light is transmitted ($V_{\mathrm{r,pp}} < 5\,\mathrm{mV}$). When the next gap (number 9) approaches the mode center the cavity signal reappears. The signal recovers to the values of the undisturbed cavity with increasing gap widths. Gap number 3 has a width of $20\,\mu\mathrm{m}$ and provides the fully recovered, empty cavity mode with lowest dissipation values and highest transmission values reached.

In principle the measured values reflect the model values for transmission and linewidth quite well. They are displayed for the respective gaps as light blue and light red bars in figure 3.15(b). An increase in linewidth of $10\,\%$ occures at gap widths between $18.6\,\mu\mathrm{m}$ and $16.6\,\mu\mathrm{m}$. This is a littel bit larger than predicted by the model but well within the tolerance range given by the input parameters of the calculations.
This result gives design guidelines for doubly clamped mechanical elements implicating a spacing of the clamps of at least $15\,\mu\mathrm{m}$ in order to not degrade the cavity mode too strongly. For measurements of dissipative elements, the gray shaded region in figure 3.15(b) marks the range of about $3\,\mu\mathrm{m}$ where the dissipative interaction facilitates the detection of mechanical displacements.

3.2 Optical setup and stabilization

The setup used for operating the cavity and sample for optomechanical measurements comprises optical and electrical subsystems. The optical part with light sources, beam guiding elements and detectors is built to form the interaction between the sample and the optical cavity field and to translate the information about the interaction to detectors. The detectors transform the optical signals into electrical signals to be analyzed and processed further for experiment controlling purposes. These topics are detailed in the following and in reference [Sta10]. A sketch of the setup is given in figure 3.16 along with a brief description in the caption. List of components used in the setup are given in appendix A.2.

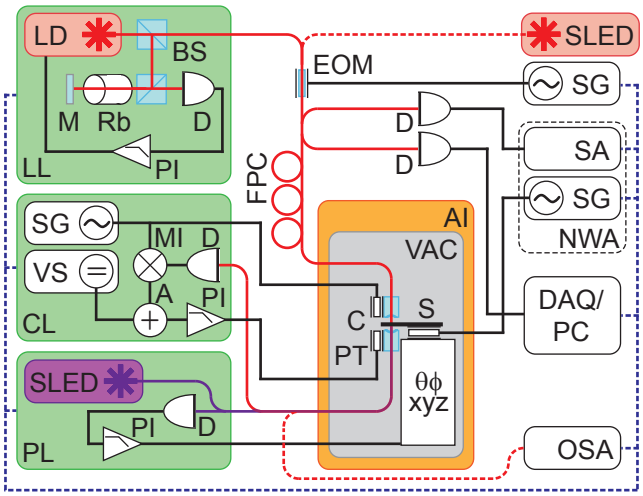

Figure 3.16: Sketch of the measurement setup. Usual operation (solid red line in the optical path): A diode laser (LD) stabilized on an atomic resonance of rubidium (Rb) is launched to the cavity (C). On its way the light passes two faraday isolators (not shown) an electro-optic modulator (EOM) driven by a RF-signal generator (SG) and a fiber beam splitter, where half of the beam is split off for intensity monitoring on a detector (D). The other portion propagates further along the fiber through a polarization control device (FPC) to match the cavity polarization and the fiber is feed-through acoustic shielding (AI) and into the vacuum chamber (VAC) where the cavity is situated. The cavity reflection signal propagates all the way back through the fiber beam splitter and ends up in the other detector (D) that is connected to either a spectrum or a network analyzer (SA, NWA) to measure the RF-spectrum of the cavity light. The cavity transmission is sent to a photo detector (D) that is connected to an electronic feed back loop (CL) stabilizing the cavity length through shear piezo elements (PT). Light from a super luminescent diode (SLED, violet) is injected through the second fiber to the cavity. The interference between the rear mirror and the sample (S) is used for position and deflection detection and to stabilize the sample z-position (PL). A signal generator (SG, either stand alone device or the output of the NWA) provides the electrical source to optionally drive vibrations of the sample via the piezo element underneath the sample. Alternative operation (dashed red line in the optical path): To measure the cavity free spectral range a super luminescent diode (red) illuminates the cavity and the transmission spectrum is measured with a spectrometer (OSA) as described earlier in chapter 3.1.2. For measurement control and data acquisition protocols are implemented on a computer with respective hardware interfaces (DAQ/PC).

3.2.1 Stabilized diode laser

A home built external cavity diode laser (LD) with typical linewidth of some hundreds of kilohertz [Ric95] serves as laser source for the experiment. The temperature and current of the laser diode are regulated by a commercial controller (DCC 110, *Toptica*, not shown) on a slow timescale. The stabilization of the laser (LL, green box in figure 3.16) consists of grating position and diode current control by locking the laser frequency on a reference, an atomic transition of rubidium. To this end a part of the laser beam exiting the laser is branched off at a glass plate (BS), sent through a rubidium gas cell (Rb) and retro-reflected at the mirror (M) to perform a Doppler-free absorption spectroscopy of the rubidium atoms at the detector (D) (details of such spectroscopy are not explained here but can be found in text books, e.g. in reference [Dem07]). The consecutive servo electronics (PI), a proportional integral feedback loop (Lock Box 5 borrowed from the group of Theodor Hänsch), settles the laser frequency on the desired position in the rubidium spectrum (here the $5\mathrm{S}_{1/2}, \mathrm{F} = 2$ to $5\mathrm{P}_{3/2}, \mathrm{F} = 2\,\mathrm{co}\,3$ crossover transition of ^{87}Rb is used). Slow thermal drifts are compensated by acting on the position of the diffraction grating of the external cavity laser, whereas high frequency disturbances are counteracted through the laser current. More details on the laser stabilization and associated electronic circuitry can be found in reference [Sta10]. It has to be mentioned that the knowhow about stabilized diode lasers together with electronic components is borrowed and adapted from the group of Theodor Hänsch.

3.2.2 Cavity stabilization

The fiber-based cavity is stabilized on the laser wavelength either by a modified 'Pound-Drever-Hall' locking scheme [Bla01] in order to lock the cavity in the vicinity of its resonance or by a 'side-of-fringe' locking scheme to lock the cavity along the slopes beside the peak. For cavity locking the functional components grouped in the green box labeled by CL in figure 3.16 are used.

For the 'Pound-Drever-Hall' scheme a lock-in amplifier (7265, *EG&G*, it comprises the signal generator SG, the mixer M and the voltage source VS) modulates the cavity length by applying a $92\,\mathrm{kHz}$ ac voltage to the first shear piezo (PT) acting on the front mirror of the cavity (C) at the singlemode fiber. The optical signal transmitted through the cavity is sent to a detector (D) and then demodulated by the lock-in. Hence the resulting error signal V_{err} (c.f. figure 3.17) has a zero point at the resonance of the cavity. A servo loop (PI) locks on this zero point by controlling the cavity length through the second shear piezo (PT) at the rear mirror. The cavity is consequently kept on resonance. By adding the dc voltage V_{add} of the programmable voltage source VS through the active adder electronics (A) to the error signal, the reference point of the feed back loop is shifted and thus the cavity is stabilized at a defined detuning. This works in the range around the cavity resonance where the error signal is monotonically increasing. Figure 3.17(a) illustrates the error signal with added offset. All traces exhibit the error signals that originate from scan-

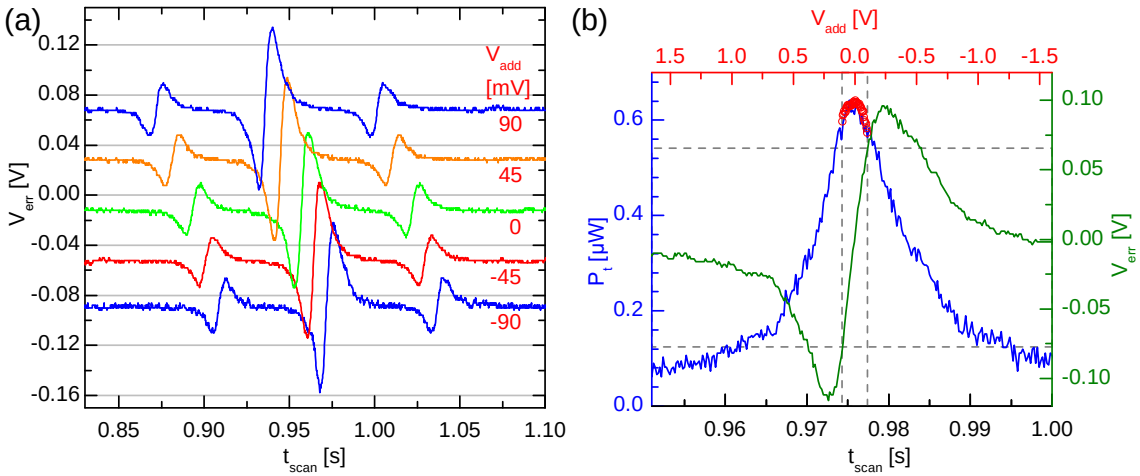

Figure 3.17: Cavity lock signals. (a) Error signal V_{err} from cavity transmission scans with different added offset voltages V_{add} in order to vary the locked cavity detuning. Blue traces have no zero and cannot be used for cavity locking. (b) Cavity transmission P_{t} (blue) and error signal V_{err} (green) during cavity scan. Red open circles denote transmission values of a locked cavity with applied V_{add} in the displayed range.

ning the cavity across the laser carrier and sidebands (see chapter 3.1.2). Blue traces are out of reach for the stabilization feedback loop, since they have no zero. Figure 3.17(b) illustrates the range of operation where the cavity lock works. Blue and green traces are the cavity transmission P_{t} and the error signal V_{err} during a cavity scan, where red circles denote the transmission values of the locked cavity with applied offset voltage V_{add}.
The 'side-of-fringe' method requires less electronics, especially the modulation of the cavity length and the demodulated signal of the lock-in amplifier are not needed. Instead the cavity transmission signal (with added offset) serves directly as error signal. It is fed into the feedback electronics, that stabilizes the cavity length around a zero of the error signal.
More details on the cavity stabilization and associated electronic circuitry can be found in reference [Sta10].

3.2.3 Interferometric setup

A built-in interferometer provides another access to the sample inside the cavity (violet path in figure 3.16). A superluminescent light emitting diode (SLED, S5FC1018S, *Thorlabs*) launches light through the multimode fiber into the cavity. At the center wavelength $\lambda_0 = 1310\,\mathrm{nm}$ of the SLED the mirror coatings are no longer highly reflective such that only a cavity with very low finesse is formed. The large spectral bandwidth $\lambda_{\mathrm{FWHM}} = 45\,\mathrm{nm}$ of the SLED provides a coherence length L_{coh} of $12\,\mu\mathrm{m}$ according to the bandwidth coherence length relation

$$L_{\mathrm{coh}} = \frac{\lambda_0^2}{\pi\,\lambda_{\mathrm{FWHM}}}. \tag{3.5}$$

Thus, on one hand L_{coh} is large enough that reflections from the sample structure and close-by cavity mirrors lead to an interference signal on the detector (D). The dc component of that signal can be used for drift compensation, whereas the ac component carries information about the vibration of the mechanics. On the other hand L_{coh} is low enough that parasitic interference in the multimode fiber from distant reflections at connectors or fiber splices are suppressed. In order to minimize drift of the interference signal itself it is crucial to mechanically fix and thermally anchor the fiber to the optical breadboard. Thus coupling of multiple fiber modes by thermal and mechanical stress stays constant on a longer timescale of a few hours.
Since no high finesse cavity is formed the interferometer provides a mean to measure the displacement of the mechanical element inside the cavity independent of optomechanical effects. This way a rather convenient method for in-situ reference measurements of the mechanical characteristics of the sample is established.

3.3 Vacuum setup and vibration isolation

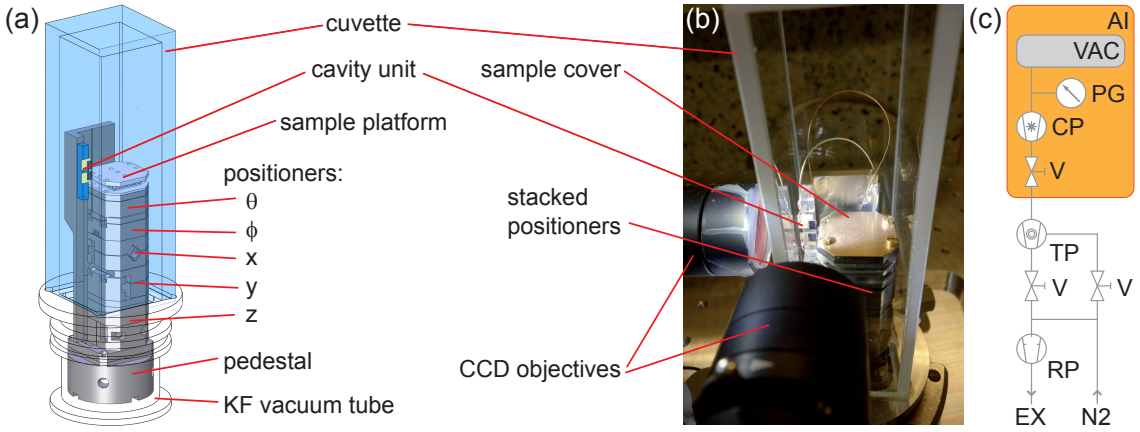

Figure 3.18: Sketch (a) and photograph (b) of the vacuum glass cuvette with cavity, positioning unit and sample. (c) Sketch of the vacuum setup. Symbols are acoustic isolation (AI), vacuum chamber (VAC), pressure gauge (PG), cryogenic pump (CP), valve (V), turbo pump (TP), rotary pump (RP), exhaust (EX), nitrogen purge line (N2).

Mechanical constructions form a solid framework to support the experimental devices, where vibration suppression and vacuum handling are major issues. The vacuum chamber consists of a glass cell and standard metal vacuum tubing. Pressure gauges, the pumping line, feedthroughs for electrical wires and optical fibers and a solid mount for the cavity and the sample positioning unit (ANP100, *attocube*) are mounted on this vacuum system. Cavity and positioning units are covered by the glass cell (700.036-OG, *HELLMA*) to enable visual access for two CCD cameras from orthogonal views. Rapid sample cycling is facilitated by connecting the glass cell with only one KF 40 quick flange to the residual vacuum chamber. Figure 3.18(a) and (b) present labeled drawing and pho-

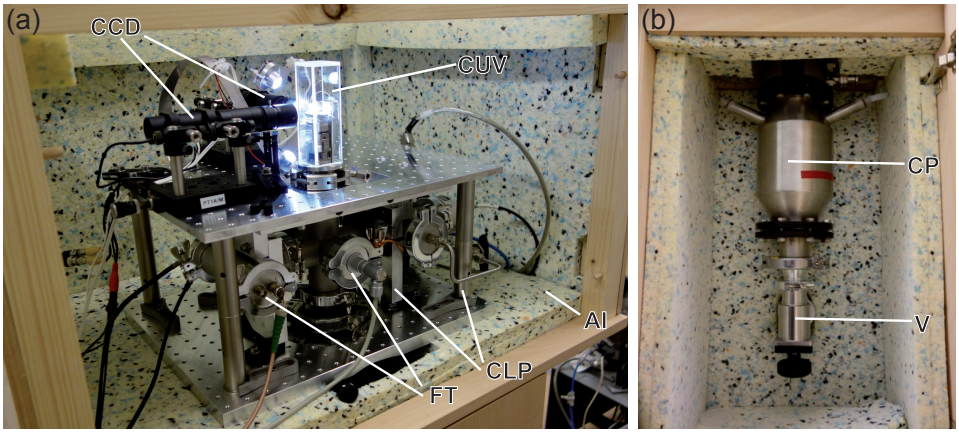

Figure 3.19: (a) Photograph of the measurement setup part situated inside the acoustic isolation box. The inner walls of the wooden box are faced with acoustic absorber panels (AI). A frame of two stacked aluminum bread boards hosts the vacuum chamber which is built from standard KF components and reinforced by solid external aluminum clamps (CLP). On the upper level of the frame a vacuum glass cuvette (CUV) encloses the cavity with sample and positioning unit. Two cameras (CCD) are installed to provide optical access to the experiment from orthogonal views. Between the two aluminum boards pressure sensors, electrical and fiber optical feedthroughs (FT) are situated. (b) The cryogenic pump (CP) is hooked up below to the vacuum chamber. The valve (V) allows disconnection of the pumping line leading out of the acoustically isolated environment to the turbo pump.

tograph of the part of the setup under the glass cover. The vacuum handling is sketched in figure 3.18(c). Pressure gauges are connected close-by the glass cell to indicate a realistic value of the pressure in the vicinity of the cavity. The cell is pumped by a cryogenic pump (CP), a turbo pump (TP) and a rotary pump (RP). Valves (V) enable controlled pumping and venting of the system. Carefully dosed purging of the rotary pump with nitrogen (N2) prevents contamination of the experiment with diffusing oil residues. The cryogenic pump, once filled with liquid nitrogen, operates self-sustained for half a day keeping the pressure at $10^{-5}\,\mathrm{mbar}$. Hence disconnecting the pumping line between the turbo pump and the valve inside AI the setup is ready to be operated without rigid connection to the outside environment in an acoustically shielded ambiance (AI).

In order to isolate the experiment, or to be more specific the cavity with the sample, from acoustic noise, two approaches are pursued. First the vacuum chamber which is built from standard KF components are reinforced by clamps (CLP) to suppress natural vibrations and second, the setup is packed in an acoustically shielded box to uncouple from vibrational sources like electric pumps or forced ventilation of electronic devices. Figure 3.19(a) and (b) present views into the acoustic isolation box. The inner walls of a wooden box are completely lined with acoustic isolation (AI), a heavy sound-absorbing sandwich of bituminized board between two mats of low-expansion foam. The glass vacuum cuvette (CUV) together with the cameras (CCD) are mounted on the top aluminum bread board. Below in the level between the two bread boards vacuum tubes are arranged tightly clamped in order to rigidify the vacuum chamber. Pressure gauges, fiber and electrical feedthroughs (FT) are flanged to these tubes. Further below (as seen in fig-

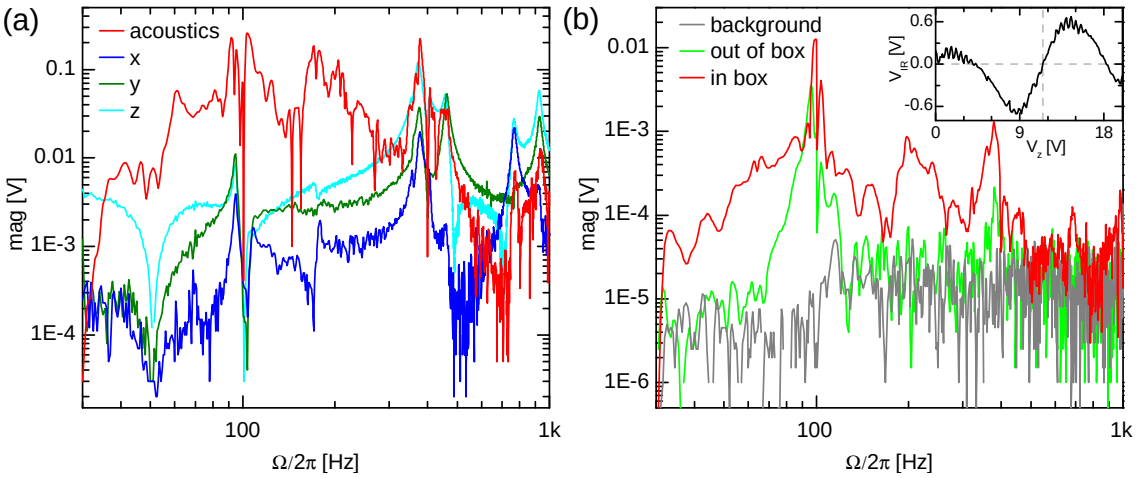

Figure 3.20: Noise transduction in the acoustic frequency range measured with the infrared interferometer and the broad beam shown in figure 3.15(a) inside the cavity. (a) Excitation source is connected to different stages of the positioning unit (blue, green, cyan) and to a speaker (red). (b) The speaker is located inside (red) and outside (green) of the closed box. The inset shows the interferometric signal V_{IR} with respect to the voltage V_z applied to the z-piezo positioner.

ure 3.19(b)) the cryogenic pump is installed with the valve (V) to disconnect the system from the pumping line coming from the turbo pump.

Acoustic noise in the frequency range from $30\,\mathrm{Hz}$ to $1\,\mathrm{kHz}$ has been identified as cause for vibrations of the sample relative to the cavity which limit the performance of the measurement setup. This is evident from measurements of the response of the setup to actuation at acoustic frequencies (shown in figure 3.20). Therefore the setup is subjected to excitation from a lock-in amplifier at different sites of the positioning unit and through a commercial speaker. The vibrations are detected with the $30\,\mu\mathrm{m}$ wide SiN beam (of figure 3.15(a)) inside the cavity using the interferometric setup (see chapter 3.2.3). The z-position of the test sample is set to the point of maximum sensitivity, say the steepest slope of the fringes of the interferogram as indicated by the dashed gray line in the inset of figure 3.20(b). Magnitudes of the interferometric signals are measured by the lock-in amplifier with respect to the excitation frequency. The different stages of the positioning unit exhibit different resonances (blue, green and cyan traces in figure 3.20(a)) that are all addressed through acoustics (red trace), too. More features in the speaker driven spectrum may originate from vibrations of the cavity mount. It remains to mention that for the measurements shown in figure 3.20(a) neither reinforcement of the vacuum chamber nor acoustic shielding had been installed. Acoustic spectra with installed reinforcement are shown in figure 3.20(b), where the speaker is located inside the acoustic shield (red) and outside (green). The stiffened vacuum chamber already blocks some features in the vibration spectrum, whereas the acoustic isolation on top reduces almost all vibrations to the limit of detection for this measurement (gray). Apart from a dominant peak around $100\,\mathrm{Hz}$ and a smaller one around $400\,\mathrm{Hz}$ the acoustic noise in the frequency range from $30\,\mathrm{Hz}$ to $1\,\mathrm{kHz}$ is suppressed by the two means up to two orders of magnitude.

3.4 Summary and outlook

A micro Fabry-Pérot cavity is assembled from optical fibers with micro-machined fiber ends that are coated with highly reflective Bragg mirrors. The cavity reveals a finesse of $33{\cdot}10^3 \pm 5\,\%$ and an effective length of $40.5\,\mu\mathrm{m}$. The lateral distribution of the optical mode tolerates a slit aperture of width down to $15\,\mu\mathrm{m}$ until optical losses become too strong for optomechanical measurements with nanomechanical objects. The experimental setup to conduct measurements comprises this cavity, a stabilized diode laser, cavity stabilization loop, interferometric detection and broadband spectroscopic analysis. Vacuum handling and acoustic vibration suppression are installed to isolate the setup from environmental disturbances. The high finesse and small mode volume of the cavity along with the setup in its completeness are perfectly suited for optomechanical studies with nanomechanical elements inside the cavity.

The presented procedure allows the design and assembly of fiber-based optical cavities covering a wide range of parameters. The choice of the mirror radius of curvature provides access to adopt the optical mode diameter and cavity length from very short with touching mirrors and minimal mode volumes to long cavities up to hundred micrometers with narrow resonances. Today mirror coatings are commercially available tailored for one specific or multiple wavelength ranges. Those coatings exhibit remarkably low dissipation, facilitating finesse values beyond 10^5. The cavity can be scanned across one free-spectral range which makes it suitable for tunable optical filter and optical spectrum analyzer applications. Doubly-clamped suspended samples reduce the influence of the environment on the measurements. Proper sample holders, as they are presented later in this work, are able to carry various samples into the cavity. In principal the cavity is compatible with cryogenic temperatures which, additional to the vacuum surrounding, will provide the best decoupling from environmental influence. Finally the fiber optical setup provides a versatile measurement system adoptable to different parameter ranges by minor modifications. It is accessible for various samples and physical systems like carbon nanotubes, nanowires [Fia10], defect centers in nanoparticles (e.g. nitrogen vacancy [Tis11], silicon vacancy [Neu11] and rare earth doped nanocrystals [Kol12]) and two dimensional materials (e.g. graphene [Poo08], hexagonal boron nitride [Son10] and molybdenum disulfide [Ye15]). According to the experimental requirements the setup can be extended to methods like cavity-enhanced Raman spectroscopy [Sum13], and time-resolved experiments [Rep14] through optical fiber connections. Combining multi-color excitation with higher order cavity modes facilitate measurements similar to the STED technique [Hel94].

Chapter 4

Carbon nanotube resonator

This chapter comprises work published in *Applied Physics Letters* in 2013 [Sta13]. It contains an introductory section motivating the measurements of the vibrational deflections of carbon nanotubes by optical means and pointing to the challenging bottleneck of the experimental realization. Following the device fabrication, characterization and the optical measurement setup are described. Measurements exhibit a sensitivity sufficient to clearly resolve the Brownian motion of the nanotube. Results are summed up in a discussion.

4.1 Motivation and challenges

Probing the vibrational motion of nano-scale objects has great potential for advancing next-generation technologies such as resonant mass or bio-sensing [Jen08, Cha12, Han12]. A key example is carbon nanotubes (CNTs), which, due to their molecular scale mass and diameter, promise to display ultimate sensitivities and may even allow to resolve the quantum nature of mechanical vibration in optomechanical experiments [WR12, Sch12]. However, small vibrational amplitudes and dimensions complicate the realization of CNT-based mechanical devices. One fundamental challenge is to resolve the thermally excited Brownian motion of CNTs to enable operation of the undriven device in the linear regime, and to limit the influence of spurious non-linear effects observed in CNTs [Eic11]. Transmission and scanning electron microscopy (TEM, SEM) have both been employed to visualize the thermal motion of CNTs [Tre96, Bab03], yielding a superposition of the small-amplitude envelopes of all oscillating modes. Electrical schemes are well-suited to detect vibrating CNTs, but typically require a coherent actuation voltage [Ste09, Cha12] and are typically not sensitive enough to resolve the Brownian motion. Dark field illumination was combined with confocal microscopy to detect the mechanical oscillation of driven CNTs with a diameter of $80\,\mathrm{nm}$, however, the Brownian motion amplitude could not be resolved with this approach [Fuk09]. Ultra-sensitive optical detection techniques [Arc06] are hindered by the diffraction limit, with typical tube diameters

much smaller than the wavelength of visible light. However, even in the sub-wavelength regime, the sensitivity can be enhanced by using an optical cavity [Fav08]. In earlier work a fiber-based optical micro-cavity of small mode volume and high finesse is employed to measure the Brownian motion of an amorphous carbon based nanorod with a diameter of about $100\,\mathrm{nm}$ [Fav09]. Following a proposal of cavity optomechanics with CNTs [Fav08], in the present work the nanorod is replaced by a carbon nanotube with a ten times smaller diameter. Taking advantage of an improved cavity with significantly increased finesse, data clearly resolving the Brownian motion of the CNT oscillating within the cavity light field is presented. The challenging tasks are first to have a substrate thin enough to provide clearance for navigation between the fiber ends. Second the substrate has to feature holes or slits with at least $18\,\mu\mathrm{m}$ width such that they do not contribute to optical losses by clipping the cavity mode. And third a CNT has to be suspended across these holes.

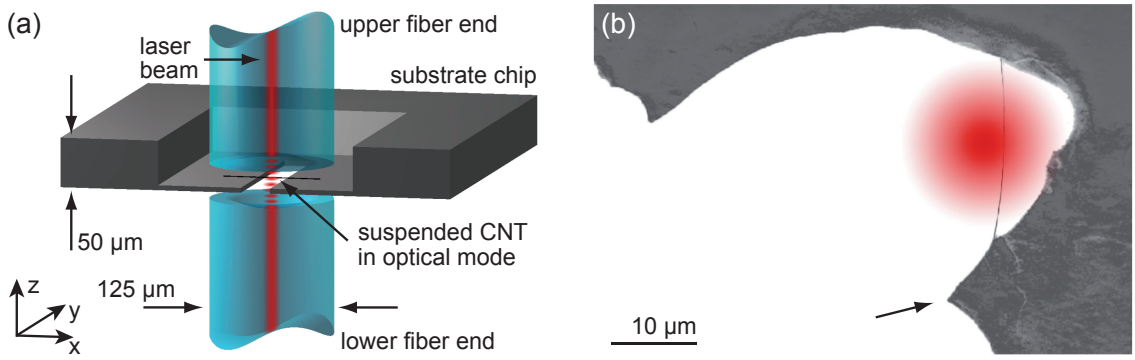

Figure 4.1: Illustration of the experimental setup. (a) Schematic view of cavity and sample chip with the CNT introduced into the cavity mode. (b) Illustration based on an SEM image of the CNT under investigation suspended across the gap (white) with surrounding substrate (gray). The red spot illustrates the position and extension of the optical cavity mode during the experiment.

The direct optical detection of a CNT of deep sub-wavelength dimensions is a challenging task [Fuk09]. In an optical cavity, however, the dispersive and dissipative interactions between the nanotube and the light field are enhanced. Particularly for a high finesse cavity of small mode volume, the signature of the CNT displacement in the cavity response is amplified. For the case of a dispersive interaction, the CNT imprints a phase shift on the photons in the cavity, which results in a resonance frequency shift of the cavity mode. On the other hand, a dissipative interaction, for example caused by absorption and scattering of photons, leads to decreasing the circulating optical power. The strength of both types of interaction depends on the position and orientation of the nanotube within the cavity mode. Thus by measuring the frequency and intensity of the cavity resonant response, information can be gained on these interactions. In the present work both dispersive and dissipative interaction of the CNT can contribute to the observed signal.

To detect the Brownian motion of the CNT, we employ a fiber-based micro cavity formed by two opposing, concavely shaped fiber end facets coated with highly reflective Bragg mirrors [Hun10, FJ12] (as illustrated in fig. 4.1(a)). For a mirror separation of

$37\,\mu\mathrm{m}$, the cavity optical mode waist radius is $3.4\,\mu\mathrm{m}$ and the finesse is measured to be $24,500$ for a wavelength of $780\,\mathrm{nm}$. The CNT is doubly clamped and freely suspended across a gap in the substrate as indicated schematically in fig. 4.1(a). The post-processed SEM micro-graph of the investigated nanotube in fig. 4.1(b) illustrates the position of the cavity mode with respect to the suspended tube during the experiment.

4.2 Fabrication and characterization of suspended CNT samples

Substrates with gaps serving as holders for freely suspended carbon nanotubes (CNTs) and with dimensions to fit into the cavity as sketched in figure 4.1(a) are fabricated using optical lithography and wet etching processes. Subsequently CNTs are grown across the gaps. Fabrication of CNT samples is explained in detail in reference [Ost10]. SEM and TEM analysis reveal dimensions and vibrational behaviour of doubly-clamped freely suspended CNTs.

4.2.1 Substrate fabrication

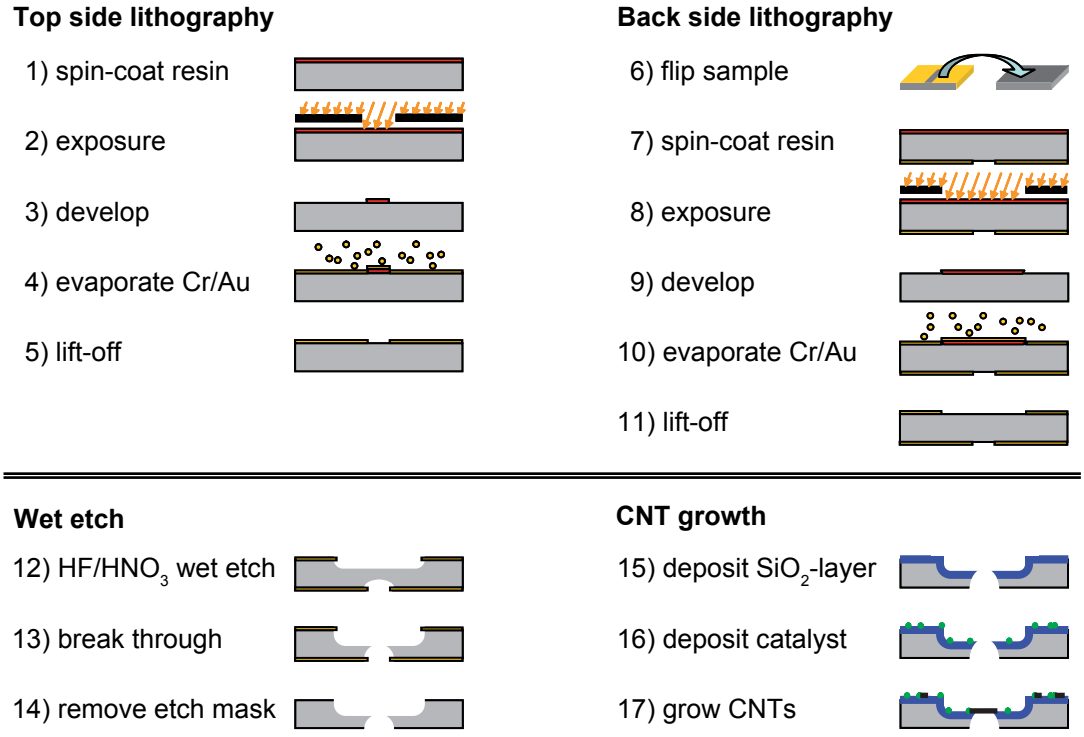

Figure 4.2: Sample processing step by step.

Sample processing steps are depicted in figure 4.2. Suitable substrate chips to serve as holders for the CNTs are fabricated starting from a $50\,\mu\mathrm{m}$ thick silicon wafer. Photo lithography and a lift-off process after evaporation of $4\,\mathrm{nm}$ chromium (Cr) and $50\,\mathrm{nm}$ gold (Au) (steps 1 through 11) performed on both sides of the wafer define the etch mask for the subsequent isotropic silicon wet etch, a mixture of $\mathrm{HNO_3}\,(65\,\%) : \mathrm{HF}\,(49\,\%)$ at ratio $98 : 2$ for about $60\,\mathrm{min}$ (steps 12 and 13). After the etch mask is removed (step 14) in aqua regia ($\mathrm{HCl}\,(37\,\%) : \mathrm{HNO_3}\,(65\,\%)$ at ratio $3 : 1$) the chips are rinsed with water and isopropanol and dried with a nitrogen air gun. This results in a rectangular region on one side of the chip thinned down to approximately $20\,\mu\mathrm{m}$ and perforated with a series of holes with diameters ranging from 10 to $50\,\mu\mathrm{m}$ as shown in figure 4.3(a).

4.2.2 CNT growth

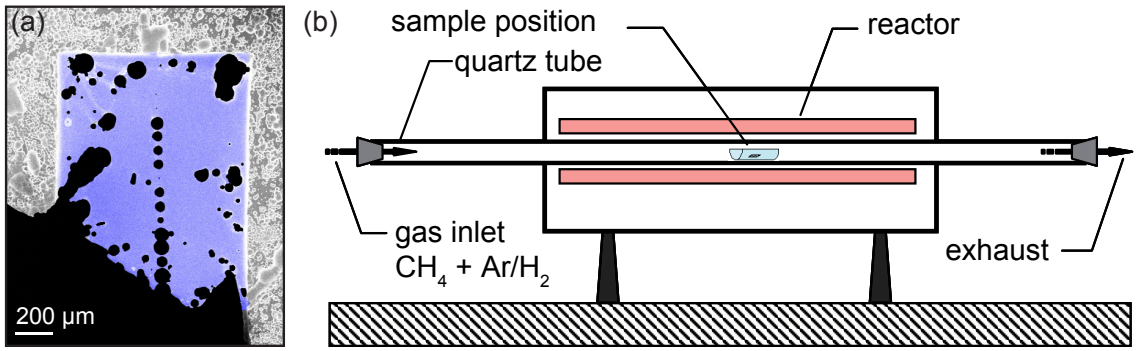

Figure 4.3: (a) The SEM image shows the silicon substrate chip (spotted gray) with thin etched and perforated region (homogeneous, blue) and holes (black). (b) Sketch of the CVD reactor used for CNT growth.

The subsequent CNT growth process is adapted from the method developed by the group of Christian Schönenberger at the Unversity of Basel [Bab03]. The substrate chips are coated with a $170\,\mathrm{nm}$ thick silicon oxide ($\mathrm{SiO_2}$) layer deposited by plasma-enhanced chemical vapor deposition (PECVD) (figure 4.2 step 15). In the following, nanocrystalline catalyst particles, a mixture of $\mathrm{Fe(NO_3)_3 - 9H_2O}$, $\mathrm{Al_2O_3}$ and $\mathrm{MoO_2Cl_2}$ (Iron(III) nitrate nonahydrate, P/N 254223; Aluminum oxide, P/N 551643; Molybdenum(VI) dichloride dioxide, P/N 373710; all *Sigma-Aldrich*) suspended in isopropanol, are deposited on top of the $\mathrm{SiO_2}$ by evaporation of the solvent (step 16). CNTs were grown (step 17) using a chemical vapor deposition (CVD) process in a quartz tube reactor at $900\,^{\circ}\mathrm{C}$ for $10\,\mathrm{min}$ at atmospheric pressure as sketched in figure 4.3(b). The process gas is a mixture of hydrogenated argon ($\mathrm{Ar}\,(95\,\%) : \mathrm{H_2}\,(5\,\%)$) and methane $\mathrm{CH_4}$ at flow rates of $1.0\,\mathrm{SLM}$ (standard liter per minute) and $0.5\,\mathrm{SLM}$, respectively.

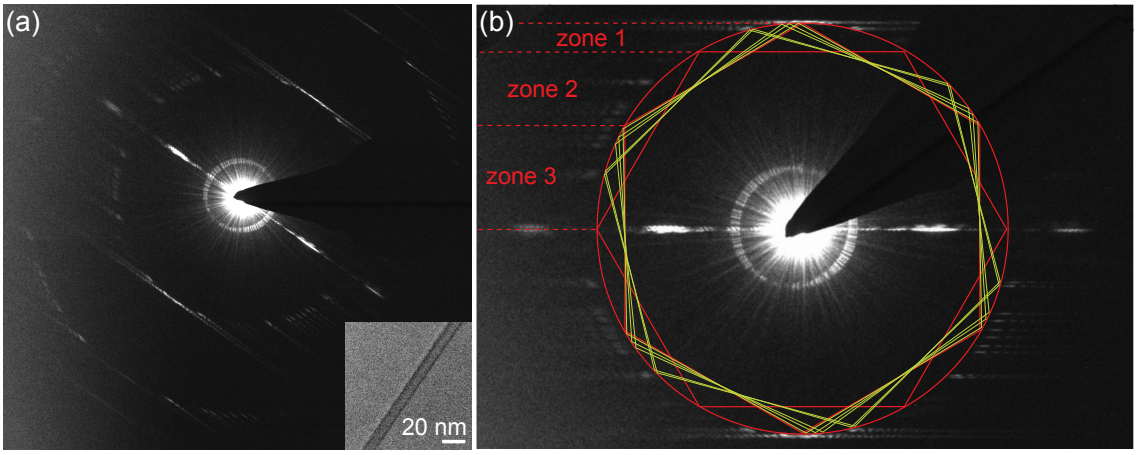

Figure 4.4: (a) Electron diffraction pattern of a CNT obtained from TEM measurements. An image of the CNT at the position of the diffraction measurement is shown in the inset. (b) Same diffraction pattern but rotated and with overlays as guide to the eye: Red circle indicates the location of Bragg reflexes. Corners of red hexagons mark points where signatures of CNTs with armchair or zig-zag chirality would occur. These points are used to divide each quadrant of the pattern into three zones. Corners of green hexagons follow Bragg features originating from shells and/or tubes with different chirality composing the CNT. The investigated CNT is thus made up of 7 SWNTs.

4.2.3 CNT geometry

Careful measurements in the TEM and SEM on different samples show that CNTs grown across gaps as described in the previous section 4.2.2 can have suspended lengths of up to $25\,\mu\mathrm{m}$. Diameters of tubes suspended on a length larger than $10\,\mu\mathrm{m}$ range from 4 to $8\,\mathrm{nm}$. Electron diffraction analysis in TEM makes clear that such long CNTs are not single-walled (SWNT) but rather multi-walled or ropes consisting of 5 to 7 individual shells or tubes. An image of a diffraction pattern is depicted in figure 4.4(a), along with an image of the corresponding CNT in the inset. The diffraction image exhibits horizontally extended Bragg reflexes starting at points on a concentric circle around the bright central peak The same diffraction pattern but rotated and with red circle as guide to the eye is repeated in figure 4.4(b). Apart from the black shadow protruding towards the pattern center, which is caused by the beam block, the image is symmetric about the horizontal and vertical axis. We use a simplified version of the procedure detailed in reference [Den10] to interpret the diffraction patterns. To this end each quadrant of the pattern is structured into three zones whose borders are given by the corners of the red hexagons. These corners indicate the starting points of horizontal Bragg reflexes that would occur if an armchair and a zig-zag SWNT were involved. Each SWNT will exhibit the same diffraction pattern, rotated about an angle depending on chirality. The number of horizontal Bragg reflexes within one zone including its borders is equal to the number of SWNTs contributing to the pattern (see green hexagons in figure 4.4(b)). Thus 7 SWNTs contribute to the displayed diffraction pattern.

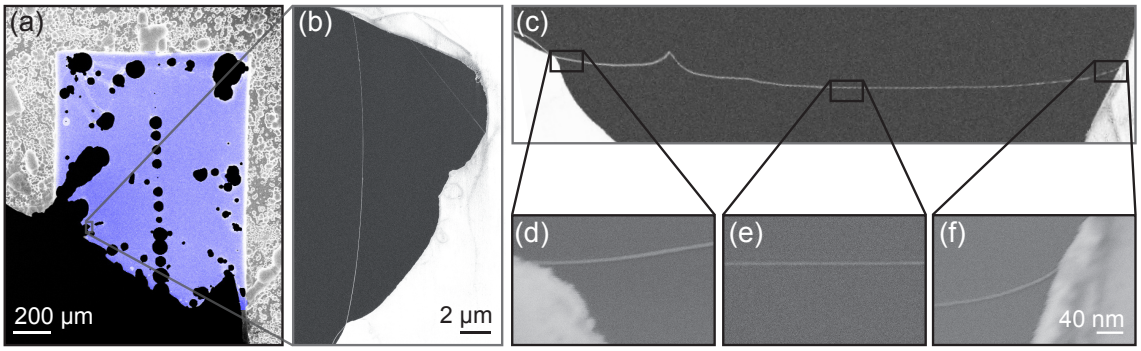

Figure 4.5: SEM images of the sample chip (a) and the CNT under investigation (b-f). The gray rectangle in (a) marks the position of the CNT. (b) Zoom showing the CNT under investigation (vertical white line) which is doubly clamped, slightly bent and freely suspended across a distance of $19.7\,\mu\mathrm{m}$ in a corner of the substrate (white). (c) shows the same view as (b) but rotated by $90°$. Kink in CNT occurred once during scanning indicating slack-induced movement and/or the occurrence of conformational changes of the CNT. Black rectangular sections along the CNT at both clamping points and in the middle in mark areas where high-resolution SEM images are taken and shown below in (d-f).

Figure 4.5(a) shows a SEM image of the sample chip with a zoom (b) to the CNT under investigation. The tube is freely suspended across a distance of $19.7\,\mu\mathrm{m}$ and its slight wavy shape indicates the absence of tensile stress along the growth axis. Note that this CNT moved a little bit during SEM scanning leading to the kink displayed in figure 4.5(c). The diameter of the tube is measured from high-resolution SEM images (figure 4.5(d-f)) at three positions. It is $8\,\mathrm{nm}$ and $7\,\mathrm{nm}$ near the clamping points (d) and (f) and $6\,\mathrm{nm}$ at a central position (e), which is consistent with TEM measurements of comparable samples.

4.2.4 Dynamical characterization

Vibrational modes of the CNT are investigated in the SEM. In order to visualize the vibrational modes, external actuation through a piezo electric element is employed (as described later in section 4.3.1). Compared with the case of no excitation figure 4.6(a) the CNT image is found to blur upon applying a white noise signal ($14\,\mathrm{dBm}$ with $20\,\mathrm{MHz}$ bandwidth) figure 4.6(b). This blurring shows the superposition of the envelopes of the simultaneously excited flexural oscillation modes [Bab03]. Driving the sample by a sinusoidal signal of $14\,\mathrm{dBm}$ power allows to isolate individual vibrational modes in the range between 0.1 and $1\,\mathrm{MHz}$. This enables identifying CNT mechanical modes at $0.153\,\mathrm{MHz}$, $0.168\,\mathrm{MHz}$, $0.215\,\mathrm{MHz}$, $0.377\,\mathrm{MHz}$, $0.51\,\mathrm{MHz}$, $0.864\,\mathrm{MHz}$, $0.907\,\mathrm{MHz}$ and $0.923\,\mathrm{MHz}$, where most of them are presented in figure 4.6(c-i). The envelopes of the modes up to $0.907\,\mathrm{MHz}$ have strong similarity to the mode profile of the fundamental mode of an elastic beam, where the one at $0.923\,\mathrm{MHz}$ resembles the profile of the first overtone with one node in the center. Since this CNT is not an ideal symmetric and homogeneous elastic beam several modes with fundamental-like profile exist. The resonance at $0.51\,\mathrm{MHz}$ (f)

exhibits the largest amplitude. Measuring the vibrational deflection and sweeping the drive frequency across this resonance at much lower drive power allows to estimate the quality factor to be about 250 ± 50.

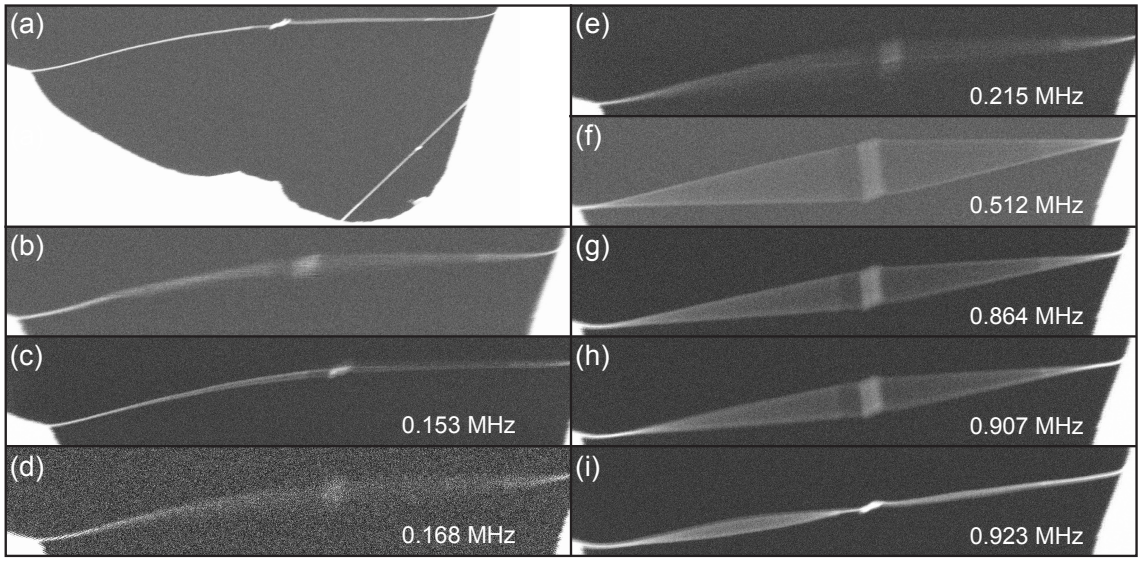

Figure 4.6: SEM images of the CNT (a) at rest and (b) driven with broadband noise. (c-i) The tube is excited at resonance frequencies as indicated.

It has to be noted that electron beam induced deposition on the CNT affects the mechanical properties, but by exposing the tube to the electron beam only at small areas during frequency scanning and taking single shot images this effect is minimized such that no obvious down-shift in resonance frequency has been observed. However, presented SEM analysis has been performed after measurements inside the optical cavity which are discussed in the following section. Thus results from optical measurements are gained from a clean CNT sample.

4.3 Brownian motion of a carbon nanotube

For the optical detection of the motion of a sub-wavelength sized CNT the cavity described in section 4.1 is used. In the following the setup as a whole and the performed measurements are described. The results are discussed and supported by further considerations.

4.3.1 Optical setup

For optical measurements of CNT vibration the substrate chip is introduced into the fiber-based cavity as illustrated in figure 4.1. The experiments are carried-out in a custom fiber-compliant vacuum cell (VAC) at a pressure of $10^{-5}\,\mathrm{mbar}$ and at room temperature

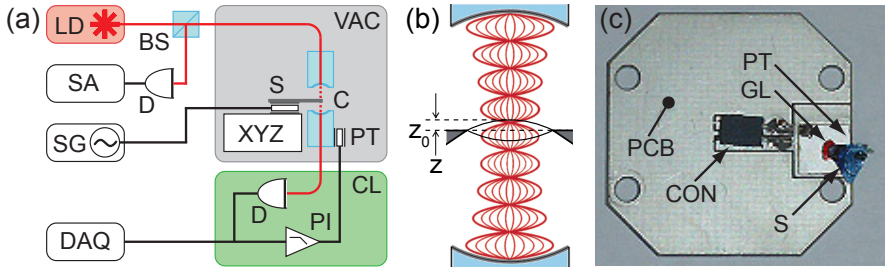

Figure 4.7: (a) Schematics of the experimental setup. (b) Illustration of the cavity with the CNT resonating with amplitude z around equilibrium position z_0 in the optical mode. (c) Photograph of the sample chip glued to the excitation piezo and mounted at the border of a circuit board ready for insertion into the cavity.

(300 K), see figure 4.7(a). A three axis XYZ-positioner allows accurate placement of the CNT inside the cavity (C). Optionally a piezo transducer (PT) underneath the sample chip (S) can be used to excite the mechanical motion of the CNT via a signal generator (SG). The cavity is pumped with a stabilized diode laser (LD) at 780 nm. The transmitted light is sent to a photo detector (D), monitored on an oscilloscope (DAQ) and used to lock the cavity (CL) on a slope of an optical resonance. Therefore an electronic feed-back loop (PI) acts on a piezo (PT) controlling the cavity length. The reflected light intensity is sensitive to both dissipative and dispersive components of the cavity field-CNT interaction. At the beam splitter (BS) the light reflected from the cavity is directed to a second photo detector (D). The CNT vibration is measured by analyzing the optical noise of the reflected light (spectrum analyzer, SA). Positioning of the CNT is ideally between a node and an anti-node of the standing wave pattern such that no clamps or substrate features protrude into the optical mode. This is illustrated in figure 4.7(b) along with the mean position z_0 and maximum vibrational deflection z of the oscillating tube. A circuit board (PCB) forms the basis of a typical sample holder shown in figure 4.7(c). It hosts the sample chip (S) that protrudes the outline of the PCB. The chip is glued to a piezo electric transducer (PT) with a droplet of photo resists (GL). The piezo is soldered to the PCB and the electrical signal for excitation can be provided through a miniature connector (CON).

4.3.2 Measurements in the cavity

The optical power transmitted on the empty cavity resonance is 0.56 μW. Bringing the CNT into the optical mode, as illustrated by the red spot in figure 4.1(b) the cavity transmission drops by 29 %. This drop is predominantly caused by residual clipping losses originating from the presence of the hosting substrate edges near the CNT. The CNT vibration is analyzed by probing the optical noise of the reflected light with a spectrum analyzer. When locked on the slope of the cavity resonance, the vibrational motion of the CNT is first characterized under external actuation from a drive piezo mounted below the substrate chip. Under white noise actuation (14 dBm with 20 MHz bandwidth), a series of resonances is clearly observed above the noise floor (figure 4.8(a) red trace). The main peak at 0.51 MHz is the fundamental flexural mode of the tube. This peak

and other spectral features (black arrrows) are identified as mechanical resonances of the CNT through SEM experiments (see chapter 4.2.4). The main peak at $0.51\,\mathrm{MHz}$ rises more than $20\,\mathrm{dB}$ above the noise floor, even when the piezo is not driven (figure 4.8(a) blue data). A Lorentzian fit to the data points of the undriven resonance after subtraction of the reference background (figure 4.8(b) red line) yields a quality factor of 300. This cavity noise peak is calibrated to the Brownian motional amplitude of the CNT according to section 2.1.3 exploiting the equipartition theorem given in equation 2.47. Interestingly, this signal peak is not stable in frequency but fluctuates slowly between $0.47\,\mathrm{MHz}$ and $0.52\,\mathrm{MHz}$ on the timescale of minutes. We suggest that slack and conformational instability of the tube, which are also observed in the SEM, contribute most to this behavior. Furthermore, a strong dependence of the signal amplitude on the position of the CNT in the optical mode is observed. The resonance vanishes completely when the CNT is positioned a few microns away from the optical mode axis. Further information is obtained when the sample is positioned such that the optical mode hits a protrusion of the hosting substrate (for example at the position indicated by a black arrow in figure 4.1(b), about ten microns away from the CNT). With this protrusion entering the optical mode, the drop in cavity transmission is still of order $29\,\%$ but the spectrum does not exhibit the resonance near $0.51\,\mathrm{MHz}$ (figure 4.8(a) gray trace). Instead a series of extra peaks below $0.22\,\mathrm{MHz}$ appear. When comparing with background measurements without any sample inside the cavity (black trace) these peaks most probably originate from vibrating substrate modes. Such substrate resonances are not observed above $0.22\,\mathrm{MHz}$, corroborating that the main resonance at $0.51\,\mathrm{MHz}$ does not stem from a substrate mode. The cavity resonant transmission exhibits constant values for the CNT being placed at several z_0-positions inside the cavity. The fact that the presence of the CNT does not lead to additional cavity losses is interpreted by a dominating influence of clipping losses to the dissipative signal component. This implies that the nanomechanical motion detection relies primarily on the dispersive interaction.

4.3.3 Discussion

Conventional Euler Bernoulli theory allows for a satisfactory estimate of the resonance frequency $f_1 = \Omega_1/(2\pi)$ of the fundamental flexural oscillation of the measured CNT [Bab03, Mar07] according to equation 2.30. Values for Young's modulus E in the range of $0.3 \ldots 1\,\mathrm{TPa}$ can be found in literature [Sal99, Ruo03, Löf11]. Based on TEM analysis we consider the observed CNT to be either a multiwall nanotube or a rope comprising five to seven individual tubes with a total outer diameter d_o between 6 and $8\,\mathrm{nm}$. The area moment of inertia $I = \pi(d_\mathrm{o}^4 - d_\mathrm{i}^4)/64$ and the cross-section area $A = \pi(d_\mathrm{o}^2 - d_\mathrm{i}^2)/4$ are used for multiwall nanotubes with the inner diameter $d_\mathrm{i} = d_\mathrm{o} - n\,\Delta_\mathrm{s}$, the number of walls n and the inter wall spacing $\Delta_\mathrm{s} = 0.335\,\mathrm{nm}$, and for ropes with $d_\mathrm{i} = 1\,\mathrm{nm}$. The physical mass density ρ is inferred from the mass density of graphite $\rho_\mathrm{graphite} = 2200\,\mathrm{kg/m^3}$ along with n, Δ_s and geometrical considerations for both cases. Entering the above input parameters into equation 2.30 yields an estimated resonance frequency between 0.16 and $0.63\,\mathrm{MHz}$,

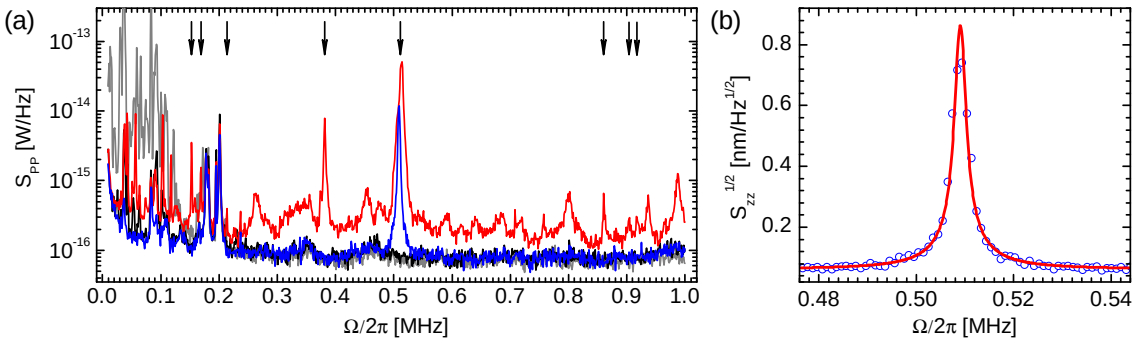

Figure 4.8: (a) Power spectra reveal the CNT's vibrational spectrum. The red trace is obtained with the CNT placed in the cavity mode and $14\,\mathrm{dBm}$ of white noise is applied to the drive piezo, whereas for the blue trace the drive is switched off. The remaining peak near $0.51\,\mathrm{MHz}$ rising more than $20\,\mathrm{dB}$ above the noise floor evidences the Brownian motion of the CNT. Black arrows point at peaks confirmed as mechanical resonances of the CNT by SEM experiments. Background signals recorded with active noise drive are displayed in black where no feature of the sample is in the cavity and in gray where only the corner of the substrate (indicated by the black arrow in figure 4.1(b)) protrudes into the optical mode. (b) Brownian vibrational amplitudes are calibrated and shown in the zoomed plot of the CNT's Brownian noise peak with subtracted background and Lorentzian fit (red).

which is consistent with the frequencies of the CNT measured in the SEM and in the cavity.

The calibration of the Brownian motional amplitude given in figure 4.8(b) requires the temperature $T = 300\,\mathrm{K}$, spring constant $k_{\mathrm{eff},1} = \Omega_1^2\, m_{\mathrm{eff},1}$ and the effective mass $m_{\mathrm{eff},1}$ of the fundamental flexural mode. According to equation 2.40a $m_{\mathrm{eff},1}$ is calculated with $\phi_1(\xi)$ and $\eta(\xi)$ in normal coordinate $\xi = x/l$ and constants for the parameters as specified ($l = 19.7\,\mu\mathrm{m}$ and $w_0 = 3.4\,\mu\mathrm{m}$). For the fundamental flexural mode $m_{\mathrm{eff},1} = 0.45\,m = 0.1 \ldots 0.9\,\mathrm{fg}$ [Eki05] is derived from the physical mass $m = \rho\, l\, A$. The large uncertainty in the mass stems from the above-mentioned uncertainty in the composition and diameter of the tube and translates into an error of $50\,\%$ for the calibration. Thus the Brownian motion peak amplitude of the nanotube of $0.9\,\mathrm{nm} \pm 50\,\%$ is measured with a sensitivity of $70\,\mathrm{pm/Hz^{1/2}} \pm 50\,\%$.

One possible effect distorting the calibration of the CNT Brownian amplitude is heating of the CNT by absorption of laser light. Neglecting optical losses by clipping on the hosting substrate and scattering losses induced by the CNT, the extreme case is envisioned where all optical power lost in the cavity is absorbed by the CNT and turns into heat. Heat generated in the illuminated section of the CNT (c.f. figure 4.1(b)) propagates along the CNT to the clamps and dissipates into the thermal bath of the substrate. Using the heat transfer model presented in section 2.1.4 with the thermal conductivity [Hsu09] $\kappa_{\mathrm{T}} = 118\,\mathrm{W/(m\,K)}$ of a comparable CNT of length l and cross-section A yields an maximal temperature increase along the CNT of $150\,\mathrm{K}$ according to equation 2.50. Under the above extreme assumptions the CNT would oscillate at an elevated vibrational temperature with larger Brownian amplitude, entailing a correction of the measurement

calibration by a factor 1.2, which is smaller than the uncertainty coming from the CNT mass estimation.

Furthermore optomechanical back-action could actuate the CNT and modify the mechanical resonance and linewidth [Fav08]. However, an estimate of the maximum increase in vibrational temperature due to dynamical backaction [Met08] yields at most a few kelvins and is thus negligible in our experiment. Further, we extract similar Q-values from measurements in the cavity and in the SEM, strongly indicating that the CNT is not driven optomechanically.

Assuming a purely dispersive optomechanical interaction, the effect of the thermal displacement of the CNT on the cavity reflection is estimated using the dispersive cavity frequency shift of equation 2.52 with permittivity for CNTs $\epsilon_\mathrm{r} \approx 3$ [Hee95]. For the fundamental flexural mode of the investigated CNT and in case of perfect alignment of the tube orthogonal to the TEM_{00} cavity mode axis, the integral of equation 2.52 leads to a maximal frequency-pull coupling rate $g_\omega = \partial\omega_\mathrm{c}/\partial z$ of $(2\pi)\,1\,\mathrm{MHz/nm}$ along the cavity axis. Assuming the dispersive detection is performed with the CNT centered between a node and an anti-node of the optical field, the employed laser power and detector response predict a peak cavity reflection noise power of $1\,\mathrm{pW/Hz}$ for the Brownian motion of the CNT. A more realistic estimate includes a finite tilt of the CNT with respect to the wavefronts of the cavity field. For an angle of $7°$ consistent with the alignment tolerance under binocular inspection, a peak value of $10\,\mathrm{fW/Hz}$ is computed which agrees with the experimentally observed signal. This independently supports the identification of the $0.51\,\mathrm{MHz}$ resonance as Brownian motion of the fundamental flexural mode.

4.4 Summary and outlook

Optical cavities with small mode volume are well-suited to detect the vibration of subwavelength sized objects like carbon nanotubes. The fabrication of CNT samples suitable for the use in a fiber-based, high-finesse optical microcavity is reported. Optical detection of the Brownian motion of the fundamental mode of the nanotube at half a megahertz is demonstrated with a sensitivity down to $70\,\mathrm{pm/Hz^{1/2}}$. These results are complemented by beam theory calculations and signal amplitude estimations. Further a full vibrational spectrum of the carbon nanotube is obtained and confirmed by characterization of the same device in a scanning electron microscope. This work extends the principles of high-sensitivity optomechanical detection to molecular scale nanomechanical systems.

Being the smallest solid-state mechanical resonators available to date along with their relatively large zero point amplitude $z_\mathrm{zpf,1} = (\hbar/(2\,m_\mathrm{eff,1}\,\Omega_1))^{1/2}$ make CNTs an interesting candidate for optomechanical studies. For the tube investigated in the present work $z_\mathrm{zpf,1} = 8.2\,\mathrm{pm}$. With an improved yet technically feasible cavity line width $\kappa/(2\,\pi) = 20\,\mathrm{MHz}$ and for good alignment of the CNT to the optical mode, a zero point equivalent optomechanical coupling rate $g_0 = g_\omega\,z_\mathrm{zpf,1} = (2\pi)\,8.2\,\mathrm{kHz}$ is expected. Cryogenic environment can boost the mechanical quality factor of the CNT [Ste09] beyond 10^5, which

would place the system deeply into the strong coupling regime [Teu11b, SN11]. This is apparent form the cooperativity $C = 4g_0^2\, n_\mathrm{c}\, Q_1/(\kappa\, \Omega_1)$, an important figure of merit for optomechanical systems, which relates the zero point optomechanical coupling rate g_0, the intracavity photon number n_c, the cavity linewidth κ and the mechanical damping rate Q_1/Ω_1. For the described parameters a cooperativity per photon $C_0 = C/n_\mathrm{c} = 2.7$ can be expected, which is higher than that reported in state-of-the-art[1] optomechanical experiments [Teu11b, SN11].

[1] stated in 2013, when the article published

Chapter 5

Silicon nitride resonators

Stoichiometric or close to stoichiometric silicon nitride (Si_3N_4 or SiN) provides a material well suited for high quality factor micro- and nanomechanical resonators [Ver08a, Unt09] and thus for the use in optomechanics experiments [Tho08, Ane10b, Bak12]. Its fabrication and processing is well established in semiconductor technology, however geometric constraints complicate the use of SiN resonators in the cavity as illustrated in figure 5.1(a). Conventional resonators on top of a substrate do not work here as usual substrates are to thick to enter the roughly $30\,\mu\mathrm{m}$ tight cavity gap and it would introduce way to much optical loss for the cavity mode. Thus SiN resonators suspended across a hole through the substrate are structures best to be measured in the cavity (figure 5.1(b)). Fabrication of such samples is explained as well as their mechanical characteristics and interactions with the optical cavity mode are discussed in the following.

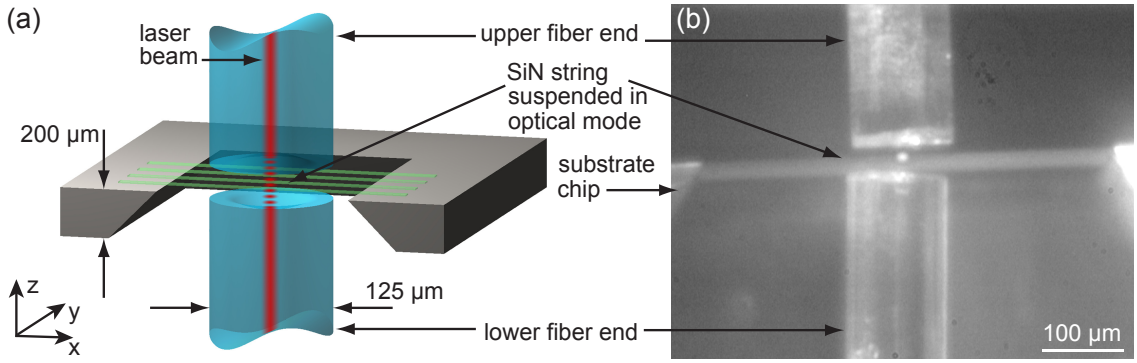

Figure 5.1: Illustration of the experimental setup. (a) Schematic view of cavity and sample chip with the SiN resonators introduced into the cavity mode. (b) Micrograph of the cavity with sample introduced. The bright spot in center shows light of the cavity mode scattered by the SiN string.

5.1 Processing of SiN membranes

Processing of freely suspended SiN structures starts with commercially available membrane chips purchased from *Norcada* (figure 5.2(a) (0.)). These are $200\,\mu\mathrm{m}$ thick silicon chips that already have a central $500\,\mu\mathrm{m}$ square window. A $50\,\mathrm{nm}$ thin Si_3N_4 membrane spans across this window and is structured using standard planar film processing methods. However the thin fragile membrane requires special care for handling, wet chemical treatment and spin coating resist. On top isolating properties complicate reproducible lithography by electron beam techniques because of charging and undesired deflection of the beam. Hence processing methods successfully developed for patterning dielectric substrates [Fau12] are adopted and applied. Detailed processing parameters are given in appendix B. The fabrication procedure is depicted in figure 5.2(a) where for each step a top view and a cross-section of the sample are sketched.

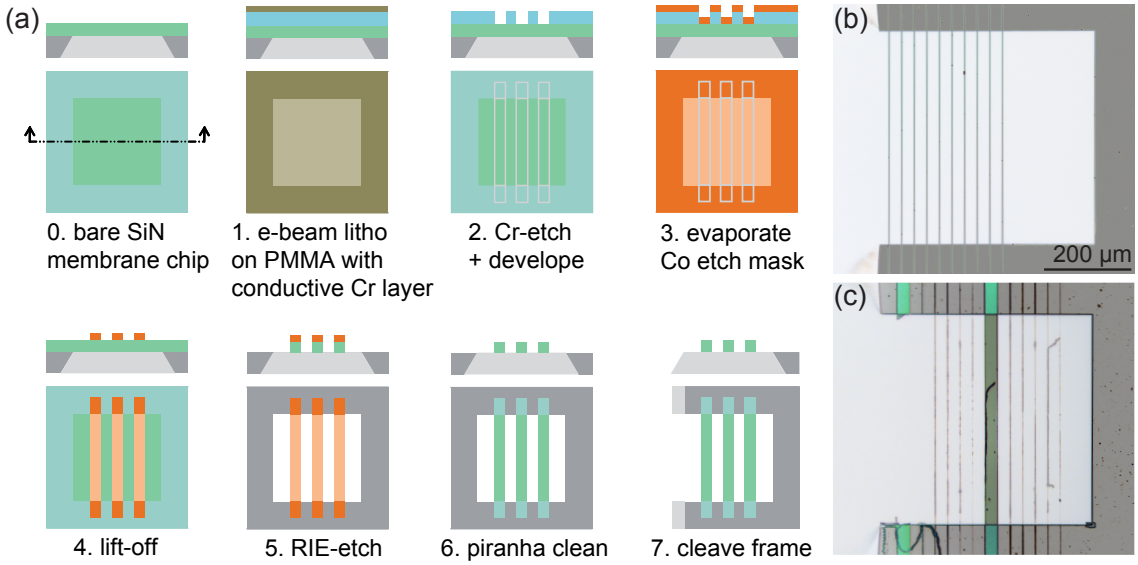

Figure 5.2: (a) Step by step structuring of silicon nitride membranes. For each step the top view (lower image) and cross-section (upper image) of the sample are sketched. Colors encode materials: silicon (gray), SiN (green), PMMA (blue), Cr (brown), Co (orange). Processed micrographs of structured $50\,\mathrm{nm}$ thin $500\,\mu\mathrm{m}$ square SiN membranes are shown in (b) and (c). Resonators widths are (b) $2\,\mu\mathrm{m}$ and (c) $80\,\mathrm{nm}$, $150\,\mathrm{nm}$, $280\,\mathrm{nm}$, $500\,\mathrm{nm}$, $700\,\mathrm{nm}$ and $30\,\mu\mathrm{m}$. The two leftmost struktures in (c) are broken.

Processing steps are described as follows: (1.) For strings with $2\,\mu\mathrm{m}$ width and more a PMMA layer is spun on the sample for electron beam lithography. Therefore the membrane chip is fixed by tape to the turntable of the spin coater since ordinary vacuum fixation destroys the membrane. Additionally $2\,\mathrm{nm}$ of chromium (Cr) are deposited on top by thermal evaporation. This layer prevents the membrane from charging during exposure and thus ensures non-distorted electron lithographic patterning of the PMMA. (2.) Removal of the Cr-layer by chemical wet etching is performed before PMMA is developed. (3.) Metal etch mask (Co, cobalt) of $20\,\mathrm{nm}$ thickness is deposited by electron beam evaporation directly onto the SiN layer. (4.) PMMA with Co on top is lift-off. (5.) Reactive

ion etch (RIE) removes all SiN except underneath the Co layer. (6.) A wet chemical piranha etch removes the Co mask. The fragile suspended structures only withstand gentle agitation in liquid. (7.) Cleaving-off one side of the Si frame enables the introduction of the sample into the cavity. Cleaving is faciltated by the anisotropically etched window of the membrane chips (c.f. cross-sectional views in figure 5.2). For cleaving the sample is sandwiched between two glass slides and the cleaving edge is oriented parallel to one window edge. This way no further scratching of the Si substrate is needed.
For structures with very small lateral dimensions wet chemical treatment is not an option. Alternatively a negative e-beam resist (AR-N 7500.08, *allresist*) is used instead of PMMA in step (1.) that serves directly as masking material for the RIE (in 5.). Thus steps (3.) and (4.) are not used and the cleaning (6.) is performed in an oxygen plasma.

Images of resulting structures are shown in figure 5.2(b) and (c). For both, the silicon frame is opened on the left. A sample with series of ten $2\,\mu\mathrm{m}$ wide strings separated by $30\,\mu\mathrm{m}$ is presented in (b). Two sets of structures with widths of $80\,\mathrm{nm}$, $150\,\mathrm{nm}$, $280\,\mathrm{nm}$, $500\,\mathrm{nm}$, $700\,\mathrm{nm}$ and $30\,\mu\mathrm{m}$ are realized in (c) whereas the two leftmost features are broken. The sample in (c) is fabricated with the alternative procedure. Samples fabricated with the firstly presented, wet method are cleaner and have better mechanical performance than those made by the second, dry method. Complete dry processing leaves more particles on the structures and the overall yield is rather poor.

5.2 Characterization of SiN resonators

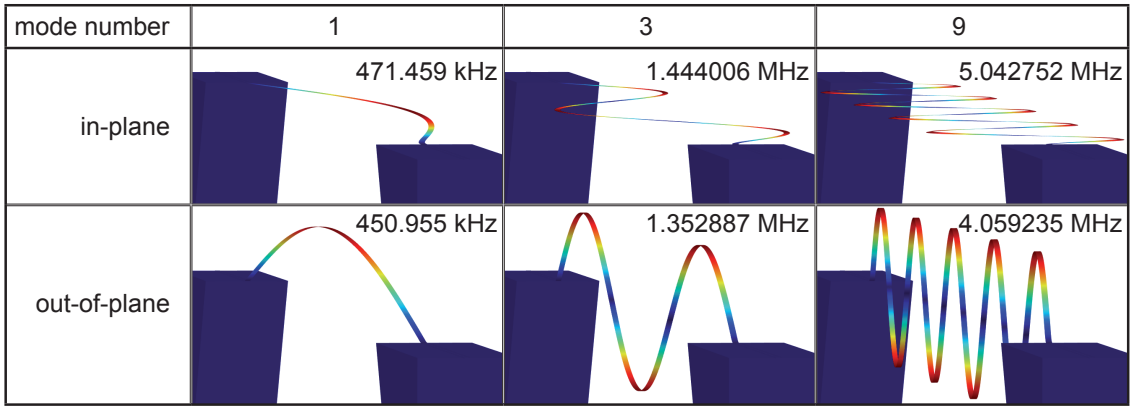

Figure 5.3: Finite element simulation of first, third and ninth modes of in-plane and out-of-plane vibrations of a $500\,\mu\mathrm{m} \cdot 2\,\mu\mathrm{m} \cdot 50\,\mathrm{nm}$ SiN string. Color encodes the deflection of the string from equilibrium, blue blocks are sections of the silicon substrate. Resonance frequencies as obtained from the simulations are written to each picture.

Finite element simulations (*COMSOL*) of the mechanical vibrational modes results in a rich mode spectrum. Besides the geometry (thickness $t = 50\,\mathrm{nm}$, width $w = 2\,\mu\mathrm{m}$ and length $l = 500\,\mu\mathrm{m}$) of the resonators, material parameters of SiN like mass density

$\rho = 3100\,\mathrm{kg/m^3}$ and Young's module $E = 250\,\mathrm{GPa}$, a tensile stress of $\sigma = 810\,\mathrm{MPa}$ for the SiN-layer are included in the numerical model. Example deflection profiles and resonance frequencies of the in-plane (ip) and out-of-plane (oop) vibrational modes of the first, third and ninth harmonics are illustrated in figure 5.3. Fundamental frequencies are a bit below half a megahertz ($0.471\,\mathrm{MHz}$ for the ip mode and $0.451\,\mathrm{MHz}$ for the oop mode). Up to the ninth harmonic the frequencies of oop modes are very well described by the model of a stretched string given in equation 2.32. Forty fold width compared to thickness leads to a higher contribution of material elasticity for the ip modes and thus their resonance frequencies rise quicker with the mode index than those of the oop modes.

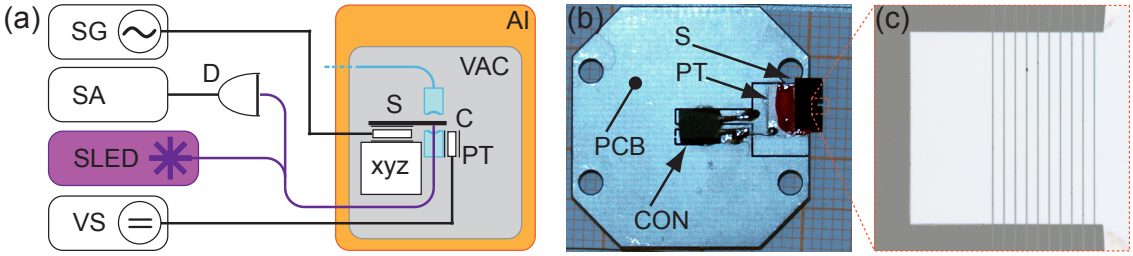

Figure 5.4: (a) Fiber integrated interferometer setup for measurements of pure mechanical properties of the sample. Labels indicate signal generator (SG), spectrum analyzer (SA), photo detector (D), super luminescent light emitting diode (SLED), voltage source (VS), sample (S), xyz-positioners (xyz), cavity (C), piezo transducer (PT), acoustic isolation (AI), vacuum chamber (VAC). (b) Sample chip glued to PT on circuit board (PCB) for mounting xyz. Electric signal for PT is provided through connector (CON). (c) Close-up of sample chip region extending the PCB outline showing freely suspended SiN strings.

Measurements of the mechanical properties are carried out using the fiber-integrated interferometer (see figure 5.4(a)) operating with a super luminescent light emitting diode (SLED) at $1310\,\mathrm{nm}$. At this wavelength the cavity mirror coating has only a very poor reflectivity. Thus optomechanics, that requires high finesse cavity modes, does not affect the mechanical properties. SiN does not absorb light at that wavelength so heating of the mechanics can be excluded, too. Interference between light scattered from the SiN strings and the cavity mirrors forms the measurement signal that is sent to a photo detector (D) and measured on a spectrum analyzer (SA). The mechanical amplitude is driven by a piezo transducer (PT) connected to a signal generator (SG). A circuit board (PCB) hosts the PT and the sample chip (S) for easy mounting on the xyz-positioning unit (see figure 5.4(b)). The sample chip is glued with photo resist (red) to the PT such that the processed section with freely suspended SiN strings (close-up in figure 5.4(c)) extends beyond the outline of the PCB. Because of its geometry the interferometer has best sensitivity for the oop modes of the sample (ip modes will no longer be regarded).

In order to increase the mechanical amplitude and the signal for spectral measurements the sample is driven through the PT connected to $-25\,\mathrm{dBm}$ of $20\,\mathrm{MHz}$ bandwidth white noise source of the SG. A Lorentzian fit to the measured spectrum yields the mechanical resonance frequency $\Omega_5/2\pi$ of $2.485\,\mathrm{MHz}$ and a quality factor Q_5 of $0.51\cdot10^6$ for the 5^{th} harmonic figure 5.5(a). However the finite bandwidth of the SA does not resolve the narrow mechanical linewidths properly. Ring-down experiments give better results.

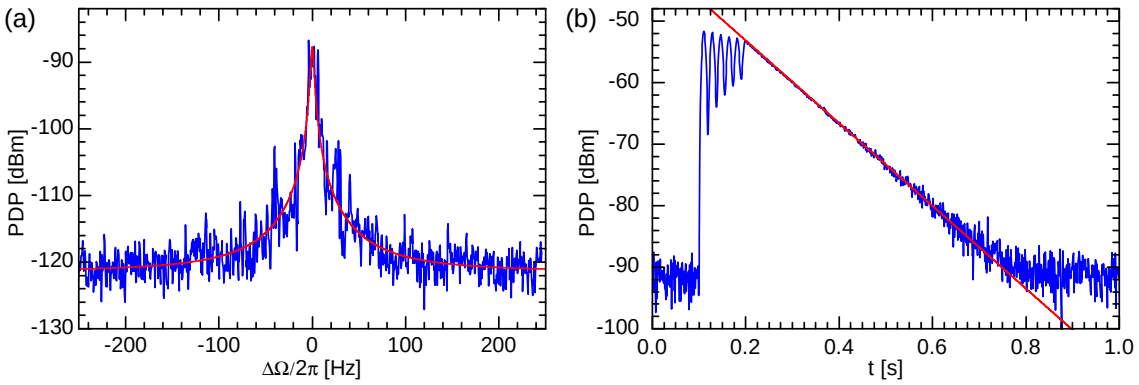

Figure 5.5: (a) Mechanical response measured in the photo detector power spectrum and (b) logarithmic amplitude decay of excited vibration of the 5th harmonic of a $2\,\mu\mathrm{m}$ wide SiN string. Blue traces are measured data points and red curves are fits.

For these the mechanical vibration is excited on resonance frequency with $-40\,\mathrm{dBm}$ RF power from the SG for $100\,\mathrm{ms}$ (in the interval $t = [0.1\,\mathrm{s}, 0.2\,\mathrm{s}]$ in figure 5.5(b)). During the excitation period the resonator is driven at fairly large amplitudes and its natural frequency is nonlinearly shifted to higher values. Thus the natural motion of the nonlinear resonator and the forced motion driven at the original resonance frequency beat and result in the oscillations in amplitude [Nay04, Fit13]. After the drive is switched off (at $200\,\mathrm{ms}$) the amplitude decays to its usual thermal fluctuations. In a common logarithmic plot in dBm units the slope of the free decay b relates to the dissipation rate $\gamma_n = -\ln(10)\,b/10$ and thus to the Q factor according to equation 2.46 as $Q_n = -10\,\Omega_n/(\ln(10)\,b)$ which gives $Q_5 = 0.71 \cdot 10^6$.

Resonance frequencies $\Omega_n/2\pi$ scale linearly with the mode number n up to the 13th harmonic. As shown in figure 5.6(a) measured data (blue) coincides with calculated (red) values and a linear fit yields $\sigma = 863\,\mathrm{MPa}$. This matches well to the results of the simulations, too, and confirms the behavior of a stretched string (equation 2.32). Thus oop mode frequencies are dominated by tensile stress.

Quality factors Q_n for the various modes scatter between 10^5 and 10^6 as shown in figure 5.6(b). Intrinsic damping mechanisms are not the dominant mechanism limiting the Q-factors of these samples. Fabrication residues and particles are considered as the main contributors of mechanical dissipation. Random positions of these defects along the strings are a possible reason for the scattering of the Q-values.

5.3 Optomechanical coupling

Static dispersive and dissipative optomechanical couplings of SiN samples of different geometries are measured in the experiment by sweeping the position z_0 of the sample inside the cavity and measuring the cavity resonance frequency and linewidth. For the dynamic case the overlap of optical mode and mechanical mode shape has to be consid-

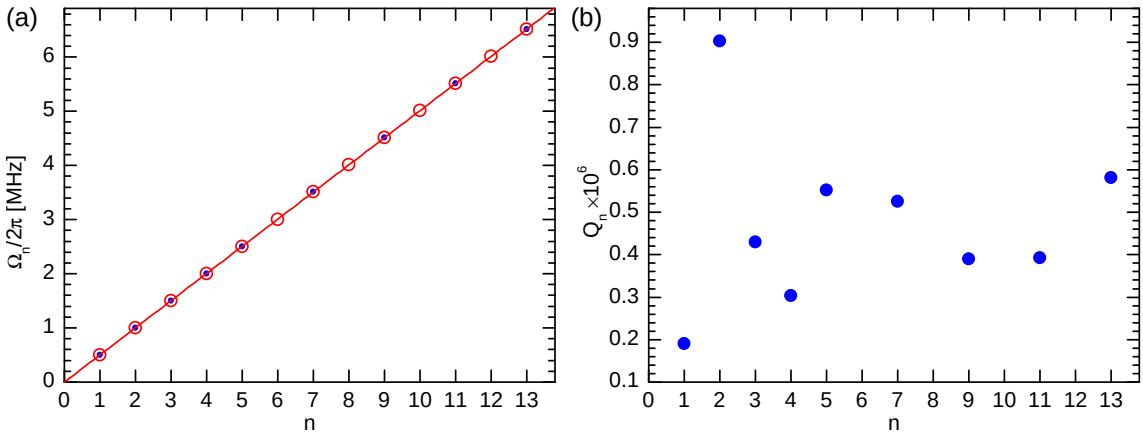

Figure 5.6: (a) Resonance frequencies $\Omega_n/2\pi$ and (b) quality factor values Q_n vs. mode index n. Measured (blue filled dots) and calculated (red open circles) data.

ered (cf. equation 2.52). Because of the geometries of the string ($500\,\mu$m long) and the cavity mode ($7\,\mu$m in diameter) and the optical mode placed at an anti-node of the mechanical deflection, the static couplings can be regarded as good approximation for the dynamic ones up to the 10$^{\text{th}}$ harmonic of the string.

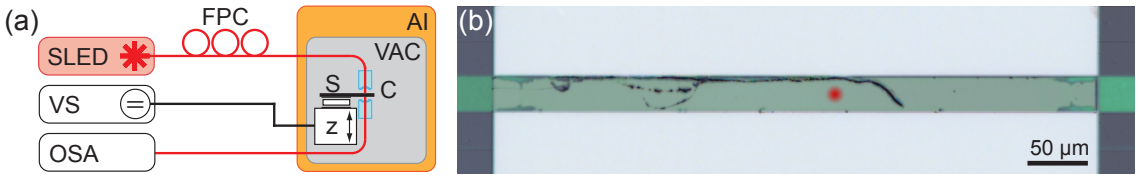

Figure 5.7: (a) Setup for measurement of the optomechanical coupling of a $30\,\mu$m wide silicon nitride sheet inside the cavity. (b) Red spot indicates the position of the cavity mode with respect to the SiN sheet. Super luminescent light emitting diode (SLED), voltage source (VS), spectrometer (OSA), (FPC) fiber polarization control, sample (S), z-positioner (z), cavity (C), acoustic isolation (AI), vacuum chamber (VAC).

In order to measure the optomechanical coupling between the cavity and a $30\,\mu$m wide SiN string the setup as sketched in figure 5.7(a) is used. Instead of a laser, a broad band super luminescent light emitting diode (SLED, EXS7505-8411, *Exalos*) with $750\,$nm center wavelength and $20\,$nm bandwidth is used to pump the cavity (C). The transmitted light is sent to a spectrometer (OSA). The cavity length is kept fixed, but the z-position z_0 of the sample (S) is changed. In xy-plane the sample is positioned such that the cavity mode is centered on the SiN sheet as illustrated in figure 5.7(b).

The transmission spectrum of the cavity (figure 5.8(a)) exhibits 8 dominant and several less bright cavity modes in the range from 380 to $410\,$THz. Bright resonances are attributed to longitudinal TEM_{00} and darker ones to higher order TE modes. Resonance frequencies and amplitudes are periodically modulated with sample position z_0. The resonance at the frequency of the diode laser around $385\,$THz is marked by a white arrow. For this mode, values of the resonant frequencies $\omega_c/2\pi$ and normalized transmissions

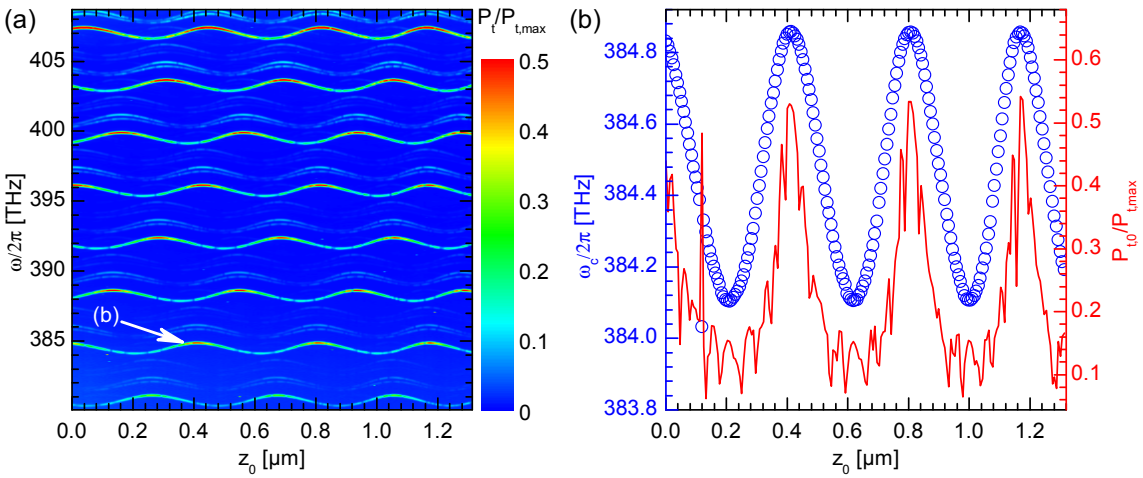

Figure 5.8: (a) Broadband optical transmission spectra of cavity with $30\,\mu\mathrm{m}$ wide silicon nitride sheet inside vs. sample position z_0 along cavity axis. (b) Cavity resonance frequency $\omega_\mathrm{c}/2\pi$ and normalized resonant transmission $P_{\mathrm{t},0}/P_{\mathrm{t,max}}$ of the optical mode indicated by white arrow in (a) vs. z_0.

$P_{\mathrm{t},0}/P_{\mathrm{t,max}}$ are plotted against the sample position z_0 in figure 5.8(b) in blue and red, respectively. Dispersive optomechanical coupling $1/2\pi \cdot \partial\omega_\mathrm{c}/\partial z_0$ extracted from this graph is modulated by the sample position between -6.1 and $7.1\,\mathrm{GHz/nm}$, which is about half of the values obtained by two different numerical simulations based on cavity perturbation (see equation 2.52) and on a transfer matrix approach. This is a reasonable agreement since small tilts of the sample with respect to the cavity mode that are beyond positioning accuracy already have a strong impact on the coupling and are not considered in the simulations. The resolution of the OSA is not sufficient to resolve the narrow linewidth of the cavity thus values for dissipative optomechanical coupling are not accessible.

The dispersive optomechanical coupling benefits from a small cavity mode volume and a large overlap between the cavity mode and the dispersive element. Nevertheless couplings in the regime of $\mathrm{THz/nm}$ achieved by integrated photonic-phononic systems [Cha11] or micro disc resonators [Din11] are out of range for this system. But as compared to state-of-the-art hybrid optomechanical systems, that reach some $\mathrm{MHz/nm}$ [Ane10b, Asp10] the presented value for the dispersive optomechanical coupling is remarkably high as it is the case for another fiber cavity based setup [FJ12].

Acoustic noise and maybe photothermal effects causing fluctuations in the sample position together with this high dispersive coupling complicate further studies of optomechanical effects of the $30\,\mu\mathrm{m}$ wide string inside the cavity. Despite rigid mechanical design of the setup, including passive acoustic isolation and active vibration cancellation using feedback to the sample position shifts in cavity resonance frequency are still too large and too fast to be followed by the cavity stabilization feedback loop. Thus continuous measurements of the mechanics inside the cavity are not possible.

SiN Strings with $2\,\mu\mathrm{m}$ width, that is smaller than the clear aperture of the cavity mode, cause too much optical loss when they are centered in the cavity mode. Thus the cavity

mode does not build up and measurements are not possible. At lateral positions off-center, where the optical disturbance of the string decreases, the cavity signal rises again. Here dispersive optomechanical coupling is too low to be resolved by the spectrometer but it is accessible by means of laser spectroscopy.

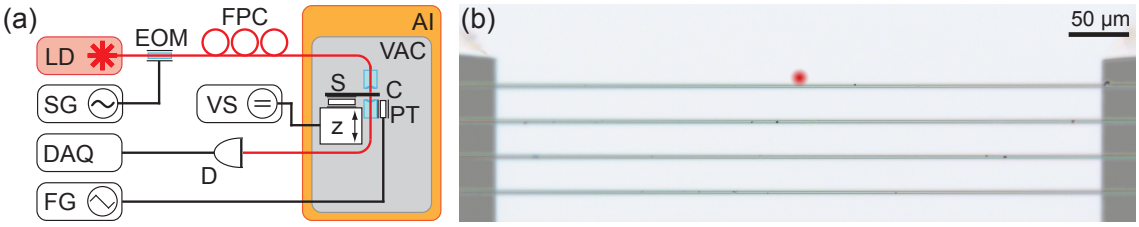

Figure 5.9: (a) Setup for measurement of the optomechanical coupling of a $2\,\mu\mathrm{m}$ wide silicon nitride sheet inside the cavity. (b) Red spot indicates the position of the cavity mode with respect to the SiN sheet. Stabilized diode laser (LD), signal generator (SG), data acquisition (DAQ), function generator (FG), electrooptical phase modulator (EOM), fiber polarization control (FPC), voltage source (VS), photo detector (d), sample (S), z-positioner (z), cavity (C), piezo transducer (PT) acoustic isolation (AI), vacuum chamber (VAC).

In figure 5.9(a) the setup is sketched. Light from a stabilized diode laser (LD) is phase-modulated (EOM) and launched to the cavity (C). Transmitted light is sent to a photo detector (D) and the signal is monitored on an oscilloscope (DAQ). The function generator (FG) triggers the oscilloscope and supplies the piezo transducer (PT) with a triangular voltage that periodically scans the cavity across its resonance. A DC voltage (VS) applied to the z-positioner (z) sets z_0 of the sample (S) inside the cavity. C, S and z are installed in vacuum (VAC) at $10^{-6}\,\mathrm{mbar}$ and in an acoustically isolated environment (AI). The signal generator (SG) drives the EOM at $1\,\mathrm{GHz}$ and modulates sidebands to the laser carrier. A fiber polarization control (FPC) is used to select one of the two cavity polarization modes. A computer (DAQ) controls the measurement and records the data. figure 5.9(b) illustrates a lateral position, where the SiN string has only small overlap with the cavity mode such that sufficient light for measurements is transmitted. The red diffuse spot represents the clear aperture of the cavity mode.

In order to map out the influence of the $2\,\mu\mathrm{m}$ wide SiN strings on the optical mode, cavity scans are recorded for sample positions along the y- and z_0-coordinates. For each scan resonant transmission $P_{\mathrm{t},0}$ and linewidth $\kappa/2\pi$ are evaluated and the resulting maps are plotted in color scale in figure 5.10(a) and (b), respectively. Deep blue in (a) and deep red in (b) mark areas where the signal is too low to extract reliable values for transmission and linewidth. At $y > 31\,\mu\mathrm{m}$ the influence of the string becomes negligible. For decreasing y the overlap of the string with the cavity mode increases. Consequently a drop in $P_{\mathrm{t},0}$ and an increase in $\kappa/2\pi$ are observed. On the range $y = 6 \ldots 20\,\mu\mathrm{m}$, which corresponds to a distance that is twice the diameter of the optical mode, the cavity mode is suppressed for most z_0 positions. Within that range the disturbance is low enough to support cavity modes only when the sample is at positions of a node of the cavity field visible by colored tilted lines in figure 5.10(a) and (b). The tilt of these lines originates from a slight tilt of

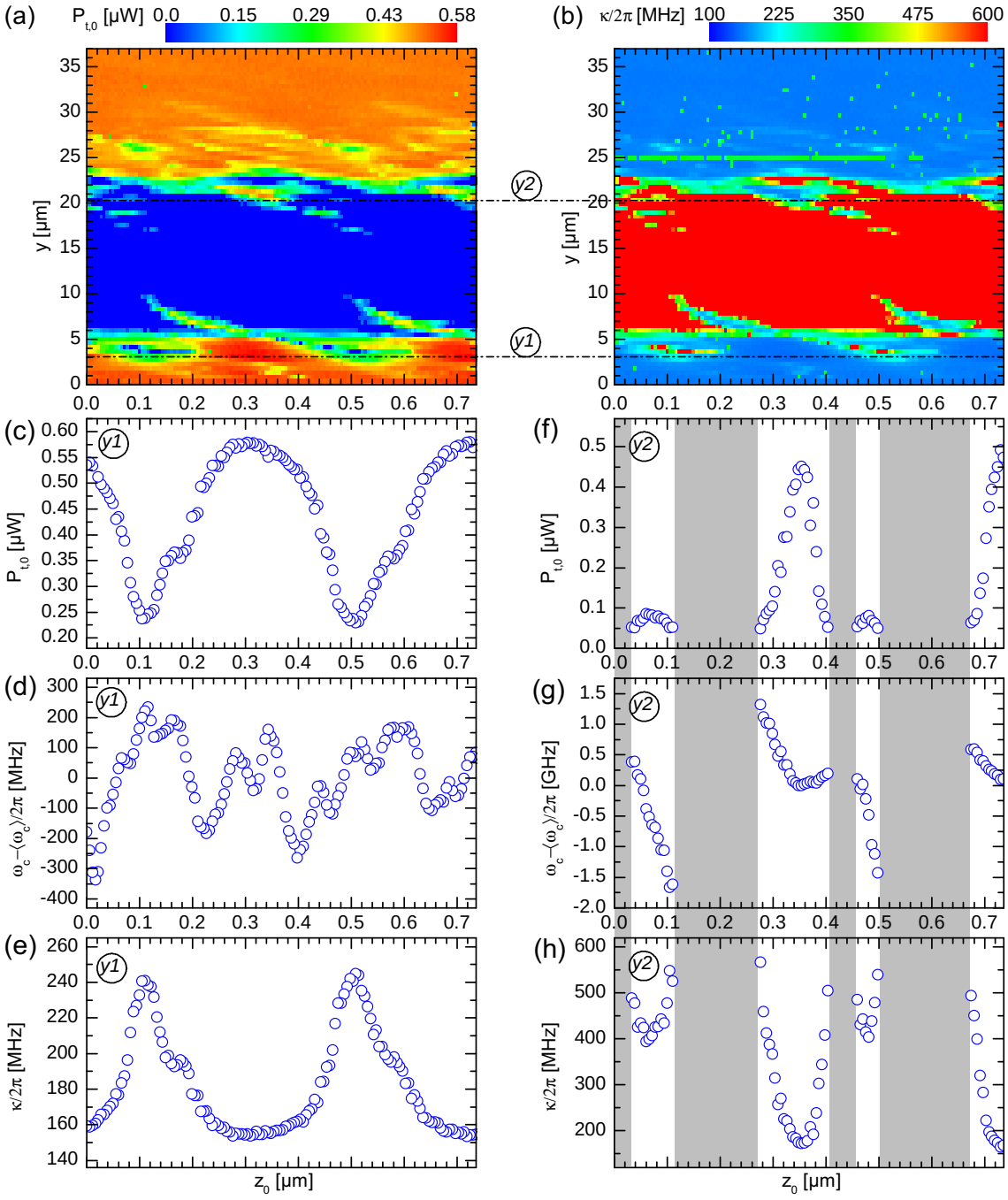

Figure 5.10: (a) Color map of resonant optical transmission $P_{t,0}$ and (b) cavity linewidth $\kappa/2\pi$ with respect to z_0 and y sample position. (c,f) Resonant transmission, (d, g) cavity line shift and (e, h) cavity linewidth vs. z_0 are presented at positions *y1* and *y2*, respectively, as indicated by the dashed lines with labels in (a) and (b). Shaded areas in (f-h) mark z_0 positions where the signal is too low for measurements.

the positioners such that the sample drifts $0.6\,\mu\mathrm{m}$ in z position upon stepping $10\,\mu\mathrm{m}$ along y. For $y < 6\,\mu\mathrm{m}$ $P_{\mathrm{t},0}$ and κ approach the values of the empty cavity. Two y positions with lower (*y1*) and higher (*y2*) optomechanical interaction are selected and the dependence on z_0 of characteristic values of the cavity mode is presented in (c, d, e) and (f, g, h), respectively. Where at *y1* for all z_0 positions signal is available, at *y2* for some z_0 regions (shaded in (f, g, h)) extra cavity losses are too strong. Half-wavelength periodicity is present in $P_{\mathrm{t},0}$ (c, f), the resonance shift $(\omega_\mathrm{c} - \langle\omega_\mathrm{c}\rangle)/2\pi$ (g) and κ (e, h). Lower interaction results in less line shift at *y1* (d) such that the periodicity is hidden in noise. Unlike for ω_c with the $30\,\mu\mathrm{m}$ wide string (figure 5.8(b)) data plots (c) to (h) exhibit asymmetric and non-sinusoidal features. These reproducible features are possibly caused by slight sample-to-cavity misalignment and coupling to further cavity modes even though other modes and their evolutions are not observed in cavity scan data. At *y2* ω_c and κ change on a larger scale and thus dispersive and dissipative optomechanical couplings are larger than at *y1*. Further measurements described in the following sections are performed at these two positions *y1* and *y2*.

SiN strings with decreasing width are desirable to approach the idea of having a sub-wavelength scale, perturbative element with potentially high mechanical quality factor in the cavity. However, structures with lateral dimensions down to $80\,\mathrm{nm}$, as presented in figure 5.2(c) rupture, when illuminated with sufficient laser power ($< 1\,\mathrm{mW}$ in the input) for measurements. Possibly residues from fabrication lead to excessive absorption, heating and consequent failure of the string in the center of the optical mode.

5.4 Mechanics at low optomechanical interaction

The influence of the optical field on the mechanical properties of the sample is studied at position *y1* in figure 5.10(a). Here the overlap of the mechanical element with the optical mode is only very little and for that reason the optomechanical interaction is low. Optomechanical couplings are characterized in detail first.

For varying z_0-position detailed cavity scans are presented in figure 5.11. The cavity transmission P_t is color encoded in plot figure 5.11(a) where scan frequency $(\omega - \langle\omega_\mathrm{c}\rangle)/2\pi$ and sample position z_0 are marked on horizontal and vertical axis, respectively. Exemplarily in plot (b) data points (blue open circles) with fitted curve (red line) of the scan at $z_0 = 0.25\,\mu\mathrm{m}$ is shown (as indicated by the analogously labeled section in (a)). It features five resonances, all spaced by $1\,\mathrm{GHz}$ originating from sidebands modulated on the laser by the EOM for calibration purposes. The fit of the sum of five airy profiles to the data points reveals the resonant transmission $P_{\mathrm{t},0}$, the cavity line shift $(\omega_\mathrm{c} - \langle\omega_\mathrm{c}\rangle)/2\pi$, that is the deviation in frequency of the cavity resonance ω_c from a mean value $\langle\omega_\mathrm{c}\rangle$, and the full-width at half maximum (FWHM) cavity linewidth $\kappa/2\pi$. Results for these evaluations (blue open circles) at each z_0-position are plotted along with fitted Fourier series (red line) obtained by fast Fourier transformations (FFT) in figure 5.11(c)-(e). $P_{\mathrm{t},0}$ (c) and $\kappa/2\pi$ (e) exhibit clear half-wavelength periodicity with respect to z_0 and reverse behavior, that means at

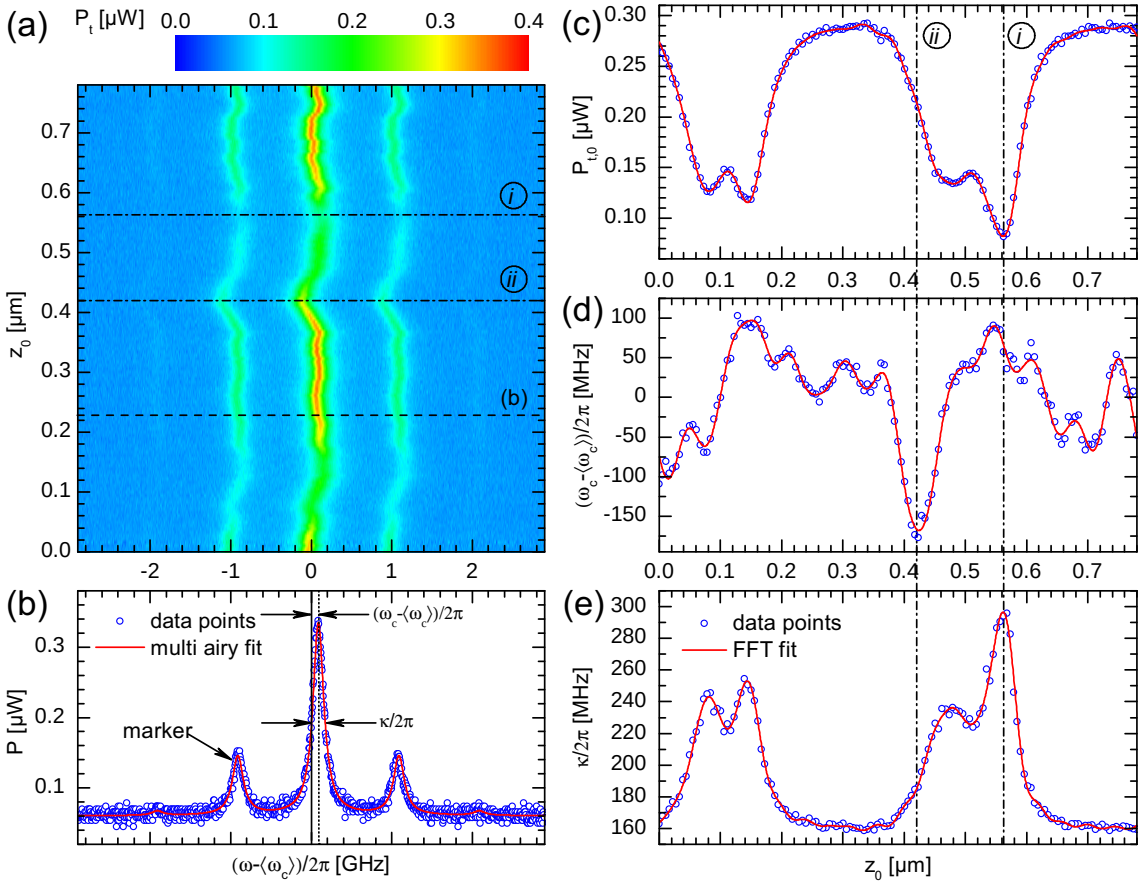

Figure 5.11: (a) Color plot of cavity transmission P_t vs. cavity scan frequency $(\omega - \langle\omega_c\rangle)/2\pi$ and sample position z_0 (at *y1*, refer to figure 5.10(a)). (b) Cavity scan at z_0 as indicated in (a) with data points (blue open circles) and multi Airy fit (red line). (c) Resonant transmission $P_{t,0}$, (d) cavity line shift $(\omega_c - \langle\omega_c\rangle)/2\pi$ and (e) cavity linewidth $\kappa/2\pi$ vs. z_0 as evaluated from scans in (a) (blue open circles) and with fitted Fourier series (red lines).

high $P_{t,0}$ the optical mode dissipation is low and vice-versa. The overall cavity line shift in (d) is less than twice the linewidth of the undisturbed cavity and unlike for $P_{t,0}$ and $\kappa/2\pi$, half-wavelength periodicity is hidden in noise. This noise originates from polarization noise of the scan piezo. Dashed-dotted lines labeled by *i* and *ii* mark positions with either dominant dispersive and dissipative optomechanical coupling, respectively. Their values are summarized in table 5.1.

The mechanical behavior of the SiN string in the cavity mode is influenced not only by optomechanical effects but also by thermal effects. Absorbed cavity photons heat the string locally and contribute to a heat flow from the cavity mode towards the clamps. Consequently a temperature profile forms along the string and upon thermal expansion its tensile stress relaxes. In order to access photothermal heating isolated from optomechanics experimental parameters are chosen to suppress optomechanical influence according to equation 2.86. Dispersive coupling is switched off by operating the cavity on reso-

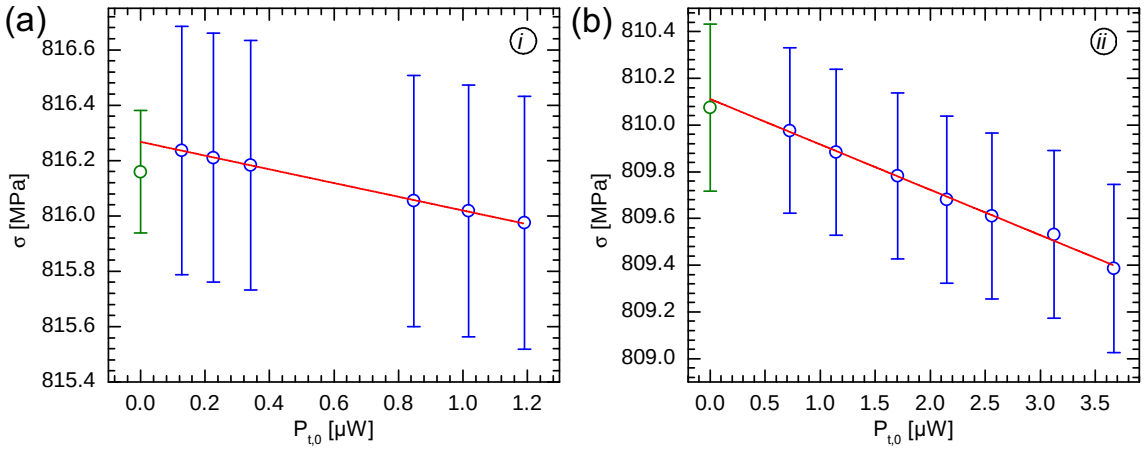

Figure 5.12: Laser power dependence of mechanical stress measured at sample position *i* (a) and *ii* (b) as indicated in figure 5.11(a, c, d, e). Derived stress values (open circles) from measurements with light in the cavity (blue) and reference measurement (green) are plotted with error bars giving the statistical fit errors and a liner fit (red line).

nance at $\Delta = 0$. Unlike dispersive coupling dissipative optomechanical coupling affects the mechanical resonance frequencies even at zero cavity detuning. Therfore the sample is positioned at *i* where dissipative optomechanical coupling is minimal. Recorded spectra of three mechanical modes (first, third and ninth harmonic) reveal a continuous decrease of the mechanical resonance frequencies with increasing laser power. From these modes values for the tensile stress σ are extracted according to equation 2.32 and plotted against cavity transmission $P_{\mathrm{t},0}$ as blue open circles in figure 5.12(a). The green point is reference data measured with light at $1310\,\mathrm{nm}$ where absorption becomes negligible. Error bars denote statistical fit errors of the σ values. A linear fit to the blue points (red lines) reaches the reference point well within the error margin and yields a power dependent stress $\partial\sigma/\partial P_{\mathrm{t}}$ of $-0.25\,\mathrm{MPa}/\mu\mathrm{W}$.
This measurement repeated at *ii* (shown in figure 5.12(b)) results in a weaker power dependence of the stress of $-0.19\,\mathrm{MPa}/\mu\mathrm{W}$. Both optomechanical couplings have opposite sign such that the frequency increase induced by dissipative optomechanical coupling counteracts the photothermal effect. As a result of the higher transmission and less cavity dissipation, the elevated intra-cavity power enhances this effect.

The power dependent stress is modeled starting from Hooke's law,

$$\sigma = \epsilon\, E \tag{5.1}$$

with stress σ, strain ϵ, and Young's module E. Stress σ varies by a variation of the strain ϵ through thermal expansion as

$$\Delta\sigma = \Delta\epsilon\, E = -E\,\alpha_{\mathrm{L}}\,\Delta T, \tag{5.2}$$

where α_L denotes the coefficient of linear thermal expansion. Assuming linearity of Hooke's law, the temperature difference ΔT in equation 5.2 can be substituted by the mean temperature increase along the string. Having the cavity mode at the center of the string and by symmetry considerations it is sufficient to integrate the temperature profile $T(x)$ given in equation 2.50 only over one half of the string $2/l \int_0^{l/2} T(x)\,\mathrm{d}x$ to obtain half of the difference in tensile stress. This yields

$$\sigma = \sigma_0 - \frac{2\,E\,\alpha_\mathrm{L}}{A\,l\,\kappa_\mathrm{T}}\left(\frac{\kappa}{\kappa_0} - 1\right) P_\mathrm{t} \int_0^{l/2} \int_x^{l/2} \mathrm{erf}\left(\sqrt{2}\frac{x'}{w_0}\right) \mathrm{d}x'\,\mathrm{d}x. \tag{5.3}$$

The stress is linear in laser power, and

$$\frac{\partial \sigma}{\partial P_\mathrm{t}} = -\frac{2\,E\,\alpha_\mathrm{L}}{A\,l\,\kappa_\mathrm{T}}\left(\frac{\kappa}{\kappa_0} - 1\right) \int_0^{l/2} \int_x^{l/2} \mathrm{erf}\left(\sqrt{2}\frac{x'}{w_0}\right) \mathrm{d}x'\,\mathrm{d}x. \tag{5.4}$$

From equation 5.4 the contribution of the absorption to the cavity linewidth reads

$$\begin{aligned} \Delta\kappa &= \kappa_0 \frac{A\,l\,\kappa_\mathrm{T}}{2\,E\,\alpha_\mathrm{L}} \frac{\partial \sigma}{\partial P_\mathrm{t}} \left(\int_0^{l/2} \int_x^{l/2} \mathrm{erf}\left(\sqrt{2}\frac{x'}{w_0}\right) \mathrm{d}x'\,\mathrm{d}x \right)^{-1} \\ &= \kappa_0 \frac{2\,A\,l\,\kappa_\mathrm{T}}{E\,\alpha_\mathrm{L}} \frac{\partial \sigma}{\partial P_\mathrm{t}} \left(\frac{l\,w_0}{\sqrt{2\,\pi}} \mathrm{e}^{-\frac{l^2}{2\,w_0^2}} + \frac{l^2 - w_0^2}{2} \mathrm{erf}\left(\frac{l}{\sqrt{2} w_0}\right) \right)^{-1} \end{aligned} \tag{5.5}$$

where $\int_0^b \mathrm{erf}(a\,x)\,\mathrm{d}x = \frac{1}{a\sqrt{\pi}}\left(\mathrm{e}^{-a^2 b^2} - 1\right) + b\,\mathrm{erf}(a\,b)$ is applied.

Thus with thermal expansion $\alpha_\mathrm{L} = 3.2 \cdot 10^{-6}\,\mathrm{K}^{-1}$ [Tie12, Imb14] and thermal conductivity $\kappa_\mathrm{T} = 30\,\mathrm{W\,m^{-1}K^{-1}}$ [Plu00, Imb14] of SiN the effect of cavity linewidth broadening $\Delta\kappa$ is estimated to be less than $1.4\,\mathrm{MHz}$, which is less than $1\,\%$ distortion related to the empty cavity linewidth of $152\,\mathrm{MHz}$ at either position *i* and *ii*. However, the experimentally observed cavity dissipation rates of $309\,\mathrm{MHz}$ at *i* and $210\,\mathrm{MHz}$ at *ii* are $103\,\%$ and $38\,\%$ more than the undisturbed value. Accordingly absorption has only a minor contribution to the optical dissipation here. Lost photons are mostly just scattered out of the cavity mode when the SiN sample is present.

In order to describe the mechanical behavior in the cavity light field more accurately photothermal stress release has to be considered along with dissipative and dispersive interaction discussed in chapter 2.2. Therefore a power dependent frequency shift

$$\frac{\mathrm{d}\Omega_n}{\mathrm{d}P_\mathrm{t}} P_\mathrm{t} = \frac{1}{2} \frac{\Omega_n}{\sigma(P_\mathrm{t})} \frac{\partial \sigma}{\partial P_\mathrm{t}} P_\mathrm{t} \tag{5.6}$$

derived from equation 2.32 with power dependent stress $\sigma(P_\mathrm{t})$ is added to the equation 2.86

$$\Omega_{\mathrm{eff},n} = \left(\Omega_n^2 - 2\,C\,\frac{\partial \omega_\mathrm{c}}{\partial z}\,\frac{\frac{\partial \omega_\mathrm{c}}{\partial z}\,\Delta\left(\kappa^2/4 - \Omega_n^2 + \Delta^2\right) + \frac{\partial \kappa}{\partial z}\,\kappa/4\left(\kappa^2/4 + \Omega_n^2 + \Delta^2\right)}{\left(\kappa^2/4 + (\Omega_n - \Delta)^2\right)\left(\kappa^2/4 + (\Omega_n + \Delta)^2\right)} \right)^{\frac{1}{2}} + \frac{1}{2}\,\frac{\Omega_n}{\sigma(P_\mathrm{t})}\,\frac{\partial \sigma}{\partial P_\mathrm{t}}\,P_\mathrm{t} \tag{5.7}$$

where higher order dispersive coupling is neglected. The model in equation 2.87 predicts a change of the mechanical dissipation γ with respect to the detuning, too. An estimation of the change in dissipation rate for present experimental parameters results $\Delta\gamma_\mathrm{eff} \approx 0.8\,\mathrm{Hz}$ at position *i*. Unfortunately large scatter in measured values does not allow a systematic analysis of γ_eff. The narrow linewidth and long acquisition times complicate the measurement. Fluctuations in the intensity of the light sent to the photo detector cause fluctuations in the measured ring-down traces and thus increase the error of the fitted dissipation rates.

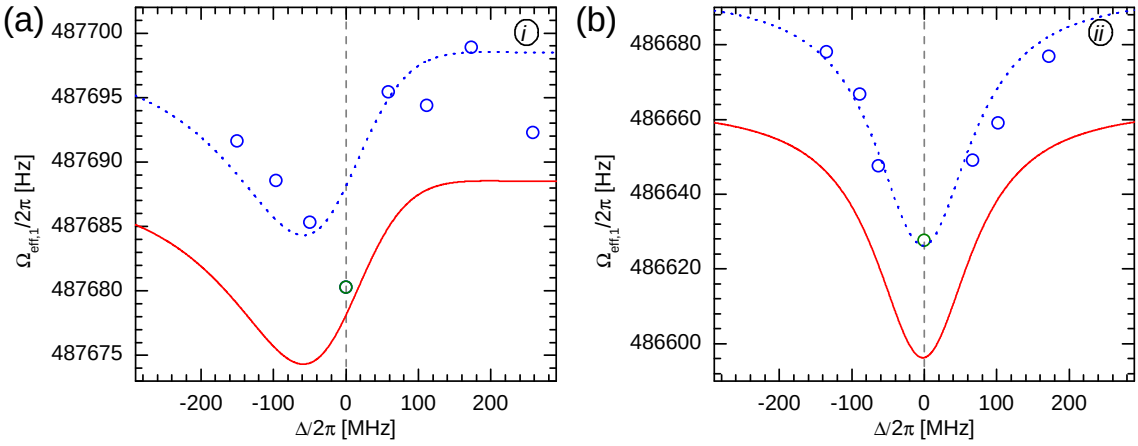

Figure 5.13: Effective Mechanical resonance frequencies of fundamental mode $\Omega_{\mathrm{eff},1}/2\pi$ vs. cavity detuning Δ measured at two sample position *i* (a) and *ii* (b) as indicated in figure 5.11(a, c, d, e). Blue and green open circles represent data points from two sets of measurements, red (blue dashed) lines are calculations including photothermal, dispersive and dissipative optomechanical effects with no free parameters (just the offset frequency adjusted).

The resonance frequency of a mechanical mode exhibits a clear dependence on the cavity detuning Δ. Figure 5.13 displays measured frequencies of the fundamental mode of a SiN string (blue open circles, green circles at $\Delta = 0$ are taken for completeness from the measurement set shown in figure 5.12). Thereby the symmetry of the data points with respect to Δ differs at positions *i* (a) and *ii* (b). Where at *ii* the points follow a dip almost symmetrically centered at zero detuning, data points at *i* are arranged asymmetrically. They rise with negative detuning values and are highest for positive Δ. Comparing the model equation 5.7 which includes photothermal, dispersive and dissipative optomechanical effects with the measured data shows good agreement. Red curves in figure 5.13 are plotted from equation 5.7 where all necessary input parameters are known by either literature or independent measurements and have been mentioned in the text above. The

dotted blue curve is like the red one with no free parameters but just shifted vertically in mechanical offset frequency to illustrate the agreement of the model with the data. Photothermal heating of the SiN string reduces the resonance frequency with the intracavity power, and thus frequency is lowest at $\Delta = 0$ and rises symmetrically with increasing absolute detuning. Dispersive optomechanical coupling that is dominantly present at *i* creates an antisymmetric curve shape of $\Omega_{\mathrm{eff},1}/2\pi$ with a minimum at negative and a maximum at positive Δ values. However it is superimposed by photothermal frequency shift that distorts this symmetry as seen in figure 5.13(a). Photothermal and dissipative optomechanical frequency shifts are symmetric with respect to the detuning and so is their superposition as seen by the line shape in figure 5.13(b).

Table 5.1: Values for cavity linewidth, stress release, dispersive and dissipative optomechanical coupling for various experimental sample positions.

y position			*y1*			*y2*	
z position			*i*	*ii*	*iii*	*iv*	*v*
relative z-coordinate	z_0	$[\mu\mathrm{m}]$	0.58	0.42	0.11	0.18	0.21
cavity linewidth	$\frac{\kappa}{2\pi}$	$[\mathrm{MHz}]$	309	210	331	235	348
stress release	$\frac{\partial\sigma}{\partial P_\mathrm{t}}$	$\left[\frac{\mathrm{MPa}}{\mu\mathrm{W}}\right]$	-0.25	-0.19	-1.4	-2.8	-5.5
dispersive coupling	$\frac{1}{2\pi}\frac{\partial\omega_\mathrm{c}}{\partial z_0}$	$\left[\frac{\mathrm{MHz}}{\mathrm{nm}}\right]$	-2.6	-0.15	13.8	11.2	12.5
dissipative coupling	$\frac{1}{2\pi}\frac{\partial\kappa}{\partial z_0}$	$\left[\frac{\mathrm{MHz}}{\mathrm{nm}}\right]$	-0.36	1.1	-3.3	2.2	5.7

5.5 Mechanics at high optomechanical interaction

Compared to the overall travel in y-direction to move the SiN string across the sensitive area of the cavity, the values for optomechanical couplings change dramatically on a rather short distance. Because of symmetry of the cavity mode and the SiN string high optomechanical interaction as observed at position *y2* in figure 5.10 occurs only 3 to $4\,\mu\mathrm{m}$ away from *y1*, too. The overlap of the mechanical element with the optical mode is only slightly bigger at sample position *y2* compared to *y1*, but optomechanical couplings increase by factors.

Having the sample placed at *y2* cavity scans for different z_0-positions are performed and presented in the color plot figure 5.14(a). Analog to figure 5.11(a) this plot shows the evolution of the cavity resonance with the sample position z_0. Besides three fold bright traces that again stem from the laser carrier frequency and modulated side bands no further cavity modes are observed in the measurement range. Thus optical modal interaction

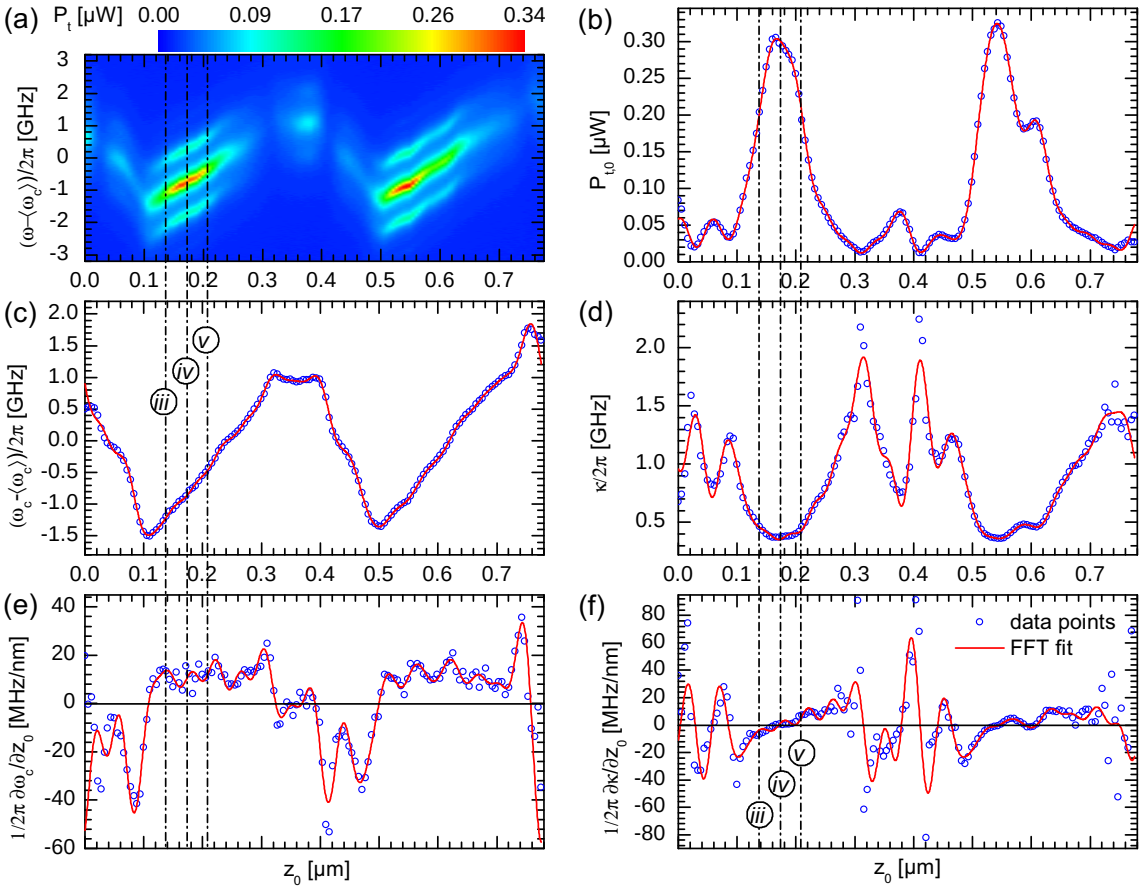

Figure 5.14: (a) Color plot of cavity transmission P_t vs. cavity scan frequency $(\omega - \langle\omega_\mathrm{c}\rangle)/2\pi$ and sample position z_0 (at *y2*, refer to figure 5.10(a)). (b) Resonant transmission $P_{\mathrm{t},0}$, (c) cavity line shift $(\omega_\mathrm{c} - \langle\omega_\mathrm{c}\rangle)/2\pi$ and (d) cavity linewidth $\kappa/2\pi$ vs. z_0 evaluated from scans in (a) (blue open circles) and with fitted Fourier series (red lines). (e) Dispersive and (f) dissipative optomechanical couplings $1/2\pi\,\partial\omega_\mathrm{c}/\partial z_0$ and $1/2\pi\,\partial\kappa/\partial z_0$ derived from (c) and (d).

and coupling is assumed to be of minor importance. The shift in cavity resonance frequency and linewidth is very obvious here. Evaluated resonant transmission $P_{\mathrm{t},0}$, cavity line shift $(\omega_\mathrm{c} - \langle\omega_\mathrm{c}\rangle)/2\pi$ and cavity dissipation $\kappa/2\pi$ data are displayed versus z_0 along (b), (c), and (d) as blue open circles. Dispersive and dissipative optomechanical couplings $1/2\pi\,\partial\omega_\mathrm{c}/\partial z_0$ and $1/2\pi\,\partial\kappa/\partial z_0$, shown in (e) and (f) are derived from values of cavity line shift and dissipation. Fourier series are fitted to the data points (red curves). The cavity features two dominant transmission regions from $0.12\,\mu\mathrm{m}$ to $0.22\,\mu\mathrm{m}$ and from $0.51\,\mu\mathrm{m}$ to $0.63\,\mu\mathrm{m}$. In between the transmission has two local maxima and it is almost completely suppressed at certain z_0-position (e.g. around $0.03\,\mu\mathrm{m}$, $0.31\,\mu\mathrm{m}$, $0.41\,\mu\mathrm{m}$ and $0.75\,\mu\mathrm{m}$). The cavity line is shifted for more than $3\,\mathrm{GHz}$ in total and presents a plateau from $0.32\,\mu\mathrm{m}$ to $0.4\,\mu\mathrm{m}$ and nearly linear sections with negative (from $0\,\mu\mathrm{m}$ to $0.11\,\mu\mathrm{m}$ and from $0.4\,\mu\mathrm{m}$ to $0.5\,\mu\mathrm{m}$) and positive slopes (from $0.11\,\mu\mathrm{m}$ to $0.32\,\mu\mathrm{m}$ and from $0.5\,\mu\mathrm{m}$ to $0.76\,\mu\mathrm{m}$). The cavity dissipation qualitatively reflects the inverse transmission curve. Minimal val-

ues are still more than twice the linewidth of the empty cavity and dissipation ranges from roughly $0.4\,\mathrm{GHz}$ up to $2.5\,\mathrm{GHz}$. All three quantities shown in (b), (c) and (d) exhibit half wavelength periodicity with respect to z_0. Especially cavity line shift and dissipation cover a range that is one order of magnitude more compared to values obtained at position *y1* which results in absolute extremal values for dispersive and dissipative optomechanical coupling of more than $50\,\mathrm{MHz/nm}$. Dashed-dotted lines labeled by *iii*, *iv* and *v* mark positions with negative, almost zero and positive dissipative coupling where dispersive coupling is nearly constant and absolutely larger. Their values are noted in table 5.1.

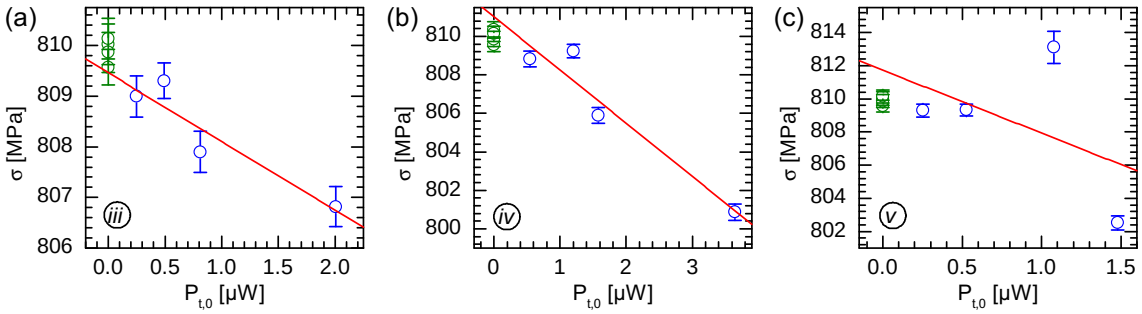

Figure 5.15: Mechanical stress relaxation with increasing laser power at positions *iii* (a), *iv* (b) and *v* (c) as indicated in figure 5.14. Derived stress values (open circles) from measurements with light in the cavity (blue) and reference measurement (green) are plotted with error bars giving the statistical fit errors and a liner fit (red line).

Analog to the previously explained method the dependence of stress on laser power is measured at position *y2*, *iii* through *v* and presented in figure 5.15. The large scatter of the data points stems from slight variations in sample position for different laser power values which implicates slightly varying optomechanical couplings and absorption rates. Absolute power dependent stress release values increase from $-1.4\,\mathrm{MPa}/\mu\mathrm{W}$ to $-5.5\,\mathrm{MPa}/\mu\mathrm{W}$ as the sample is moved from *iii* to *v*. This is in agreement with equation 5.7 and the experimental finding at *y1* where optomechanical couplings with opposing sign counteract the photothermal frequency down-shift of the mechanics. For comparison these values are summarized in Table table 5.1. At *iv* dissipative optomechanical coupling is lowest and thus the stress release of $-2.8\,\mathrm{MPa}/\mu\mathrm{W}$ is considered to be close to the natural value mostly free of optomechanical effects. The cavity linewidth is larger by $82\,\mathrm{MHz}$ at position *iv* compared to the case of an empty cavity. That means the SiN string adds $54\,\%$ to the optical dissipation. According to equation 5.5 heating of the string significantly contributes to the cavity linewidth of $21\,\mathrm{MHz}$ which is more than a quarter of the total increase. But still the bigger part of the extra dissipation, namely the other three quarters, originates from photons just scattered out of the cavity mode.

The analysis of the experimental data of the resonance frequencies as a function of detuning does not reveal a systematic behavior according to the extended model of equation 5.7 as it was the case in section 5.4 when the sample is at any position *iii*, *iv* or *v*. A reason might be drifts in sample position that could not be compensated for by feedback during each measurement set. Since a small change in position already has strong

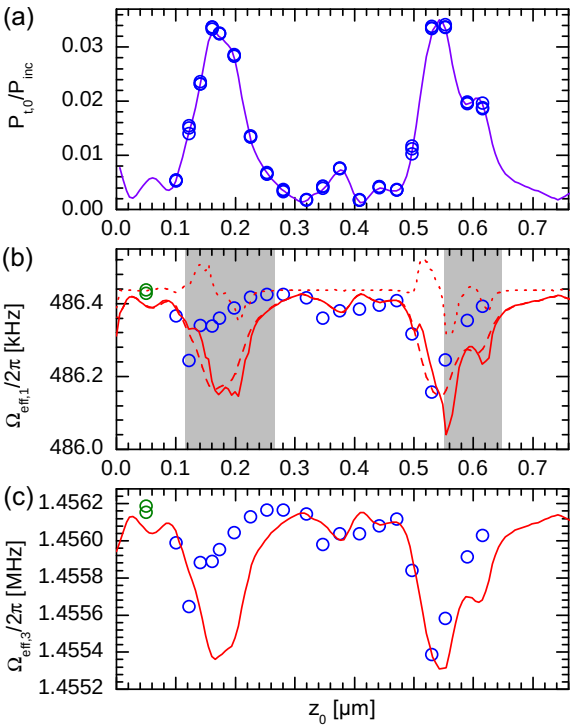

Figure 5.16: Dependence on z_0 position of normalized cavity transmission $P_{t,0}/P_{inc}$ (a) and effective mechanical resonance frequencies $\Omega_{eff,1}/2\pi$ (b) and $\Omega_{eff,3}/2\pi$ (c) measured at zero cavity detuning. (a) Blue open circles represent values recorded during measurement of the mechanics is performed, the purple trace is a continuous measurement of the transmission. Open circles in (b) and (c) are resonance frequencies fitted to measured spectra with light in the cavity (blue) and for reference measurements (green). Red traces in (b) and (c) are frequencies calculated with the model including dispersive and dissipative optomechanical couplings (dotted, only in (b)), photothermal stress relaxation (dashed, only in (b)) and all three contributions (solid line) based on experimental parameters.

influence on the optomechanical couplings resonance frequencies are altered in an uncontrolled way.

For further tests of the model with less requirements on the stability of the sample position spectra of the first and third mechanical modes are recorded for various z_0-positions while the cavity detuning ($\Delta = 0$) and the input laser power are kept constant. The profile of the resonant cavity transmission (purple curve in figure 5.16(a) displays the transmission normalized to the incident laser power) has the same shape as the one shown in figure 5.14(b). Thus it is assumed that the positioning of the sample in y-direction is quite comparable. Effective resonance frequencies $\Omega_{eff,1}/2\pi$ and $\Omega_{eff,3}/2\pi$ (blue open circles) of the first and third mechanical modes are plotted vs. z_0-position in figure 5.16(b) and (c). Frequencies of the two modes are decreased with respect to the reference values (green open circles, again measured at $1310\,\mathrm{nm}$) over the full measurement range. Two pronounced dips (at $z_0 = 0.12\,\mu\mathrm{m}$ and $z_0 = 0.52\,\mu\mathrm{m}$) reflect the half wavelength periodicity that is present in the transmission values (blue open circles in figure 5.16(a)), too. Three curves modeling $\Omega_{eff,1}/2\pi$ by only optomechanical effects (dotted, equation 2.86), photothermal effects (dashed) and the sum of both (solid, equation 5.7) are plotted to the measured data in figure 5.16(b). Along with measured data of the third mode $\Omega_{eff,3}/2\pi$ only the curve of the full model (solid red line, equation 5.7) is plotted in figure 5.16(c). For the modeling all relevant input values are known or extracted from measurements analog to figure 5.14 and fed into respective equations. In that sense the models applied to the two mechanical modes $\Omega_{eff,1}/2\pi$ and $\Omega_{eff,3}/2\pi$ are fed with identical input parameters that relate to the optical mode and the optomechanical couplings. Like these input parame-

ters optomechanical coupling, cavity transmission and linewidth all versions of the model feature half wavelength periodicity with z_0. Dispersive and dissipative optomechanical couplings only result in a bidirectional shift of the mechanical frequency above and below reference as indicated by the dotted red curve in figure 5.16(b). Modeled photothermal effects reduce the resonance frequency (dashed red curve), especially where the cavity transmission is high. The photothermal effect dominates over optomechanical effects. This is more clear for the third than for the first mode because photothermal and optomechanical effects scale differently with the mechanical resonance frequency. In sum the resonance frequencies drop below the respective references for all positions z_0 (solid red curve follows equation 5.7). The dips in resonance frequencies occur at positions of high cavity transmission where the model predicts a pronounced decrease, too, mainly because of photothermal effects. The magnitude of the shift around $0.2\,\mathrm{kHz}$ for the fundamental mode is comparable to the experimental values. But especially in the gray shaded regions in figure 5.16(b) the models fail to describe the exact mechanical frequency behavior. Here the measured values are higher than expected by the model and minimal values of measured data are shifted to lower z_0-positions compared to the predictions of the model. Interestingly the gray regions are spaced at half wavelength in z_0-positions. Generation of complicated spacial cavity mode patterns at those positions would affect the interaction characteristics and lead to frequencies deviating from the modeled predictions. However, the underlying mechanism remains unclear and requires further investigations.

5.6 Summary and outlook

Doubly-clamped mechanical resonators are processed starting from $50\,\mathrm{nm}$ thick silicon nitride membranes. The resonators are freely suspended across a $0.5\,\mathrm{mm}$ wide gap in the substrate as required for the use inside the cavity. They are fabricated in different widths between $80\,\mathrm{nm}$ and $30\,\mu\mathrm{m}$. The fundamental modes have resonance frequencies around half a megahertz and because of the dominating tensile stress higher harmonics are separated in frequency by the same amount. Quality factors are found between 10^5 and 10^6 for different modes. Whereas narrow structures with widths below $2\,\mu\mathrm{m}$ disrupted when exposed to the cavity within seconds the wider ones showed no degradation. Cavity transmission, resonance frequency and linewidth are affected by the presence of the mechanical element in the optical mode and half wavelength periodicity is observed for all values with respect to z-position (along the cavity axis) of the sample. Dispersive and dissipative optomechanical coupling between the cavity mode and the mechanical element are tunable through y- and z-position in a wide range of $\pm 6\,\mathrm{GHz/nm}$. Not only optomechanical couplings are identified to influence the mechanical element but also absorption of light and the resulting thermal expansion of the resonator reduce the resonance frequency. In the presented experimental situations absorption contributes up to $25\,\%$ to the extra cavity losses. The model proposed in reference [Bia11] is extended by a term expressing photothermal expansion and thus found to apply qualitatively to the measured frequency shift of the fundamental mechanical mode for moderate optomechanical cou-

plings. However at higher optomechanical couplings and at increased absorption rates this model only partially describes the measured features.

Photothermal heating seems to be a limiting factor for the measurements. In order to gain better understanding, further experimental effort is required. Thus with more samples statistical variation of the original SiN membranes can be observed and the best candidates can be selected. Additional influence of the fabrication method like surface roughness and residues can be identified. This will help to improve the sample processing and quality, and possibly very thin strings will be available for the cavity. Measurements at very high optomechanical coupling with $30\,\mu\mathrm{m}$ wide strings is hindered by residual acoustic vibration and possibly photothermal effects. Even though heavy noise isolation improved the situation a lot the setup is still to twitchy in order to perform extremely stable measurements. To overcome photothermal effects in SiN modifications of the setup to operate at $1064\,\mathrm{nm}$ would be beneficial since SiN exhibits almost negligible absorption at longer wavelengths compared to $780\,\mathrm{nm}$ [San10].

The method presented to pattern the SiN membrane gives large freedom of design for the samples which keeps large potential for fabrication of structures with tailored mechanical properties. This way not only flexural but also torsional resonators [Kim13] can be prepared for measurements inside the cavity. Sample geometries with two or more close-by mechanical resonators can be realized and subjected to the cavity field. These resonators prospectively couple through the optical mode which might initiate entanglement of their motional states [Har08].
Because of their built-in stress as processed SiN membranes provide a robust platform to serve as a holder for various samples to be introduced into the narrow gap of a fiber cavity beyond optomechanical purposes. This way nanoparticles can be attached to the SiN bridges and subjected to the cavity field. Thus the interaction of e.g. nanodiamonds with defect centers [Tis11] and rare earth doped nanocrystals [Kol12] with the cavity field can be studied. A promising combination of SiN bridges with CNT is shown in the outlook (chapter 6) of this work.

Chapter 6

Conclusion and outlook

This thesis presents results of experiments on two structurally different nanomechanical resonators formed by either carbon nanotubes (CNTs) or silicon nitride (SiN) strings measured in a miniature optical cavity. Inspired by the proposal of Favero and Karraï [Fav08] this project advances the study of miniaturization of mechanical resonators for optomechanical experiments. Theoretical framework including descriptions of the optical and mechanical subsystems, optomechanical couplings and useful mathematical formalisms is presented in chapter 2. Suitable optomechanical models are oulined in this chapter.

An optical experiment is developed involving a high-finesse fiber-based microscale Fabry-Pérot cavity that is used for ultra-sensitive readout of the motion of the nanomechanical resonators. Descriptions and specifications of the setup along with the detailed assembly procedure and characterization of the cavity are presented in chapter 3.

In order to extend the principles of high-sensitivity optomechanical detection to molecular scale nanomechanical systems carbon nanotube samples are produced as described in chapter 4. Suitable for the use inside the cavity, CNTs grown in a bottom-up process are suspended across gaps in specialy fabricated thin silicon substrates. The optical detection of the Brownian motion of the fundamental mode of the sub-wavelength sized nanotube is demonstrated. A full vibrational spectrum of the carbon nanotube is obtained optically and confirmed by characterization of the same device in a scanning electron microscope. Cavity perturbation calculations suggest that the optical readout of this nanoscopic device is enabled through dispersive interaction with the cavity mode.

In a top-down fabrication procedure described in chapter 5 suspended nanomechanical devices made from silicon nitride material are developed for measurements inside the cavity. In contrast to CNTs these devices reproducibly allow a large freedom in design. Hence SiN resonators with widths in a range from $80\,\mathrm{nm}$ to $30\,\mu\mathrm{m}$ have been used in this work. Because of their built-in stress, these resonators exhibit high intrinsic quality factors beyond 10^5. In the cavity SiN resonators exhibit dispersive and dissipative optomechanical coupling. Couplings are mapped out in the optical mode and show a strong dependence on the position of the string. Small cavity mode volume and dominantly dispersive character of SiN enable couplings up to $\pm 6\,\mathrm{GHz/nm}$ for $30\,\mu\mathrm{m}$ wide strings.

Strings introduce significant loss by scattering photons when their side faces overlap with the optical mode. This is implicitly the case for resonators of widths less than the clear aperture of the cavity mode. At moderate optomechanical couplings the interaction with the cavity mode yields in shifts of the mechanical resonance frequencies that fit qualitatively to a model presented in reference [Bia11]. Dispersive and dissipative optomechanical couplings are included, however the model had to be extended by a frequency shift term that is related to photoabsorption induced thermal stress release in SiN.

Further investigations are required to gain more insight on the factors influencing photoabsorption and the mechanical quality. Subject of these investigations could be surface roughness, residues from fabrication and intrinsic factors [Jöc11] with large intersample variance. Studies with larger number of samples are required in order to build up a statistical basis to distinguish between these contributions. This possibly helps to improve fabrication process and yield, to realize very thin strings. In addition it may lead to a better control of the optical and mechanical performance of samples. To overcome photothermal effects in SiN modifications of the setup operation at $1064\,\mathrm{nm}$ would be required. As mentioned in reference [San10] SiN exhibits almost negligible absorption at longer wavelengths compared to $780\,\mathrm{nm}$.
The method presented to pattern the SiN membrane gives large freedom of design for the samples, including large potential for fabrication of structures with tailored mechanical properties. This way not only flexural but also torsional resonators [Kim13] can be prepared for measurements inside the cavity. Sample geometries with two SiN strings, that are separated by $12\,\mu\mathrm{m}$ to $14\,\mu\mathrm{m}$ according to figure 3.15(b) can be realized. Subjecting those strings simultaneously to the cavity mode enables coupling through the optical field and may prospectively initiate entanglement of their motional states [Har08].

Because of their built-in stress as processed SiN membranes provide a robust platform to serve as holder for various samples to be introduced into the narrow gap of a fiber cavity. In consequence of the work on CNTs, SiN membrane structures are tested as more reliable sample holders for doubly-clamped freely suspended carbon nanotubes. Results of a conceptual study demonstrate the compatibility of processed SiN membranes with the deposition of CNTs. Bundles of CNTs are found to bridge the $20\,\mu\mathrm{m}$ wide gap between two adjacent SiN beams as shown in figure 6.1. Those samples imply a significant improvement in terms of yield, ease of handling and they provide a spledid base for advanced investigations of CNTs within the cavity. A clever choice of cavity modes could enable cavity-enhanced Raman spectroscopy and optomechanical experiments with Raman modes of the nanotube independent of substrate effects.

From a technical perspective, the setup holds potential for further improvements. A more rigid revision of the hardware construction hosting cavity and sample positioning assembly is necessary to reduce vibrations and guarantee stable operation condition. Especially when wide membrane structures with the largest optomechanical coupling are used this modification will facilitate high-resolution measurements. Additional active position control and stabilization in z-direction can be implemented by an extra fiber, that forms a low finesse interferometer in combination with the surface of the sample chip.

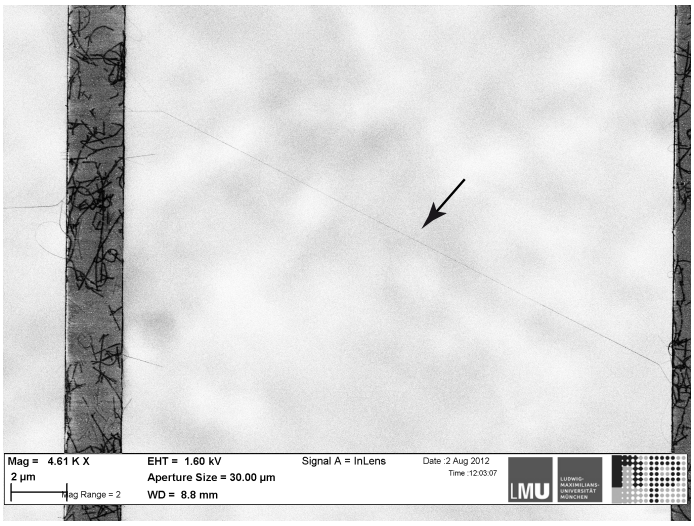

Figure 6.1: SEM image of a carbon nanotube bundle (faint, black diagonal line from top left to bottom right where the black arrow points at) freely suspended across a $20\,\mu\mathrm{m}$ wide gap between silicon nitride beams (vertical, dark gray).

Temperature control of the sample, either locally employing simple Peltier heating and cooling or in a grander scale using cryogenic environment, will enable complementary measurements for the Brownian nature of the motion of the resonators and for further studies of the photothermal effects in SiN. Especially for advanced optomechanics experiments cryogenic cooling will be a necessity.
At longer wavelength not only photothermal effects of the nanoresonator will be reduced but also roughness-induced scattering which scales quadratically with the inverse wavelength. As such less scattering off the nanoresonator is expected. Moreover cavity mirrors exhibit enhanced performance via decreased scattering through roughness at the surface and by lesser absorbtion in the coatings. Together these improvements outweigh the loss in vibrational sensitivity. On top of that, at telecom wavelengths fiber optic components are available more cheaply and in larger diversity than at other wavelengths, providing much more flexibility for the experimental setup.
A reduction of the diameter of the mirror-ended fibers also increases clearance in the cavity. A lapping technique of tapering mirrored fiber ends as recently established in the group of David Hunger could be applied prior to cavity assembly. This way shorter resonators with higher frequency at the fundamental mode and lower effective mass can be used and thus the sensitivity for higher mechanical frequencies will be increased.
In order to increase the sensitivity of the overall setup, laser and detection noise budgeting has to be carried out. Implementing a polarization-sensitive balanced detection scheme will at a minimum help to cancel out technical noise.
The procedure presented here enables the design and assembly of fiber-based optical cavities covering a wide range of parameters. This makes it attractive for various samples

and physical systems like carbon nanotubes, nanowires, defect centers in nanocrystals, and two dimensional materials. According to the specific experimental requirements the setup can be extended through optical fiber connections to methods like cavity-enhanced Raman spectroscopy and time-resolved experiments. Combining multi-color excitation with higher order cavity modes facilitates measurements similar to the STED technique. These high finesse and small mode volume cavities along with the setup in its completeness provide a rare combination of technical advantages begging application in studies well above and beyond the optomechanical purposes presented in this work.

Appendix A

Experimental material

A.1 Cavity assembly material

Home built parts used for fiber coating and cavity assembly as mentioned in chapter 3.1.1 are illustrated in figure A.1 and figure A.2.

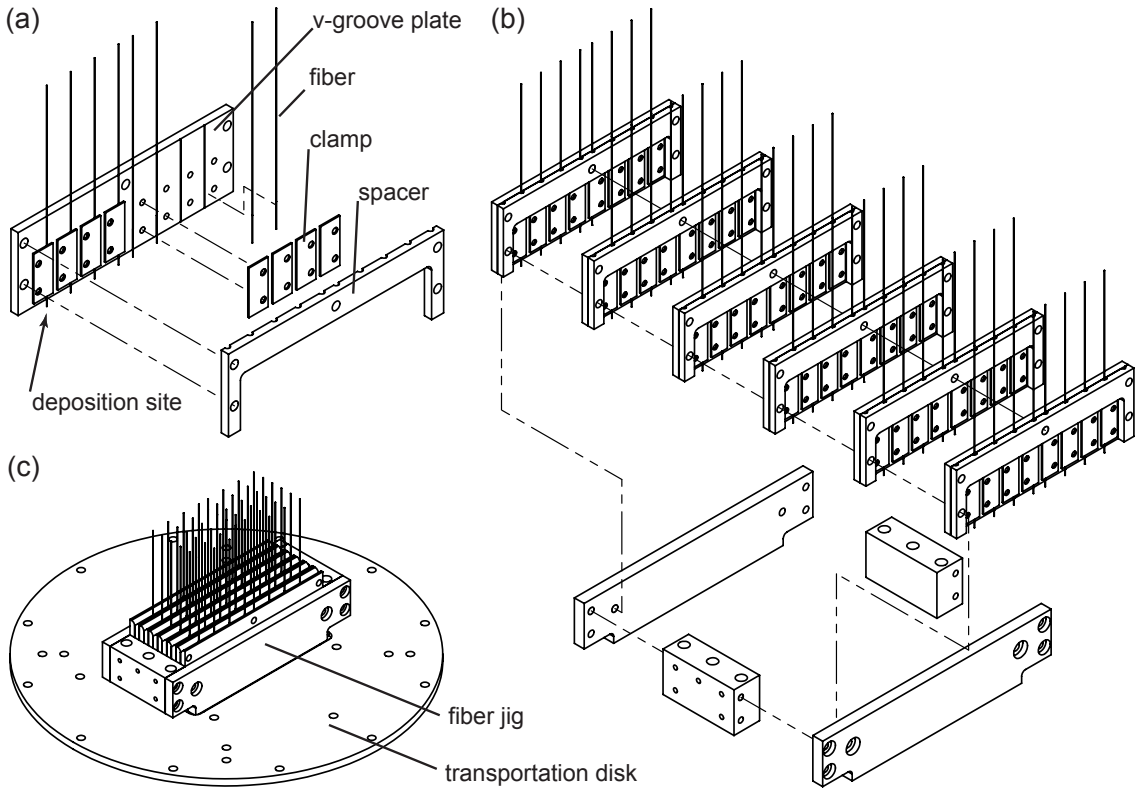

Figure A.1: Drawings of the tool to mount 48 fibers for shipping and for deposition of the Bragg mirror coating at ATF.

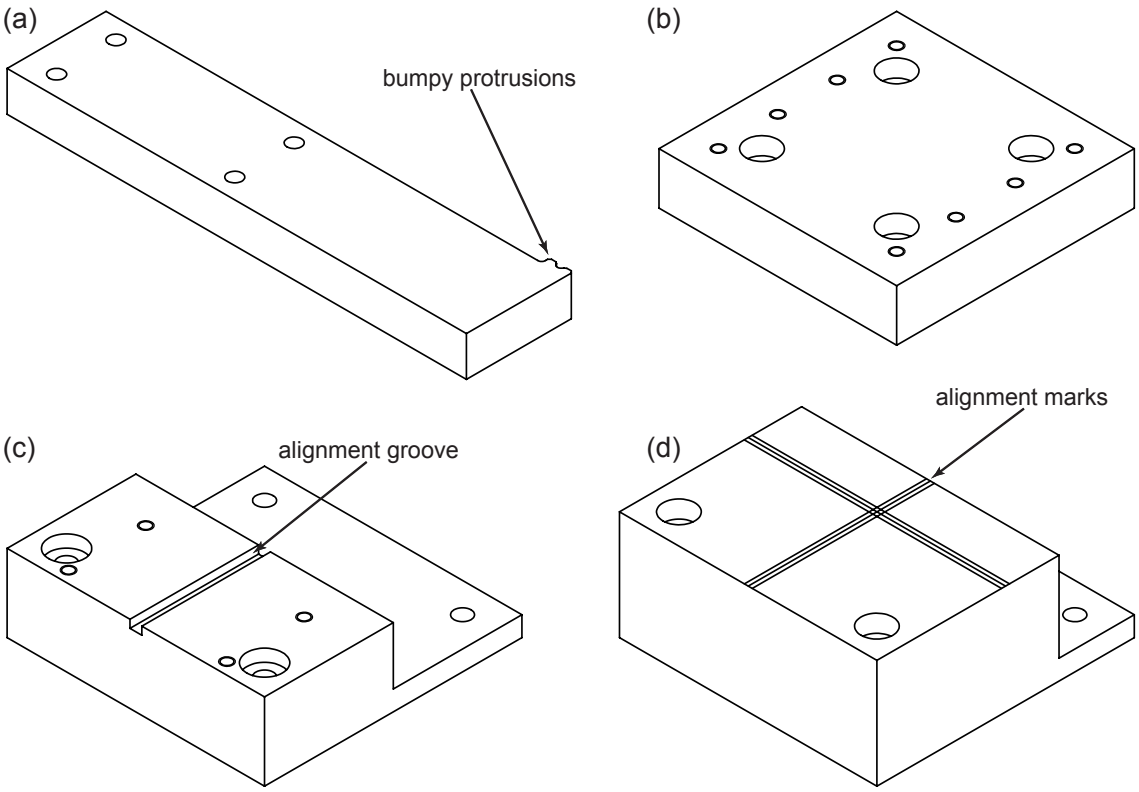

Figure A.2: Drawings of additional hardware used for cavity assembly. (a) aluminum lever, adapters for (b) the lever and (c) the steel v-groove, (d) aluminum block.

A.2 Setup components list

Diverse components are listed that are used in the various arrangements of the measurement setup.

Table A.1: Electronic measurement and controller devices.

component / part number	manufacturer / distributor	description
33220A	Agilent	arbitrary waveform generator
3390	Keithley	arbitrary waveform generator
SMA100A	Rohde&Schwarz	signal generator
SML3	Rohde&Schwarz	signal generator
FSU26	Rohde&Schwarz	spectrum analyzer
FSP3	Rohde&Schwarz	spectrum analyzer
ZVB4	Rohde&Schwarz	network analyzer
ZVL3	Rohde&Schwarz	network analyzer
TDS2024B	Tektronix	oscilloscope
TDS2014B	Tektronix	oscilloscope
NI PCI-6014	National Instruments	data acquisition card
ANC300	attocube	piezo positioning controller

Table A.2: Homebuilt electronics and optoelectronic components.

component / part number	manufacturer / distributor	description
Lockbox 5	A. Scheich / LS Hänsch	feed back electronics
RF-Lock-In amplifier	A. Scheich / LS Hänsch	for laser stabilization
RF-photo detector	A. Scheich / LS Hänsch	for laser stabilization
high voltage low noise amplifier	A. Scheich / LS Hänsch	cavity piezo driver
external cavity diode laser	homebuilt / LS Hänsch copy	wavelength 780 nm
DC110 with DCC110, DCT110	Toptica	laser controller with current and temperature control
fiber polarization controller	homebuilt	three paddles with 1, 2 and 1 fiber loops with 45 mm diameter
PDA 55	Thorlabs	variable gain photo detector
photo detector	S. Manus / LS Kotthaus	Hamamatsu G9801-22 Z_{tr} = 100 kΩ, BW = 10 MHz
photo detector	homebuilt	BPW34 and BPW33 + transimpedance amplifier

Table A.3: Fiberoptic and RF-electronic components.

component / part number	**manufacturer / distributor**	**description**
MX-050-0813-50-17-1	Laser Components	multimode wavelength devision multiplexer, 850 nm/1300 nm
CA-050-50-12-08-17-1	Laser Components	multimode coupler, 1 by 2 ports, ratio 50/50
NIR-MPX800-LN10-P-P-FA-FA	Photline	electro-optic modulator, 800 nm, BW = 10 GHz
ZFSC-2-10G+ (SMA)	Mini Circuits	RF power splitter/combiner
ZN2PD2-50-S+	Mini Circuits	RF power splitter/combiner
ZFBT-4R2GW+ (SMA)	Mini Circuits	RF coaxial bias-tee

Appendix B

Silicon nitride sample fabrication

The fabrication processes for the samples used in chapter 5 are described. Fabrication of SiN string resonators requires electron beam lithography and reactive ion etching.
For lithography the eLine (*Raith*) and especially the fixed beam moving stage mode (FBMS) for patterning is used. Relevant parameters in this mode depend on the nominal geometry of the structures and are listed in table B.1.
Dry etching is performed with the ICP-RIE Plasmalab System 100, *Oxford Instruments*. In the following two processes for fabrication of wide strings ranging from 1 to 30 µm in width and narrow structures with widths down to 100 nm are described. Main differences are the applied lithographic resin and etch mask. But some common annotations are mentioned first:

- **Preparations**

  Processing starts with commercially available silicon nitride window chips (*norcada*, NX5050AS) as used for sample holders in transmission electron microscopy. Square windows have an edge length of $500\,\mu\mathrm{m}$ and the thickness of the membrane is $50\,\mathrm{nm}$. The outer dimensions of these chips are $5\,\mathrm{mm}$ squared and $200\,\mu\mathrm{m}$ in thickness. No pre-cleaning is required since the chips are delivered in excellent quality ready for use.

- **Electron beam lithography**

  Membranes are very fragile and must not be subjected directly to the vacuum clamping mechanism of a spin-coater. Instead the chip is glued with double-sided tape to a fragment of a microscopy glass slide which is sucked to the rotary table. Removal of resist residues on the rear side of the chips is mandatory prior to SEM lithography. This way sample tilt is prevented and the focus of the electron beam, once set to the sample surface, needs not to be readjusted on the membrane area during exposure. Fixed beam moving stage (FBMS) patterning mode is used. Write field alignment and angle correction are not used for exposure because it was found

that these corrections cause a slightly wavy trajectory instead of a straight line. This is an undesired shape especially for strings that are less than 1 µm in width. For those narrow structure, it is recommended to orient them along a main axis in the design file and to pay attention to accurate clamping of the membrane with the window edge parallel to the SEM stage axes. This way write field alignment and angle correction can be disabled and the strings are parallel to the window edge.

- **Dry and wet etch**

  Membranes have uniform planar built in stress. This stress relaxes as the membrane is released from the window frame. Etching just one side of the three supports of the membrane does not work and yields in rupture of the residual membrane. In order to fabricate strings out of the membrane this release takes place on either side of the string during one dry etching process. Thus the support and the stress on both sides of the string are reduced simultaneously. Wet chemical processes can be very harmful to structures released from the membrane and should be avoided for strings less wide than a micron. Chips with wider strings are dipped into and pulled out of liquids only along the long extension of the strings. This way forces by surface tension act parallel to the strings and react in the clamping points. Stirring was performed very gently. It is strongly recommended to perform wet chemical steps with very clean glass beakers, and if yield of the process drops, beaker set should be replaced by new ones.

B.1 Wide strings

The fabrication method for strings that are wider than 1 µm involves PMMA e-beam resist, dry and wet etching procedures. This process is adopted to membranes from the method used in [Kre11, Sei12, Fau13, Rie13]. The steps with relevant parameters for this process are listed in table B.2 and table B.5.

B.2 Narrow strings

The process for strings with widths down to 100 nm is described. Wet chemical processes can be very harmful to structures released from the membrane and should be avoided for strings less wide than a micron. Thus a process is developed using a negative e-beam resist and dry etching procedures only. The steps with relevant parameters for this process are listed in table B.4 and table B.5.

Table B.1: FBMS parameters. Here *n.a.* means *not applicable*.

nominal width	µm	30	2	< 1
aperture	µm	120	20	20
acceleration voltage	kV	20	20	20
beam current	pA	4933	173	94
area dose	µC/cm^2	300	300	n.a.
line dose	nC/cm	n.a.	n.a.	3…8
stage speed	µm/s	48	187	118…315
FBMS calculation width	µm	30	2	n.a.
FBMS step size	nm	131	9.6	n.a.
FBMS cycle time	µs	6550	668	n.a.

Table B.2: Lithography procedure for SiN strings of widths form 1 to 30 µm.

step	description
deposit resist	spin-coat PMMA 950k A6 at 800 rpm for 1 s, at 5000 rpm for 30 s bake at 120 °C for at least 60 min
conductive layer	evaporate 3 nm of chromium onto the resist
SEM lithography	FBMS mode, SEM parameters are described in table B.1 for structures of 30 µm and 2 µm nominal width
chromium etch	in chromium etchant (111547, *Selectipur*) for 30 s, rinse in water
develop	in isopropanol:MIBK (3:1) for 50 s rinse in isopropanol, blow-dry with nitrogen
O_2 plasma clean	at 1 torr with 200 W RF power for 30 s
deposit etch mask	evaporate 30 nm of cobalt
lift-off	in warm acetone rinse in isopropanol, blow-dry with nitrogen

Table B.3: Etching procedure for SiN strings of widths form 1 to 30 µm.

step	description
ICP-RIE dry etch	4 sccm Ar and 2 sccm SF_6 at 2 mtorr with ICP power of 70 W and RF power of 35 W, duration 4 min
mask removal	in "piranha" ($H_2SO_4 : H_2O_2$ at ratio 1:1) for 90 s
drying	rinse in water and hot isopropanol and immediately blow-dry with nitrogen
cleaving	cleave the chip along one edge of the membrane window

Table B.4: Lithography procedure for SiN strings of widths below 1 µm.

step	description
conductive layer	evaporate 10 nm of chromium onto the rear side of the membrane
adhesion layer	spin-coat HDMS at 1000 rpm for 1 s, at 4000 rpm for 30 s bake at 85 °C for 60 s
deposit resist	spin-coat AR-N7500.08 *ALLRESIST* at 1000 rpm for 1 s, at 4000 rpm for 30 s bake at 85 °C for 60 s
SEM lithography	FBMS mode, SEM parameters are described in table B.1 for structures of nominal width below 1 µm
develop	in AR300-47 (*ALLRESIST*):water (3:1) for 120 s rinse in water
chromium etch	in diluted chromium etchant (111547, *Selectipur*):water (1:1) for 60 s rinse in water and isopropanol, blow-dry with nitrogen

Table B.5: Etching procedure for SiN strings of widths below 1 µm.

step	description
ICP-RIE dry etch	4 sccm Ar and 2 sccm SF_6 at 2 mtorr with ICP power of 70 W and RF power of 35 W, duration 4 min
mask removal	O_2 plasma etch at 2 torr with 200. . . 260 W RF power for 175 min
cleaving	cleave the chip along one edge of the membrane window

Bibliography

[Alb13] R. Albrecht, A. Bommer, C. Deutsch, J. Reichel, and C. Becher. Coupling of a Single Nitrogen-Vacancy Center in Diamond to a Fiber-Based Microcavity. *Physical Review Letters* **110**, 243602 (2013).

[And14] R. W. Andrews, R. W. Peterson, T. P. Purdy, K. Cicak, R. W. Simmonds, C. A. Regal, and K. W. Lehnert. Bidirectional and efficient conversion between microwave and optical light. *Nature Physics* **10**, 321 (2014).

[Ane10a] G. Anetsberger. *Novel Cavity Optomechanical Systems at the Micro- and Nanoscale and Quantum Measurements of Nanomechanical Oscillators*. Ph.D. thesis, Ludwig-Maximilians-Universität München (2010).

[Ane10b] G. Anetsberger, E. Gavartin, O. Arcizet, Q. P. Unterreithmeier, E. M. Weig, M. L. Gorodetsky, J. P. Kotthaus, and T. J. Kippenberg. Measuring nanomechanical motion with an imprecision below the standard quantum limit. *Physical Review A* **82**, 061804 (2010).

[Arc06] O. Arcizet, P.-F. Cohadon, T. Briant, M. Pinard, A. Heidmann, J.-M. Mackowski, C. Michel, L. Pinard, O. Français, and L. Rousseau. High-Sensitivity Optical Monitoring of a Micromechanical Resonator with a Quantum-Limited Optomechanical Sensor. *Physical Review Letters* **97**, 133601 (2006).

[Asp10] M. Aspelmeyer, S. Gröblacher, K. Hammerer, and N. Kiesel. Quantum optomechanics—throwing a glance. *Journal of the Optical Society of America B* **27**, A189 (2010).

[Asp14] M. Aspelmeyer, T. J. Kippenberg, and F. Marquardt. Cavity optomechanics. *Reviews of Modern Physics* **86**, 1391 (2014).

[Bab03] B. Babić, J. Furer, S. Sahoo, S. Farhangfar, and C. Schönenberger. Intrinsic Thermal Vibrations of Suspended Doubly Clamped Single-Wall Carbon Nanotubes. *Nano Letters* **3**, 1577 (2003).

[Bak12] C. Baker, S. Stapfner, D. Parrain, S. Ducci, G. Leo, E. M. Weig, and I. Favero. Optical instability and self-pulsing in silicon nitride whispering gallery resonators. *Optics Express* **20**, 29076 (2012).

[Bar11] R. J. Barbour, P. A. Dalgarno, A. Curran, K. M. Nowak, H. J. Baker, D. R. Hall, N. G. Stoltz, P. M. Petroff, and R. J. Warburton. A tunable microcavity. *Journal of Applied Physics* **110**, 053107 (2011).

[Bia11] C. Biancofiore, M. Karuza, M. Galassi, R. Natali, P. Tombesi, G. Di Giuseppe, and D. Vitali. Quantum dynamics of an optical cavity coupled to a thin semi-transparent membrane: Effect of membrane absorption. *Physical Review A* **84**, 033814 (2011).

[Bla01] E. D. Black. An introduction to Pound-Drever-Hall laser frequency stabilization. *American Journal of Physics* **69**, 79 (2001).

[Bra67] V. B. Braginsky and A. B. Manukin. Ponderomotive Effects of Electromagnetic Radiation. *Soviet Journal of Experimental and Theoretical Physics* **25**, 653 (1967).

[Cha10] D. E. Chang, C. A. Regal, S. B. Papp, D. J. Wilson, J. Ye, O. Painter, H. J. Kimble, and P. Zoller. Cavity opto-mechanics using an optically levitated nanosphere. *Proceedings of the National Academy of Sciences* **107**, 1005 (2010). And supplementary information.

[Cha11] J. Chan, T. P. Mayer Alegre, A. H. Safavi-Naeini, J. T. Hill, A. Krause, S. Gröblacher, M. Aspelmeyer, and O. Painter. Laser cooling of a nanomechanical oscillator into its quantum ground state. *Nature* **478**, 89 (2011).

[Cha12] J. Chaste, A. Eichler, J. Moser, G. Ceballos, R. Rurali, and A. Bachtold. A nanomechanical mass sensor with yoctogram resolution. *Nature Nanotechnology* **7**, 301 (2012).

[Cle03] A. N. Cleland. *Foundations of Nanomechanics*. Springer (2003).

[Cle10] A. A. Clerk, M. H. Devoret, S. M. Girvin, F. Marquardt, and R. J. Schoelkopf. Introduction to quantum noise, measurement, and amplification. *Reviews of Modern Physics* **82**, 1155 (2010).

[Coh99] P. F. Cohadon, A. Heidmann, and M. Pinard. Cooling of a Mirror by Radiation Pressure. *Physical Review Letters* **83**, 3174 (1999).

[Cor07] T. Corbitt, C. Wipf, T. Bodiya, D. Ottaway, D. Sigg, N. Smith, S. Whitcomb, and N. Mavalvala. Optical Dilution and Feedback Cooling of a Gram-Scale Oscillator to 6.9 mK. *Physical Review Letters* **99**, 160801 (2007).

[Dem07] W. Demtröder. *Laserspektroskopie: Grundlagen und Techniken*. Springer (2007).

[Den10] H. Deniz, A. Derbakova, and L.-C. Qin. A systematic procedure for determining the chiral indices of multi-walled carbon nanotubes using electron diffraction - each and every shell. *Ultramicroscopy* **111**, 66 (2010).

[Din10] L. Ding, C. Baker, P. Senellart, A. Lemaitre, S. Ducci, G. Leo, and I. Favero. High Frequency GaAs Nano-Optomechanical Disk Resonator. *Physical Review Letters* **105**, 263903 (2010).

[Din11] L. Ding, C. Baker, P. Senellart, A. Lemaitre, S. Ducci, G. Leo, and I. Favero. Wavelength-sized GaAs optomechanical resonators with gigahertz frequency. *Applied Physics Letters* **98**, 113108 (2011).

[Dor83] A. Dorsel, J. D. McCullen, P. Meystre, E. Vignes, and H. Walther. Optical Bistability and Mirror Confinement Induced by Radiation Pressure. *Physical Review Letters* **51**, 1550 (1983).

[Eic11] A. Eichler, J. Moser, J. Chaste, M. Zdrojek, I. Wilson-Rae, and A. Bachtold. Nonlinear damping in mechanical resonators made from carbon nanotubes and graphene. *Nature Nanotechnology* **6**, 339 (2011).

[Eki05] K. L. Ekinci and M. L. Roukes. Nanoelectromechanical systems. *Review of Scientific Instruments* **76**, 061101 (2005).

[Els09] F. Elste, S. M. Girvin, and A. A. Clerk. Quantum Noise Interference and Backaction Cooling in Cavity Nanomechanics. *Physical Review Letters* **102**, 207209 (2009).

[Fau12] T. Faust, P. Krenn, S. Manus, J. P. Kotthaus, and E. M. Weig. Microwave cavity-enhanced transduction for plug and play nanomechanics at room temperature. *Nature Communications* **3**, 728 (2012).

[Fau13] T. Faust. *Damping, on-chip transduction, and coherent control of nanomechanical resonators*. Ph.D. thesis, Ludwig-Maximilians-Universität München (2013).

[Fau14] T. Faust, J. Rieger, M. J. Seitner, J. P. Kotthaus, and E. M. Weig. Signatures of two-level defects in the temperature-dependent damping of nanomechanical silicon nitride resonators. *Physical Review B* **89**, 100102 (2014).

[Fav08] I. Favero and K. Karrai. Cavity cooling of a nanomechanical resonator by light scattering. *New Journal of Physics* **10**, 095006 (2008).

[Fav09] I. Favero, S. Stapfner, D. Hunger, P. Paulitschke, J. Reichel, H. Lorenz, E. M. Weig, and K. Karrai. Fluctuating nanomechanical system in a high finesse optical microcavity. *Optics Express* **17**, 12813 (2009).

[Fia10] A. Fian, M. Lexholm, R. Timm, B. Mandl, U. Håkanson, D. Hessman, E. Lundgren, L. Samuelson, and A. Mikkelsen. New Flexible Toolbox for Nanomechanical Measurements with Extreme Precision and at Very High Frequencies. *Nano Letters* **10**, 3893 (2010).

[Fio11] V. Fiore, Y. Yang, M. C. Kuzyk, R. Barbour, L. Tian, and H. Wang. Storing Optical Information as a Mechanical Excitation in a Silica Optomechanical Resonator. *Physical Review Letters* **107**, 133601 (2011).

[Fit13] R. Fitzpatrick. *Oscillations and Waves: An Introduction*. CRC Press, Taylor & Francis Group (2013).

[FJ12] N. E. Flowers-Jacobs, S. W. Hoch, J. C. Sankey, A. Kashkanova, A. M. Jayich, C. Deutsch, J. Reichel, and J. G. E. Harris. Fiber-cavity-based optomechanical device. *Applied Physics Letters* **101**, 221109 (2012).

[Fuk09] S. Fukami, T. Arie, and S. Akita. Effect of Gaseous Dissipation of Oscillating Cantilevered Carbon Nanotubes. *Japanese Journal of Applied Physics* **48**, 06FG04 (2009).

[Gie12] J. Gieseler, B. Deutsch, R. Quidant, and L. Novotny. Subkelvin Parametric Feedback Cooling of a Laser-Trapped Nanoparticle. *Physical Review Letters* **109**, 103603 (2012).

[Gig06] S. Gigan, H. R. Böhm, M. Paternostro, F. Blaser, G. Langer, J. B. Hertzberg, K. C. Schwab, D. Bäuerle, M. Aspelmeyer, and A. Zeilinger. Self-cooling of a micromirror by radiation pressure. *Nature* **444**, 67 (2006).

[Gor10] M. L. Gorodetsky, A. Schliesser, G. Anetsberger, S. Deleglise, and T. J. Kippenberg. Determination of the vacuum optomechanical coupling rate using frequency noise calibration. *Optics Express* **18**, 23236 (2010).

[Han12] M. S. Hanay, S. Kelber, A. K. Naik, D. Chi, S. Hentz, E. C. Bullard, E. Colinet, L. Duraffourg, and M. L. Roukes. Single-protein nanomechanical mass spectrometry in real time. *Nature Nanotechnology* **7**, 602 (2012).

[Har08] M. J. Hartmann and M. B. Plenio. Steady State Entanglement in the Mechanical Vibrations of Two Dielectric Membranes. *Physical Review Letters* **101**, 200503 (2008).

[Hee95] W. A. d. Heer, W. S. Bacsa, A. Chatelain, T. Gerfin, R. Humphrey-Baker, L. Forro, and D. Ugarte. Aligned Carbon Nanotube Films: Production and Optical and Electronic Properties. *Science* **268**, 845 (1995).

[Hel94] S. W. Hell and J. Wichmann. Breaking the diffraction resolution limit by stimulated emission: stimulated-emission-depletion fluorescence microscopy. *Optics Letters* **19**, 780 (1994).

[Hsu09] I.-K. Hsu, M. T. Pettes, A. Bushmaker, M. Aykol, L. Shi, and S. B. Cronin. Optical Absorption and Thermal Transport of Individual Suspended Carbon Nanotube Bundles. *Nano Letters* **9**, 590 (2009).

[Hun10] D. Hunger, T. Steinmetz, Y. Colombe, C. Deutsch, T. W. Hänsch, and J. Reichel. A fiber Fabry-Perot cavity with high finesse. *New Journal of Physics* **12**, 065038 (2010).

[Hun12] D. Hunger, C. Deutsch, R. J. Barbour, R. J. Warburton, and J. Reichel. Laser micro-fabrication of concave, low-roughness features in silica. *AIP Advances* **2**, 012119 (2012).

[Imb14] M. Imboden and P. Mohanty. Dissipation in nanoelectromechanical systems. *Physics Reports* **534**, 89 (2014).

[Jöc11] A. Jöckel, M. T. Rakher, M. Korppi, S. Camerer, D. Hunger, M. Mader, and P. Treutlein. Spectroscopy of mechanical dissipation in micro-mechanical membranes. *Applied Physics Letters* **99**, 143109 (2011).

[Jen08] K. Jensen, K. Kim, and A. Zettl. An atomic-resolution nanomechanical mass sensor. *Nature Nanotechnology* **3**, 533 (2008).

[Kar08] D. M. Karabacak. *Resonant operation of nanoelectromechanical systems in fluidic environments*. Ph.D. thesis, Boston University (2008).

[Kim13] P. H. Kim, C. Doolin, B. D. Hauer, A. J. R. MacDonald, M. R. Freeman, P. E. Barclay, and J. P. Davis. Nanoscale torsional optomechanics. *Applied Physics Letters* **102**, 053102 (2013).

[Kle88] M. V. Klein and T. E. Furtak. *Optik*. Springer-Verlag (1988).

[Kle06] D. Kleckner and D. Bouwmeester. Sub-kelvin optical cooling of a micromechanical resonator. *Nature* **444**, 75 (2006).

[Kol12] R. Kolesov, K. Xia, R. Reuter, R. Stöhr, A. Zappe, J. Meijer, P. R. Hemmer, and J. Wrachtrup. Optical detection of a single rare-earth ion in a crystal. *Nature Communications* **3**, 1029 (2012).

[Kra12] A. G. Krause, M. Winger, T. D. Blasius, Q. Lin, and O. Painter. A high-resolution microchip optomechanical accelerometer. *Nature Photonics* **6**, 768 (2012).

[Kre11] P. Krenn. Heterodyne dielektrische Detektion von nanomechanischen Resonatoren. *Master's thesis, LMU München* (2011).

[Löf11] M. Löffler, U. Weissker, T. Mühl, T. Gemming, and B. Büchner. Robust determination of Young's modulus of individual carbon nanotubes by quasi-static interaction with Lorentz forces. *Ultramicroscopy* **111**, 155 (2011).

[Li09] M. Li, W. H. P. Pernice, and H. X. Tang. Reactive Cavity Optical Force on Microdisk-Coupled Nanomechanical Beam Waveguides. *Physical Review Letters* **103**, 223901 (2009).

[Lif00] R. Lifshitz and M. L. Roukes. Thermoelastic damping in micro- and nanomechanical systems. *Physical Review B* **61**, 5600 (2000).

[Mar07] M. J. Martin and B. H. Houston. Gas damping of carbon nanotube oscillators. *Applied Physics Letters* **91**, 103116 (2007).

[Met04] C. H. Metzger and K. Karrai. Cavity cooling of a microlever. *Nature* **432**, 1002 (2004).

[Met08] C. Metzger, I. Favero, A. Ortlieb, and K. Karrai. Optical self cooling of a deformable Fabry-Perot cavity in the classical limit. *Physical Review B* **78**, 035309 (2008).

[Nay04] A. H. Nayfeh and D. T. Mook. *Nonlinear oscillations*. Wiley (2004).

[Neu11] E. Neu, D. Steinmetz, J. Riedrich-Möller, S. Gsell, M. Fischer, M. Schreck, and C. Becher. Single photon emission from silicon-vacancy colour centres in chemical vapour deposition nano-diamonds on iridium. *New Journal of Physics* **13**, 025012 (2011).

[O'C10] A. D. O'Connell, M. Hofheinz, M. Ansmann, R. C. Bialczak, M. Lenander, E. Lucero, M. Neeley, D. Sank, H. Wang, M. Weides, J. Wenner, J. M. Martinis, and A. N. Cleland. Quantum ground state and single-phonon control of a mechanical resonator. *Nature* **464**, 697 (2010).

[Ost10] L. Ost. Kontrolliertes Wachstum von Kohlenstoffnanoröhrchen für optomechanische Experimente. *Master's thesis, LMU München* (2010).

[Pin99] M. Pinard, Y. Hadjar, and A. Heidmann. Effective mass in quantum effects of radiation pressure. *The European Physical Journal D - Atomic, Molecular, Optical and Plasma Physics* **7**, 107 (1999).

[Plu00] J. Plummer, M. Deal, and P. Griffin. *Silicon VLSI Technology: Fundamentals, Practice and Modeling*. Prentice Hall electronics and VLSI series. Prentice Hall (2000).

[Poo08] M. Poot and H. S. J. van der Zant. Nanomechanical properties of few-layer graphene membranes. *Applied Physics Letters* **92**, 063111 (2008).

[Reg08] C. A. Regal, J. D. Teufel, and K. W. Lehnert. Measuring nanomechanical motion with a microwave cavity interferometer. *Nature Physics* **4**, 555 (2008).

[Rep14] J. Repp, G. J. Schinner, E. Schubert, A. K. Rai, D. Reuter, A. D. Wieck, U. Wurstbauer, J. P. Kotthaus, and A. W. Holleitner. Confocal shift interferometry of coherent emission from trapped dipolar excitons. *Applied Physics Letters* **105**, 241101 (2014).

[Ric95] L. Ricci, M. Weidemiiller, T. Esslinger, A. Hemmerich, C. Zimmermann, V. Vuletic, W. Kijnig, and T. W. Hänsch. A compact grating-stabilized diode laser system for atomic physics. *Optics Communications* **117**, 541 (1995).

[Rie12] J. Rieger, T. Faust, M. J. Seitner, J. P. Kotthaus, and E. M. Weig. Frequency and Q factor control of nanomechanical resonators. *Applied Physics Letters* **101**, 103110 (2012).

[Rie13] J. Rieger. *AFM manipulation of damping in nanomechanical resonators*. Ph.D. thesis, Ludwig-Maximilians-Universität München (2013).

[Rie14] J. Rieger, A. Isacsson, M. J. Seitner, J. P. Kotthaus, and E. M. Weig. Energy losses of nanomechanical resonators induced by atomic force microscopy-controlled mechanical impedance mismatching. *Nature Communications* **5**, 3345 (2014).

[Roc10] T. Rocheleau, T. Ndukum, C. Macklin, J. B. Hertzberg, A. A. Clerk, and K. C. Schwab. Preparation and detection of a mechanical resonator near the ground state of motion. *Nature* **463**, 72 (2010).

[Ruo03] R. S. Ruoff, D. Qian, and W. K. Liu. Mechanical properties of carbon nanotubes: theoretical predictions and experimental measurements. *Comptes Rendus Physique* **4**, 993 (2003).

[Sal91] B. E. A. Saleh and M. C. Teich. *Fundamentals of Photonics*. John Wiley & Sons (1991).

[Sal99] J.-P. Salvetat, G. A. D. Briggs, J.-M. Bonard, R. R. Bacsa, A. J. Kulik, T. Stöckli, N. A. Burnham, and L. Forró. Elastic and Shear Moduli of Single-Walled Carbon Nanotube Ropes. *Physical Review Letters* **82**, 944 (1999).

[San10] J. C. Sankey, C. Yang, B. M. Zwickl, A. M. Jayich, and J. G. E. Harris. Strong and tunable nonlinear optomechanical coupling in a low-loss system. *Nature Physics* **6**, 707 (2010).

[Sch06] A. Schliesser, P. Del'Haye, N. Nooshi, K. J. Vahala, and T. J. Kippenberg. Radiation Pressure Cooling of a Micromechanical Oscillator Using Dynamical Backaction. *Physical Review Letters* **97**, 243905 (2006).

[Sch12] B. H. Schneider, S. Etaki, H. S. J. van der Zant, and G. A. Steele. Coupling carbon nanotube mechanics to a superconducting circuit. *ArXiv e-prints* **arXiv:1209.1514** (2012).

[Sei12] M. J. Seitner. Mechanische und dielektrische Manipulation nanomechanischer Resonatoren. *Master's thesis, LMU München* (2012).

[Sie86] A. E. Siegman. *Lasers*. University Science Books (1986).

[SN11] A. H. Safavi-Naeini, T. P. M. Alegre, J. Chan, M. Eichenfield, M. Winger, Q. Lin, J. T. Hill, D. E. Chang, and O. Painter. Electromagnetically induced transparency and slow light with optomechanics. *Nature* **472**, 69 (2011).

[Son10] L. Song, L. Ci, H. Lu, P. B. Sorokin, C. Jin, J. Ni, A. G. Kvashnin, D. G. Kvashnin, J. Lou, B. I. Yakobson, and P. M. Ajayan. Large Scale Growth and Characterization of Atomic Hexagonal Boron Nitride Layers. *Nano Letters* **10**, 3209 (2010).

[Sri06] K. Srinivasan, M. Borselli, O. Painter, A. Stintz, and S. Krishna. Cavity Q, mode volume, and lasing threshold in small diameter AlGaAs microdisks with embedded quantum dots. *Optics Express* **14**, 1094 (2006).

[Sta10] S. Stapfner, I. Favero, D. Hunger, P. Paulitschke, J. Reichel, K. Karrai, and E. Weig. Cavity nano-optomechanics: a nanomechanical system in a high finesse optical cavity. *Proc. SPIE* **7727**, 772706 (2010). *ArXiv e-prints* 1110.6292v1.

[Sta13] S. Stapfner, L. Ost, D. Hunger, J. Reichel, I. Favero, and E. M. Weig. Cavity-enhanced optical detection of carbon nanotube Brownian motion. *Applied Physics Letters* **102**, 151910 (2013).

[Ste06] T. Steinmetz, Y. Colombe, D. Hunger, T. W. Hänsch, A. Balocchi, R. J. Warburton, and J. Reichel. Stable fiber-based Fabry-Pérot cavity. *Applied Physics Letters* **89**, 111110 (2006).

[Ste09] G. A. Steele, A. K. Hüttel, B. Witkamp, M. Poot, H. B. Meerwaldt, L. P. Kouwenhoven, and H. S. J. van der Zant. Strong Coupling Between Single-Electron Tunneling and Nanomechanical Motion. *Science* **325**, 1103 (2009).

[Sum13] H. Sumikura, E. Kuramochi, H. Taniyama, and M. Notomi. Cavity-enhanced Raman scattering of single-walled carbon nanotubes. *Applied Physics Letters* **102**, 231110 (2013).

[Teu11a] J. D. Teufel, T. Donner, D. Li, J. W. Harlow, M. S. Allman, K. Cicak, A. J. Sirois, J. D. Whittaker, K. W. Lehnert, and R. W. Simmonds. Sideband cooling of micromechanical motion to the quantum ground state. *Nature* **475**, 359 (2011).

[Teu11b] J. D. Teufel, D. Li, M. S. Allman, K. Cicak, A. J. Sirois, J. D. Whittaker, and R. W. Simmonds. Circuit cavity electromechanics in the strong-coupling regime. *Nature* **471**, 204 (2011).

[Tho08] J. Thompson, B. Zwickl, A. Jayich, F. Marquardt, S. Girvin, and J. Harris. Strong dispersive coupling of a high-finesse cavity to a micromechanical membrane. *Nature* **452**, 72 (2008).

[Tie12] C.-L. Tien and T.-W. Lin. Thermal expansion coefficient and thermomechanical properties of SiNx thin films prepared by plasma-enhanced chemical vapor deposition. *Applied Optics* **51**, 7229 (2012).

[Tis11] J. Tisler, R. Reuter, A. Lämmle, F. Jelezko, G. Balasubramanian, P. R. Hemmer, F. Reinhard, and J. Wrachtrup. Highly Efficient FRET from a Single Nitrogen-Vacancy Center in Nanodiamonds to a Single Organic Molecule. *ACS Nano* **5**, 7893 (2011).

[Tre96] M. M. J. Treacy, T. W. Ebbesen, and J. M. Gibson. Exceptionally high Young's modulus observed for individual carbon nanotubes. *Nature* **381**, 678 (1996).

[Unt09] Q. P. Unterreithmeier, E. M. Weig, and J. P. Kotthaus. Universal transduction scheme for nanomechanical systems based on dielectric forces. *Nature* **458**, 1001 (2009).

[Unt10] Q. P. Unterreithmeier, T. Faust, and J. P. Kotthaus. Damping of Nanomechanical Resonators. *Physical Review Letters* **105**, 027205 (2010).

[Ver08a] S. S. Verbridge, H. G. Craighead, and J. M. Parpia. A megahertz nanomechanical resonator with room temperature quality factor over a million. *Applied Physics Letters* **92**, 013112 (2008).

[Ver08b] S. S. Verbridge, R. Ilic, H. G. Craighead, and J. M. Parpia. Size and frequency dependent gas damping of nanomechanical resonators. *Applied Physics Letters* **93**, 013101 (2008).

[Vit07] D. Vitali, S. Gigan, A. Ferreira, H. R. Böhm, P. Tombesi, A. Guerreiro, V. Vedral, A. Zeilinger, and M. Aspelmeyer. Optomechanical Entanglement between a Movable Mirror and a Cavity Field. *Physical Review Letters* **98**, 030405 (2007).

[Wal60] R. A. Waldron. Perturbation theory of resonant cavities. *Proceedings of the IEE - Part C: Monographs* **107C**, 272 (1960).

[Wea90] Weaver, W. and Timoshenko, S. P. and Young, D. H. *Vibration problems in engineering*. John Wiley & Sons, 5th edition (1990).

[Wei10] S. Weis, R. Rivière, S. Deléglise, E. Gavartin, O. Arcizet, A. Schliesser, and T. J. Kippenberg. Optomechanically Induced Transparency. *Science* **330**, 1520 (2010).

[Wil09] D. J. Wilson, C. A. Regal, S. B. Papp, and H. J. Kimble. Cavity Optomechanics with Stoichiometric SiN Films. *Physical Review Letters* **103**, 207204 (2009).

[WR12] I. Wilson-Rae, C. Galland, W. Zwerger, and A. Imamoglu. Exciton-assisted optomechanics with suspended carbon nanotubes. *New Journal of Physics* **14**, 115003 (2012).

[Xue11] A. Xuereb, R. Schnabel, and K. Hammerer. Dissipative Optomechanics in a Michelson-Sagnac Interferometer. *Physical Review Letters* **107**, 213604 (2011).

[Ye15] M. Ye, D. Winslow, D. Zhang, R. Pandey, and Y. K. Yap. Recent Advancement on the Optical Properties of Two-Dimensional Molybdenum Disulfide (MoS2) Thin Films. *Photonics* **2**, 288 (2015).

[Yu12] P.-L. Yu, T. P. Purdy, and C. A. Regal. Control of Material Damping in High-Q Membrane Microresonators. *Physical Review Letters* **108**, 083603 (2012).

List of Publications

- Ivan Favero, Sebastian Stapfner, David Hunger, Philipp Paulitschke, Jakob Reichel, Heribert Lorenz, Eva M. Weig, Khaled Karrai. Fluctuating nanomechanical system in a high finesse optical microcavity. *Optics Express* **17**, 12813 (2009)

- Sebastian Stapfner, Ivan Favero, David Hunger, Philipp Paulitschke, Jakob Reichel, Khaled Karrai, Eva M. Weig. Cavity nano-optomechanics: a nanomechanical system in a high finesse optical cavity. *SPIE Proceedings* **7727**, 772706 (2010)

- Christophe Baker, Sebastian Stapfner, David Parrain, Sara Ducci, Giuseppe Leo, Eva M. Weig, Ivan Favero. Optical instability and self-pulsing in silicon nitride whispering gallery resonators. *Optics Express* **20**, 29076 (2012)

- Sebastian Stapfner, Lukas Ost, David Hunger, Jakob Reichel, Ivan Favero, Eva M. Weig. Cavity-enhanced optical detection of carbon nanotube Brownian motion. *Applied Physics Letters* **102**, 151910 (2013)

Vielen Dank

Abschließend möchte ich noch einigen großartigen Leuten danken, die zum Gelingen dieser Arbeit beigetragen haben:

Eva Weig, ich hab es sehr genossen, in deiner Nanomechanikgruppe arbeiten zu dürfen. Du hast mich sehr gut durch die Promotion begleitet und ich konnte vieles von dir lernen. Ich wünsche dir viel Spaß und alles Gute auf deiner, nun nicht mehr ganz so neuen Stelle in Konstanz!

Jörg Kotthaus, dir danke ich, dass ich hier am Lehrstuhl für meine Doktorarbeit werken durfte. Du ließt mich selbständig und ungezwungen meine Ideen umsetzten, und warst immer für Diskussionen offen. Ich hoffe, du kannst deinen wohlverdienten Ruhestand genießen!

Ivan Favero, vielen Dank, dass du dich aus Paris so sehr für meine Experimente interessiert und engagiert hast. Die Diskussionen und gegenseitigen Besuche haben mir immer wieder neue Impulse für die Arbeit gegeben. Danke auch an deinen Doktoranden Christophe Baker. Eigentlich sollte ich ihm Reinraumprozesse beibringen, doch bei jedem seiner Besuche konnte ich wichtige Erkenntisse für meine Projekte gewinnen.

Jakob Reichel möchte ich danken, dafür dass ich an seinem Setup in Zeiten der Not Fasern für eine neue Kavität schießen durfte. An dieser Stelle sei auch David Hunger und Hanno Kaupp gedankt, der Trip zum Jakob nach Paris mit euch war echt spitze. Sehr zu schätzen weiß ich auch die Unterstützung bei Fragen rund um den optischen Messaufbau. Ich danke Theodor Hänsch für elektronische Leihgaben für das Experiment.

Lukas Ost für sein außerordentliches Engagement und Geschick, um derart herrvorragenden CNT-Strukturen herzustellen. Die Arbeit mit dir hat mir sehr viel Spaß gemacht!

Dankeschön, Markus Döblinger, für das Anfertigen exzellenter HRTEM-Aufnahmen unserer CNT-Proben.

Danke an Ben Michaelis und Johannes Schmelzl für eure Beiträge zu den Messungen mit den Siliziumnitridstrukturen während eurer Bachelor- bzw. Diplomarbeit.

Vielen Dank an die lieben Nanomechaniker Onur Basarir, Thomas Faust, Phillip Paulitschke, Johannes Rieger, Darren Southworth und Quirin Unterreithmeier. Die Stimmung war sehr angenehm und ihr seid ein tolles Team gewesen!

Liebe Bürokollegen Florian Seilmeier, Jan Glückert, Matthias Fiebig, André Neumann, Sahra Witting, Sobhan Sepehri und Nooshin Yavari, dank euch hatten wir immer eine angenehme Atmosphäre im Büro.

Stephan Manus, vielen Dank für deine genialen Fotodetektoren, die kompetente Unterstützung in allen elektronischen und messtechnischen Fragestellungen und für alle Diskussionen, die darüber hinaus gingen.

Philipp Altpeter und Reinhold Rath, euch danke ich für eure vielseitige Unterstützung an den Geräten im exzellent geführten Reinraum.

Martina Jüttner und Bert Lorenz, danke für alle Unterstützung bei verwaltungstechnischen Belangen.

Vielen Dank an die Mitarbeiter der feinmechanischen Werkstatt, ohne die mechanischen Komponenten in der Präzision wären Teile dieser Arbeit überhaupt nicht zustande gekommen.

Danke an die komplette Besatzung des Lehrstuhls, es herrschte immer gute Stimmung. Ich hoffe, das bleibt auch in Zukunft so!